INFORMATION TO USERS

The most advanced technology has been used to photograph and reproduce this manuscript from the microfilm master. UMI films the text directly from the original or copy submitted. Thus, some thesis and dissertation copies are in typewriter face, while others may be from any type of computer printer.

The quality of this reproduction is dependent upon the quality of the copy submitted. Broken or indistinct print, colored or poor quality illustrations and photographs, print bleedthrough, substandard margins, and improper alignment can adversely affect reproduction.

In the unlikely event that the author did not send UMI a complete manuscript and there are missing pages, these will be noted. Also, if unauthorized copyright material had to be removed, a note will indicate the deletion.

Oversize materials (e.g., maps, drawings, charts) are reproduced by sectioning the original, beginning at the upper left-hand corner and continuing from left to right in equal sections with small overlaps. Each original is also photographed in one exposure and is included in reduced form at the back of the book. These are also available as one exposure on a standard 35mm slide or as a 17" x 23" black and white photographic print for an additional charge.

Photographs included in the original manuscript have been reproduced xerographically in this copy. Higher quality 6" x 9" black and white photographic prints are available for any photographs or illustrations appearing in this copy for an additional charge. Contact UMI directly to order.

U·M·I

University Microfilms International
A Bell & Howell Information Company
300 North Zeeb Road, Ann Arbor, MI 48106-1346 USA
313/761-4700 800/521-0600

Order Number 9000708

Study of electronic and vibrational properties of HgCdTe and CdTe

Ksendzov, Alexander, Ph.D.

City University of New York, 1989

U·M·I
300 N. Zeeb Rd.
Ann Arbor, MI 48106

A

STUDY OF ELECTRONIC AND VIBRATIONAL PROPERTIES OF HgCdTe AND CdTe

by

ALEXANDER KSENDZOV

A dissertation submitted to the Graduate Faculty in Physics in partial fulfillment of the requirements for the degree of Doctor of Philosophy, The City University of New York.

1989

This manuscript has been read and accepted for the Graduate Faculty in Physics in satisfaction of the dissertation requirement for the degree of Doctor of Philosophy.

4/17/89

Date

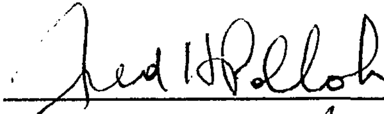

Chair of Examining Committee

4/17/89

Date

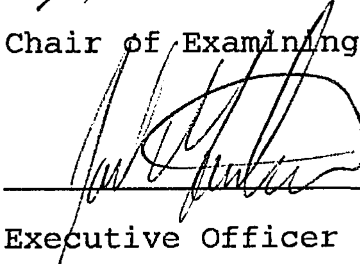

Executive Officer

Prof. Roshan L. Aggarwal

Prof. Steven Greenbaum

Prof. George Skorinko

Prof. Micha Tomkiewicz

Supervisory Committee

The City University of New York

Abstract

STUDY OF ELECTRONIC AND VIBRATIONAL PROPERTIES OF HgCdTe AND CdTe

by

Alexander Ksendzov

Adviser: Professor Fred H. Pollak

Electronic and vibrational properties of $Hg_{1-x}Cd_xTe$ and CdTe have been studied using modulation optical spectroscopy and Raman scattering. Electronic properties of $Hg_{1-x}Cd_xTe/SiO_2$- Photox™ interface also were investigated using electroreflectance (ER) and capacitance- voltage (C-V) measurements.

We have measured, for the first time, the nonlinear temperature dependence of the E_1 transition energy in CdTe using photoreflectance (PR) and in $Hg_{1-x}Cd_xTe$ (nominal composition x=0.3) using ER in a metal- insulator- semiconductor (MIS) configuration. The temperature variation of the broadening parameter was

also evaluated.

The temperature dependence of the E_0 transition in CdTe has been investigated by PR. Although the sample was not intentionally doped, the optical spectra in the E_0 region are dominated by transitions from the valence band to a donor level at temperatures over 200 K.

We have measured the frequency dependence of the PR signal at 77 K for a series of $Hg_{1-x}Cd_xTe$ samples (x= 0.14-0.3). This dependence yields the characteristic trap times (τ), which fall into 1-4 ms range for our samples.

The vibrational properties of $Hg_{1-x}Cd_xTe$ were studied by resonance Raman scattering (RRS). We found that in the forbidden polarization configuration RRS is caused by impurity induced scattering. It has been shown also, that the "LO & TO CdTe- like" peak in $Hg_{1-x}Cd_xTe$ belongs to a propagating mode rather than a localized vibration of a Cd atom in HgTe.

Electroreflectance in a MIS configuration was used to study the SiO_2 (Photox^{TM})/$Hg_{1-x}Cd_xTe$ interface. The ER spectra showed that, in addition to the $x\cong0.3$ semiconductor material, islands of the semimetallic ($x\cong0.1$) material are present at the interface. Also, with use of the C-V measurements, the presence of very slow (τ>8 h) trap states at the interface with energy distribution centered approximately 4.5 eV above the valence band of the SiO_2 was established.

The influence of the reflection from the back surface of a CdTe sample on its PR and thermoreflectance (TR) spectra in the E_0 region was compared. We found that while the TR lineshape was very sensitive to the condition of the back surface of the sample, the changes in the PR lineshape were negligible.

Preface

$Hg_{1-x}Cd_xTe$, HgTe and CdTe are interesting from both fundamental and applied points of view. These materials are not as well studied as the III-V zincblende systems and the data available on some of their properties are still controversial. The development of optical characterization techniques for $Hg_{1-x}Cd_xTe$ has a large practical value since it is extensively used in infrared detection applications. Recently a number of superlattice structures utilizing CdTe as one of the components have been grown. That revived interest in the optical properties of this material, some of which have not been studied thoroughly.

We have used modulation optical spectroscopy to probe the electronic bandstructure and Raman scattering spectroscopy to study the vibrational properties of these materials. We have also used capacitance- voltage measurements to probe the electronic properties of $Hg_{1-x}Cd_xTe/SiO_2$ interface.

The basic idea of modulation spectroscopy is a very general principle of experimental physics. Rather than measuring an optical spectrum directly, a

derivative with respect to a selected parameter is evaluated.

The derivative nature of modulation spectra suppresses unwanted background effects and emphasizes structures localized in the energy region of interband transitions at critical points in the Brillouin zone. Also, weak features that may not have been seen in the absolute spectra are enhanced. Because of this derivative- like nature, a large number of sharp spectral features can be observed even at room temperature. Since modulation spectroscopy is an ac method, additional information can be obtained by measuring other variables such as modulation frequency, modulation amplitude, phase of response of the sample to the modulation, ect.

Of the variety of modulation methods we put an emphasis on electromodulation techniques. Since the electromodulation spectra result from the response of the matter to the electric field, they contain additional information on the electric field distribution in the semiconductor. Also, in bulk material the electromodulation lineshapes are extremely sharp (they are proportional to the third derivative of the dielectric function over the photon energy) and, therefore yield very accurate values of electronic transition energies.

Study of the semiconductor- insulator interface is not only scientifically interesting, but also has a practical value. The instability of the material entails the need to passivate surfaces of $Hg_{1-x}Cd_xTe$- based devices. Electronic properties of an interface between the passivating material and the $Hg_{1-x}Cd_xTe$ substrate have not as yet been studied by optical methods and, therefore present an interesting object for investigation. The interface is also an integral part of the metal- insulator- semiconductor device. This makes the electroreflectance study of $Hg_{1-x}Cd_xTe$ in MIS configuration interesting for the practical purposes.

On the other hand, the MIS configuration provides the possibility to control the semiconductor surface potential which is not possible in other configurations, thus allowing the electroreflectance study of electric fields at the interface. Also, electromodulation experiments in the MIS configuration can be performed at low temperatures. Since electromodulation spectra are extremely sharp, temperature dependence of interband transitions can be investigated with high precision.

$Hg_{1-x}Cd_xTe$ is known to be extremely unstable. Therefore, contactless modulation methods are of special value since they do not cause any chemical changes at the surface. Photoreflectance is a contactless electromodulation technique and, as such, is a very

important tool for studying $Hg_{1-x}Cd_xTe$. Additional value of the photoreflectance technique stems from the fact that the modulation mechanism depends on photocharging of the trap states. Thus, information about characteristic trap state times may be extracted from the photoreflectance spectra.

Raman spectroscopy is one of the most useful methods of studying the vibrational spectra of solids. Raman scattering is a function of the electron- phonon (lattice vibrations) interaction. Since lattice vibrations are very sensitive to local environments, Raman spectra can give information about material structure or quality on the scale of a few lattice constants. Also, since Raman scattering is a second-order process, it contains symmetry information not available from first- order interactions. For example, in diamond and zincblende- type semiconductors frst-order processes are not sensitive to the polarization of the radiation (relative to the crystal axes) whereas in Raman scattering the scattering intensity for a given phonon mode is a function of both incident and scattered light polarizations. This dependence leads to symmetry information that can be utilized to characterize many parameters of materials.

The method of resonance Raman scattering (RRS) is based on the study of the energy dependence of Raman

scattering efficiency. Since the Raman scattering depends on the electron- phonon interaction, the RRS is determined by the parameters of the intermediate electronic states (such as energy and broadening). Thus RRS can be used to complement the techniques used for the electronic band structure studies. Even more important is the link that RRS can provide between the electronic and lattice- dynamical properties. By evaluating the parameters of the intermediate electronic states, one may differentiate between localized vibrations (bound to impurities or local parts of the electronic wavefunction) and propagating vibrational modes.

This thesis is divided into five chapters. In Chapter I the electronic and vibrational spectra of $Hg_{1-x}Cd_xTe$ are discussed. A short overview of the material applications is also given.

Chapter II presents theoretical background of the modulation spectroscopy and discusses the experimental modulation techniques.

Chapter III presents experimental results obtained by electromodulation techniques. The results are discussed and compared to the data available in the literature.

Chapter IV deals with Raman spectroscopy. First the theoretical background is discussed. Then the data

obtained from resonance Raman scattering and symmetry selection rules measurements on bulk samples of $Hg_{1-x}Cd_xTe$ are presented and interpreted.

In Chapter V we present the results of the measurements of photocharging of the $Hg_{1-x}Cd_xTe/SiO_2$ interface. The results are explained in terms of a model distribution of very long- lived interface states.

Appendix A is devoted to experimental comparison of the interference effects in photoreflectance and thermoreflectance spectra of CdTe in the fundamental bandgap region. We find that thermoreflectance spectra are much stronger affected by the interference and give qualitative explanation of this fact.

Acknowledgements

I am deeply grateful to my adviser, Professor Fred H. Pollak. I am lucky to have had an opportunity to draw on his knowledge and experience. He expertly guided me through the years of work which resulted in this thesis.

To the other members of the Examining Committee, Professor Roshan Aggrawal, Professor Steven Greenbaum, Professor George Skorinko and Professor Micha Tomkiewicz, my sincere thanks for their criticisms and helpful advice.

I thank Dr. Paul M. Amirtharaj for the numerous stimulating discussions and advice and for sharing samples. I am greatful to Dr. Hongen Shen who volunteered his help and generously permitted the use of his excellent computer programs.

I am indebted to Dr. J. A. Wilson, Dr. V. A. Cotton, Dr. O. Wu and Dr. E. A. Patten for providing samples used in this study.

My family provided encouragement and patient support during the years of my graduate study. This work would not be possible without them.

Table of Contents

Abstract....................................iii

Preface....................................vi

Acknowlegements....................................xii

I. $Hg_{1-x}Cd_xTe$....................................1

1.1 Electronic Band Structure 1

1.2 Vibrational Spectra 7

1.3 Applications 11

II. Modulation Spectroscopy....................13

2.1 Introduction....................13

2.2 Interaction of Light With Condensed Matter......14

2.3 Modulation Techniques....................19

2.4 Electromodulation Methods....................25

2.4.1 Electroreflectance....................25

2.4.2 Photoreflectance....................26

2.3.3 Experimental Details....................29

III. Results and Discussion - Modulation Spectroscopy 35

3.1 Review: Dependence of the Electronic Transition Energies of $Hg_{1-x}Cd_xTe$ on Composition and Temperature....................35

3.2 Electroreflectance of $Hg_{1-x}Cd_xTe$ in Metal-Insulator- Semiconductor Configuration.......43

3.2.1 Sample Preparation 43

3.2.2 Temperature Dependence of the E_1 Transition of $Hg_{1-x}Cd_xTe$....................................43
3.2.3 Dependence of Electroreflectance Signal on the Gate Bias....................................50
3.3 Pump Chopping Frequency Dependence of Photoreflectance in $Hg_{1-x}Cd_xTe$...............60
3.3.1 Experimental....................................63
3.3.2 Results....................................64
3.3.3 Analysis and Discussion.......................67
3.4 Temperature Dependence of Photoreflectance of Bulk CdTe 79
3.4.1 Sample Preparation............................80
3.4.2 Experimental Results..........................81
3.4.3 Analysis and Discussion......................83

IV. Raman Spectroscopy............................96
4.1 Macroscopic Description of Raman Scattering.....97
4.2 Selection Rules..............................101
4.3 Polarization Selection Rules..................102
4.4 Microscopic Theory............................104
4.5 Resonance Raman Scattering....................111
4.6 Experimental 117
4.7 Review: Vibrational Spectra of $Hg_{1-x}Cd_yTe$......121
4.8 Sample Details................................125
4.9 Results and Discussion........................126

V. Light induced charging of the $Hg_{1-x}Cd_xTe/SiO_2$ interface..144
5.1 Theory of Capacitance-Voltage Measurements.....145
5.2 Experimental Details...........................152
5.3 Experimental Results...........................155
5.4 Discussion.....................................161

Appendix
Influence of Interference on the Photoreflectance and Thermoreflectance Spectra of Bulk CdTe..........170

References...177

List of Tables

Table I. Compositional dependence of E_1 and $E_1+\Delta_1$ electronic transition energies in $Hg_{1-x}Cd_xTe$ 38

Table II. Experimental values of the E_1 transition energy and broadening parameter for $Hg_{1-x}Cd_xTe$ with x=0.3 MIS sample (RCS-254-4) at various temperatures..44

Table III. Energies, broadening parameters and phases obtained for the E_1^a and E_1^b features at various gate biases for MIS sample (ZH-245-3GB)........54

Table IV. Values of the energy gap and broadening parameter for the E_1 transition at 77 K for several $Hg_{1-x}Cd_xTe$ samples..............................76

Table V. Values of the time constant τ at 77 K for several $Hg_{1-x}Cd_xTe$ samples 78

Table VI. Energies and broadening parameters for the E_0 and E_1 transitions of CdTe at various temperatures.......................................89

Table VII Experimental and theoretical values of dE_1/dT for CdTe.......................................95

Table VIII. Polarization selection rules for Raman scattering from (110) surface........................107

Table IX. Phonon energies in CdTe and HgTe as

measured by Raman scattering 124

List of Figures

Fig.1 Conventional cell of zincblende structure.......2

Fig.2 The first Brillouin zone of fcc structure.......2

Fig.3 Electronic bandstructure of HgTe and CdTe.......3

Fig.4 Raman spectrum of $Hg_{0.8}Cd_{0.2}Te$..................10

Fig.5 Mechanism of the electric field modulation by light.......................................27

Fig.6 Electroreflectance setup........................30

Fig.7 Photoreflectance setup..........................33

Fig.8 Electroreflectance spectra of $Hg_{1-x}Cd_xTe$ (x = 0.3) sample (RCS-245-4) at 77 and 293 K...46

Fig.9 Temperature dependence of E_1 transition energy and broadening parameter for $Hg_{1-x}Cd_xTe$ (x = 0.3) MIS sample (RCS-245-4)...............47

Fig.10 Electroreflectance spectrum of $Hg_{1-x}Cd_xTe$ (x = 0.3) MIS sample (ZH-245-3GB)..............53

Fig.11 Electroreflectance spectrum of $Hg_{1-x}Cd_xTe$ (x=0.3) MIS sample (ZH-245-3GB) at various gate biases....................................56

Fig.12 Electroreflectance spectrum of $Hg_{1-x}Cd_xTe$ MIS (RCS-245-4) sample at room temperature.........61

Fig.13 Photoreflectance spectra of the x=0.22 LPE $Hg_{1-x}Cd_xTe$ sample at various chopping frequencies....................................66

Fig.14 Frequency dependence of the PR intensity for

the $x=0.22$ LPE $Hg_{1-x}Cd_xTe$ sample...............68

Fig.15 Photoreflectance spectrum of the $x=0.14$ $Hg_{1-x}Cd_xTe$ MBE (n-type) sample................69

Fig.16 Photoreflectance spectrum of the $x=0.3$ $Hg_{1-x}Cd_xTe$ bulk (n-type) sample..............70

Fig.17 Photoreflectance spectrum of the $x=0.3$ $Hg_{1-x}Cd_xTe$ bulk (p-type) sample taken with 4067 Å pump....................................71

Fig.18 Photoreflectance spectrum of the $x=0.3$ $Hg_{1-x}Cd_xTe$ bulk (p-type) sample taken with 4579 Å pump....................................72

Fig.19 Frequency dependence of the PR intensity for the $x=0.3$ bulk (p-type) $Hg_{1-x}Cd_xTe$ sample.....73

Fig.20 Photoreflectance spectra of the CdTe sample in the E_1 spectral region at various temperatures....................................85

Fig.21 Temperature dependence of the E_1 transition energy and broadening parameter for CdTe.......86

Fig.22 Photoreflectance spectra of the CdTe sample in the E_0 spectral region at various temperatures....................................87

Fig.23 Examples of the lineshape fit of the CdTe PR spectra in the E_0 spectral region.............88

Fig.24 Temperature dependence of the E_0 transition energy and broadening parameter for CdTe......90

Fig.25 First order Raman scattering..................106

Fig.26a Diagrams of the transitions producing

Fig.26a Diagrams of the transitions producing two-band contributions to the Raman tensor...109

Fig.26b Diagrams of the transitions producing three-band contributions to the Raman tensor..110

Fig.27 Diagram of a typical term contributing to the impurity- induced scattering..................116

Fig.28 The experimental setup for Raman scattering measurements.........................119

Fig.29 Compositional dependence of the vibrational frequencies in $Hg_{1-x}Cd_xTe$.....................123

Fig.30 Raman scattering spectra for $Hg_{1-x}Cd_xTe$ x=0.3 sample at 77 K.................................127

Fig.31 Raman scattering spectra for $Hg_{1-x}Cd_xTe$ x=0.3 sample at 10 K.................................128

Fig.32 The Raman scattering spectra for $Hg_{1-x}Cd_xTe$ x=0.2 sample at 77 K...........................129

Fig.33 The procedure of subtracting the elastic scattering background from Raman spectrum of $Hg_{1-x}Cd_xTe$ x=0.3 sample, taken at 77 K with 4965 Å excitation..............................131

Fig.34 The procedure of subtracting the elastic scattering background from Raman spectrum of $Hg_{1-x}Cd_xTe$ x=0.2 sample, taken at 10 K with 4965 Å excitation..............................132

Fig.35 Polarization selection rules study of the $Hg_{1-x}Cd_xTe$ x=0.3 sample.....................135

Fig.36 Comparison of PR and RRS results for

$Hg_{1-x}Cd_xTe$ x=0.3 sample at 77 K..............137

Fig.37 RRS results for $Hg_{1-x}Cd_xTe$ x=0.3 sample at 10 K..............................138

Fig.38 RRS results for $Hg_{1-x}Cd_xTe$ x=0.2 sample at 10 K...139

Fig.39 Band diagram of the ideal unbiased MIS device (n-type semiconductor).......................146

Fig.40 Band diagram of the ideal MIS device under bias (n-type semiconductor)..................147

Fig.41 The result of manual CV measurement of the MIS sample unexposed to light.................149

Fig.42 Setup for automated CV measurements...........153

Fig.43 Results of CV measurements after exposure to 2800 Å light at zero bias....................157

Fig.44 Photo-induced flatband shift ΔU_{fb} as a function of the total number of photons per cm^2...158

Fig.45 C-V curves taken after 1-μm light exposure with +10 V bias 160

Fig.46 Proposed model for $Hg_{1-x}Cd_xTe$ (n-type)/SiO_2-Photox™ interface...........................162

Fig.47 Experimental and theoretical values of $n_8(\hbar\omega)$ 167

Fig.48 Photoreflectance spectra of CdTe (111) sample with smooth (polished) and rough back surface 172

Fig.49 Thermoreflectance spectra of CdTe (111)

sample with smooth (polished) and rough back
surface..................................173

CHAPTER I

$Hg_{1-x}Cd_xTe$.

1.1 Electronic Band Structure.

Crystals of HgTe and CdTe have the zincblende structure at atmospheric pressure. This structure belongs to the space group (T_d^2)[1] and consists of two face centered cubic (fcc) lattices shifted relatively to one another by 1/4 of a body diagonal. A conventional cell of the zincblende structure is shown in Fig.1. The first Brilluoin zone of the fcc structure is shown in Fig.2. The set of commonly used notations for high symmetry points and directions is also given in this figure.

There have been a number of theoretical band structure calculations performed for CdTe and HgTe materials [2-4]. The results of the calculations by the workers of Ref.2 are shown in Fig.3. As seen in this figure, CdTe is a direct bandgap semiconductor with the fundamental gap at the Γ point of the Brillouin zone. The doubly degenerate level Γ_8 is the top of the valence band, Γ_6 is the lowest - lying conduction band and Γ_7 is the valence band split from Γ_8 by the spin- orbit interaction. In HgTe, however, the order of the

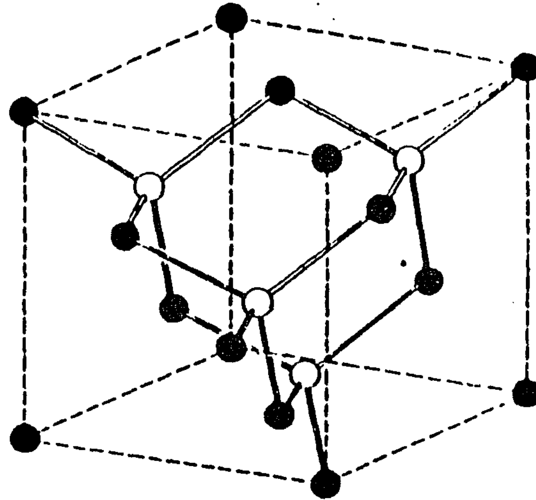

Fig.1

Conventional cell of the zinkblende structure.

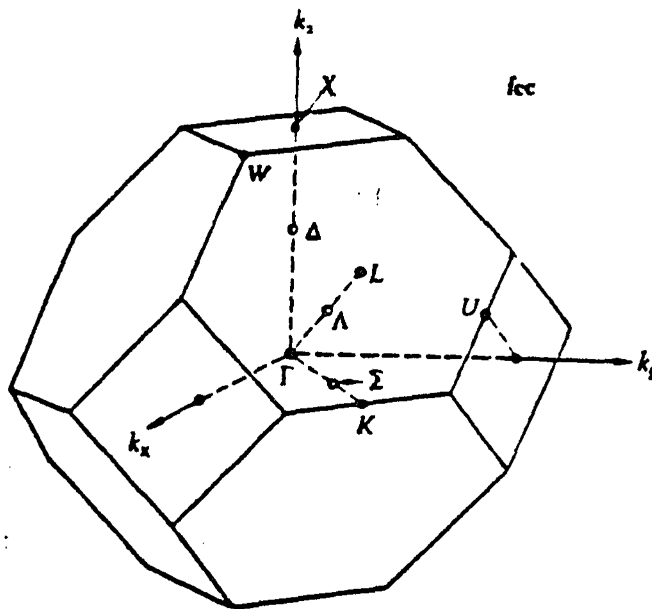

Fig.2

The first Brillouin zone of the fcc structure.

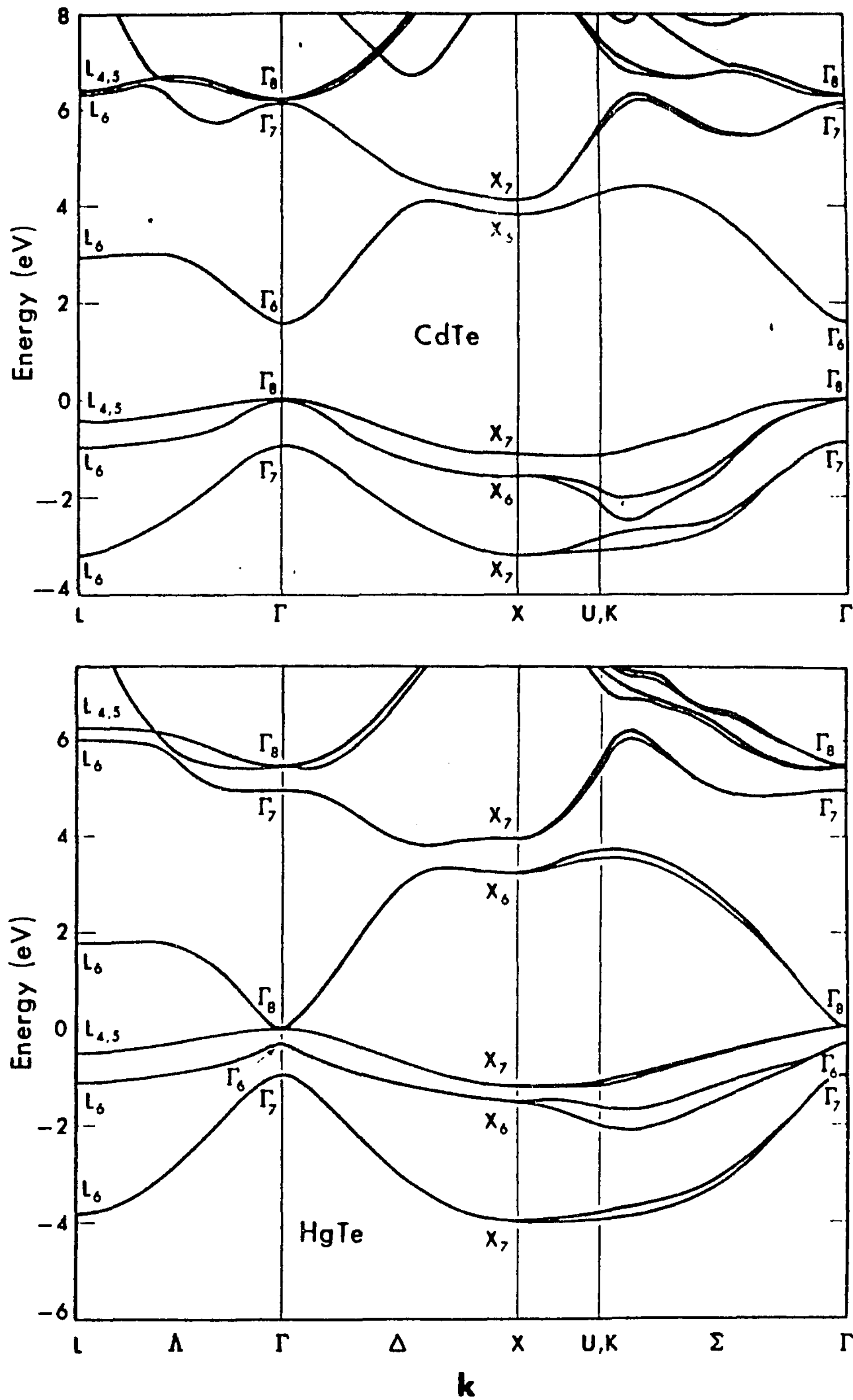

Fig.3

Electronic band structure of CdTe and HgTe (after Chadi et al[2]).

Γ_6 and Γ_8 bands is reversed (i.e. Γ_8 is higher in energy than Γ_6). Since Γ_8 is doubly degenerate, it is half filled by electrons and the material is a semimetal. The values of the fundamental energy gap and the critical points higher in energy have been measured by a variety of experimental methods[5].

We would like to point out that in spite of the long history of study of these materials, many of the optical properties of CdTe are not very well understood. The fundamental absorption spectra at room temperature have an Urbach tail[6] shape which has yet to be explained[7-9]. Also, some of the data suggest that even in samples that are not intentionally doped the optical spectra near the fundamental gap are dominated by the features caused by the shallow impurity (or defect) states[10]. This, in turn, is probably the cause of the very large disagreement between measurements of the temperature dependence of the fundamental energy gap, made by different groups[9].

$Hg_{1-x}Cd_xTe$ belongs to a very interesting class of pseudo binary alloys. CdTe and HgTe can be alloyed over the full range of composition. The process of alloying can be seen as an introduction of substitutional isovalent impurities into a binary compound (say, Hg introduced into CdTe). Such a process preserves the zincblende structure of the host material. It does,

however, introduce disorder into the crystal in the sense that the occupation of the cation sites becomes random. Local strains are introduced because of the different cation sizes. Local potentials at cation sites also change depending on the atom occupying the site. The important point is that the system remains the same topologically (in a marked contrast to glass forming alloys). So it may be expected that, unlike glasses, electronic properties of the pseudobinary alloys remain similar to the properties of the parent compounds and vary continuously through the whole range of composition.

Band structure calculations done for $Hg_{1-x}Cd_xTe$[3,4,11] predict nearly linear dependence of the fundamental energy gap on composition x. A great number of experimental measurements of the fundamental energy gap in $Hg_{1-x}Cd_xTe$ material have been made utilizing optical absorption[12], magnetoabsorption[13] and other techniques[14]. It has been found experimentally that at $x \cong 0.15$ at 77K the reversal of the Γ_6-Γ_8 order occurs causing the semiconductor- semimetal transition.

The temperature dependence of the fundamental energy gap in $Hg_{1-x}Cd_xTe$ is unusual: the value of the temperature coefficient $\delta E_g/\delta T$ varies from $-6 \cdot 10^{-4}$ eV/K at x=1 to $+5 \cdot 10^{-4}$ eV/K at x=0. While the $-6 \cdot 10^{-4}$ eV/K value for the CdTe is within the range typical for the

II-VI zinkblende semicomductors, the positive temperature coefficient at the HgTe end of the alloy is unusual. This temperature dependence has not been explained[15].

The results of the measurements of the compositional dependence of the energy gaps can be utilized for fundamental study as well as for material characterization. We shall study the samples of $Hg_{1-x}Cd_xTe$ with $x \cong 0.2- 0.3$. The fundamental energy gap of the material in this composition range is around 0.2-0.3 eV which makes it suitable for infrared detection. Higher lying transitions are measured for characterization purposes since the measurements can be accomplished by working with conventional optical equipment in visible light. Higher lying gaps have been measured by various groups using methods of electro- and photoreflectance[16-20], ellipsometry[21] and normal incidence reflection[22]. At this point we shall introduce the conventional notation used for interband transition identification: the fundamental energy gap $(\Gamma_6-\Gamma_8)$ is denoted as E_0; $(\Gamma_7-\Gamma_8)$ transitions are called $E_0+\Delta_0$; $(\Lambda_{4,5}-\Lambda_6)$ are called E_1; $(\Lambda_6-\Lambda_6)$ are denoted $E_1+\Delta_1$; $(\Gamma_8-\Gamma_7)$ are called $E_0^{'}$; and (X_7-X_6) transitions are called E_2. The parameters Δ_0 and Δ_1 are the spin- orbit splitting energies at Γ and L (Λ) points. The E_1 and $E_1+\Delta_1$ transition energies are within the range

accessible to the visible light and thus are the ones often used for characterization purposes.

1.2 Vibrational Spectra.

One expects that HgTe and CdTe will have a vibrational spectrum consisting of 2 acoustical and 2 optical branches since the crystals have two atoms per unit cell. Transverse acoustical and optical modes (TA and TO) are doubly degenerate. Longitudinal acoustic and optic modes (LA and LO) are non- degenerate[1].

In this work we shall use the Raman scattering technique for the investigation of the vibrational spectra. Therefore the discussion of experimental results will lean toward Raman results rather than far infrared (FIR) absorption and reflection. Raman scattering technique measures the energies of the long wavelength optical phonons (optical phonons with near-zero wavevector ,i.e.$\vec{q}\cong 0$). In a diamond- structure crystal (such as Si) with inversion symmetry, optical branches of the phonon dispersion curve are triply degenerate at the Brillouin zone center (at $\vec{q}=0$). Polar materials with zincblende structure (such as HgTe and CdTe) do not have a center of inversion and the LO- TO degeneracy is lifted. The long range electric field associated with the long- wavelength LO phonons couples

with the vibrations and raises the energy of the LO phonons above that of the TO phonons at the zone center[23]. It is therefore expected that first- order Raman spectra of CdTe and HgTe have 2 peaks caused by TO and LO phonons. The LO and TO vibrations can be distinguished using polarization selection rules. Raman measurements of HgTe and CdTe were carried out by the workers of Refs.24 and 25.

The vibrational properties of the pseudo binary alloys of II-VI and III-V materials have been extensively investigated. They can be classified into two broad categories according to the compositional behavior of their vibrational spectra[26]. In the first class, known as amalgamated-type (or one- mode crystals), the pseudo binary alloy has the same number of LO and TO vibrational modes as the two parent compounds. The vibrational frequencies vary continuously with composition x. The spectral line intensities are also composition dependent in a continuous way.

$Hg_{1-x}Cd_xTe$ displays the second type of behavior which is called a persistent type (two-mode behavior)[24-26]. These crystals posess twice the number of LO and TO modes of the parent crystals. The frequency dependence of the modes have been found to be continuous. The modes which extrapolate to CdTe frequencies (for $x \cong 1$) are called "CdTe- like" modes. The

ones that extrapolate to HgTe (at $x \cong 0$) frequencies are called "HgTe- like" modes. As $x \rightarrow 1$ the "HgTe-like" vibrations degenerate into a single mode with the frequency of the vibrations of a single Hg impurity in CdTe. At $x \rightarrow 0$ the "CdTe- like" modes degenerate into a single mode belonging to a Cd impurity in HgTe.

The compositional dependence of the LO and TO phonons of $Hg_{1-x}Cd_xTe$ has been investigated using both FIR reflection[27,28] and Raman scattering techniques[26]. The results show that $Hg_{1-x}Cd_xTe$ displays a two-mode behavior.

In addition to the "two-mode" LO and TO modes, samples of HgTe and some samples of $Hg_{1-x}Cd_xTe$ display a number of features not expected of well behaved crystals[27-29] (see Fig.4). One of these features (labled "defect mode") has been assigned to vibrations of Hg atoms substituted on Te sites[28,29]. Another peak that has not been seen in any samples of CdTe or HgTe (labled "clustering mode") was detected by the workers of Ref.29. The origin of this feature is still somewhat controversial. Initially, this feature was thought to be a manifestation of the short- order clustering[29,30] - the mechanism put forth for III-V compounds in a similar case by workers of Ref.31. Recent calculations[32] done for the $x = 0.2$ material, however, show that a mode which is an integral part of the vibrational spectrum

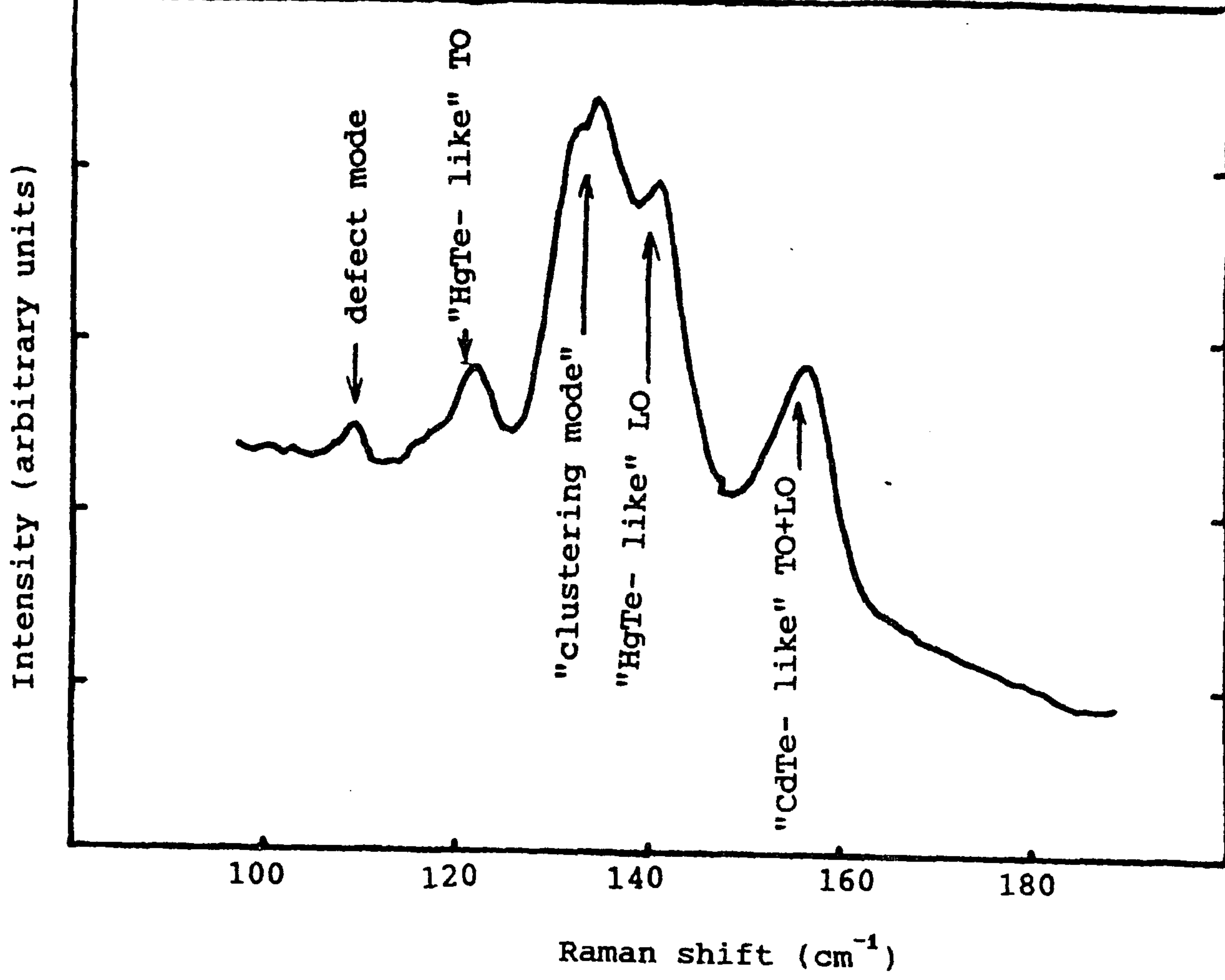

Fig.29 Raman spectrum of $Hg_{0.8}Cd_{0.2}Te$ (from Ref.21)

exists at the energy position of the "clustering mode". That casts doubt on the explanation that is based on the clastering mechanism.

1.3 Applications.

Aside from being interesting from the fundamental point of view, $Hg_{1-x}Cd_xTe$ has drawn a lot of attention as an infrared photodetector material. In principle, by choosing a suitable composition x, its variable energy gap can be tuned from 0 to 1.5 eV thus allowing a material with the desired spectral sensitivity to be obtained.

Turning to device applications, one finds a number of interesting physical problems. One such problem is the detection of surface trap states that will affect the carrier lifetimes and may drastically influence the performance of photodetectors. A new contactless method of detecting such surface states and deriving their lifetime from the frequency dependence of the photoreflectance (PR) signal has been developed by Shen, et al[33].

Another interesting physical problem concerns the physics of interfaces between $Hg_{1-x}Cd_xTe$ and insulators. The pseudo binary alloy $Hg_{1-x}Cd_xTe$ is rather unstable under room temperature conditions[5]. Mercury is known to

be the most volatile component of the alloy. A significant amount of Hg is always lost under free evaporation conditions from bare surfaces. To avoid the loss, the surface must be passivated. Thus the interface between $Hg_{1-x}Cd_xTe$ and the passivating insulator is an important part of many electronic devices. The insulating layer is also a functional element of metal-insulator- semiconductor (MIS) devices. Application of the insulating layer may create a significant number of interface states. These states can cause not only the carrier lifetime changes, but may also become charged - a condition which introduces uncertainty when attempting to bias the semiconductor surface by applying the external bias to the metal electrode of the MIS device.

As we have shown above, the study of the $Hg_{1-x}Cd_xTe$ and the parent binary materials presents a number of interesting questions - both in the applied and the fundamental fields - which will be addressed in this work.

CHAPTER II

Modulation Spectroscopy

2.1 Introduction.

Optical methods of the electronic structure of solids can produce a wealth of information about electronic energy bands and mechanisms of interaction of light with solids. Methods involving light reflection as opposed toabsorption allow the spectral regions where solids become opaque to be investigated . The reflectivity spectra exhibit features which can be attributed to the interband electronic transitions in solids at critical points thus yielding information about the electronic band structure. These features, however, are not always prominent and are usually obscured by the featureless background arising from the interband electronic transitions away from the critical points in the Brillouin zone.

Modulation spectroscopy is used to overcome these difficulties. The general idea is to create either an external perturbation that modulates the parameters of the sample or to modulate the incident beam parameters in a periodic fashion, and then to register the signal

component which alternates with the same frequency[34-37]. The signal can be proved to be proportional to a derivative of the reflectivity over the energy of light[34-37]. The spectrum thus obtained has sharper features than the reflectivity spectrum and may contain features not resolved in the reflectivity spectra at all[38].

Since the differential spectrum contains no background from transitions away from the critical points, the theoretical explanation of the spectra need only be concerned with the reegions immediately surrounding the critical points in the Brillouin zone. This presents a vast simplification over consideration of all transitions in the Brillouin zone required in the case of reflectance spectra. Electromodulation method in particular produces features so sharp (proportional to the third derivative of reflectivity over energy) and so strong that it has quickly gained popularity as a relatively simple and inexpensive method of characterizing semiconductor materials, structures and devices[39]. The following discussion concentrates on the electromodulation techniques employed in this work.

2.2 Interaction of Light With Condensed Matter.

The fundamental quantity which describes the

response of matter to the incident electromagnetic field is the complex dielectric function[34,40,41] $\varepsilon(\omega)$:

$$\varepsilon(\omega)=\varepsilon_1(\omega) + i\varepsilon_2(\omega) = N^2 \qquad (1a)$$

where ε_1 and ε_2 are the real and imaginary parts of ε and N is the complex refractive index of the material, i.e.,

$$N = n + ik \qquad (1b)$$

where n and k are the real and imaginary parts of N. The real and imaginary parts of the refractive index N are related to those of the dielectric function ε by:

$$\varepsilon_1 = n^2 - k^2 \qquad (2)$$

$$\varepsilon_2 = 2nk \qquad (3)$$

For near-normal incidence the reflectivity at discontinuous interface between two different homogeneous media (substrate and ambient) can be written using Fresnel formulae[42] as:

$$R = \frac{|N - N_a|^2}{|N + N_a|^2} \qquad (4)$$

where N and N_a are the refractive indices of the material and the ambient, respectively. The formulae Eqs.(2-4) show that singularity in $n(\omega)$ (or $k(\omega)$) will cause singular behavior of $R(\omega)$ which can be detected experimentally. The singularities in $n(\omega)$ (or $\varepsilon(\omega)$) can in turn be explained in terms of the interband optical transitions at critical points.

The dielectric function exhibits features which are due to the singularities in the combined density of states at certain points in the Brilluoin zone known as Van Hove singularities[43]. The imaginary part of the dielectric function ε_2 due to a given pair of valence and conduction bands is given by an integral in the wavevector space ($\vec{k}$- space)taken over the surface $E_{cv}=\hbar\omega$[35]:

$$\varepsilon_2 = (Q/\omega^2) \int_{E_{cv}=\hbar\omega} \frac{ds}{|\nabla_k E_{cv}(\vec{k})|} |\hat{e}\cdot\vec{P}_{cv}|^2 \qquad (5)$$

where: $E_{cv}(\vec{k})= E_c(\vec{k})-E_v(\vec{k})$ is the interband energy; $\vec{P}_{cv}$ is a matrix element of electron- radiation interaction between a given pair of conduction (c) and valence (v) bands; $\hat{e}$ is the unit vector in the direction of the incident electric field; ∇_k denotes gradient in k- space and

$$Q = (2/2\pi^3)(4\pi^2 e^2/m^2) \qquad (6)$$

where e and m are the electron charge and mass, respectively. The integration is to be carried out in a wavevector space on a constant energy surface given by the condition $E_{cv} = \hbar\omega$. The real part of the dielectric constant can be found using the Kramers- Kronig relation:

$$\varepsilon_1 = 1 + (2/\pi)P \int_0^\infty \frac{\omega'\varepsilon_2(\omega')}{\omega'^2 - \omega^2} d\omega' \qquad (7)$$

Assuming that the matrix element $\vec{P}_{cv}$ is a smooth function of the wavevector k we find[41] that discontinuities in the dielectric function occur whenever the gradient of the interband energy in k-space vanishes, i.e.,

$$\nabla_k E_{cv}(\omega) \equiv \nabla_k [E_c(k) - E_v(k)] = 0 \qquad (8a)$$

Points in $\vec{k}$- space for which Eq.(8) is satisfied are called the critical points (CP's). They occur usually at high symmetry points where $\nabla_k E_C(k) = \nabla_k E_v(k) = 0$ and along the high symmetry directions in the Brillouin zone (BZ) where

$$\nabla_k E_c(\omega) = \nabla_k E_v(k) \neq 0 \qquad (8b).$$

To classify the types of the critical points let us expand the interband energy as a function of the wavevector around a critical point:

$$E_{cv} = E_{cv}(k) + \frac{1}{2} \sum_{i,j} \left(\frac{\partial^2 E_{cv}(k)}{\partial k_i \partial k_j}\right)\Bigg|_{k=k_c} \cdot (k_i - k_{ci})(k_j - k_{cj}) + \ldots \qquad (9)$$

where indexes i and j stand for the coordinate axes x, y and z. There is no linear term near the $\nabla_k E_{cv} = 0$ point.

If we deal with a high symmetry point in a BZ for which Eq.(8) holds, then $E_{cv}(k)$ depends on all three

components of the wavevector near this point. Then the critical point is called a 3- dimensional (3D) CP. Choosing a coordinate system which diagonalizes Eq.(9) we obtain for a 3D CP:

$$E_{cv} = E_g + \frac{\hbar^2}{2}\left[\frac{(k_x - k_{xc})^2}{m_x^*} + \frac{(k_y - k_{yc})^2}{m_y^*} + \frac{(k_z - k_{zc})^2}{m_z^*} \right] \quad (10)$$

where $E_g \equiv E_{cv}(k_c)$ and the effective masses m_x^*, m_y^*, and m_z^* are defined by:

$$\frac{1}{m_i^*} = \frac{1}{\hbar^2}\left(\frac{\partial^2 E_{cv}}{\partial k_i^2}\right), \; i=x,\ y,\ z \quad (11)$$

If one of the effective masses is very large, only two terms in square brackets on the right side of Eq.(10) are important. This often happens along high symmetry lines in the Brillouin zone or when the electrons are confined in a sheet- like configuration. In this case we have a two- dimensional CP (2D CP)

Four types of 3- dimensional critical points can occur between two nondegenerate bands[41]. If all the effective masses are positive, the critical point is a minimun (M_0). If one or two of the masses are negative, we have a saddle point (called (M_1) or (M_2) correspondingly). A maximum (M_3) corresponds to all negative masses.

It can be shown[34,35,41,44] that the singular part of the dielectric function has the form

$$\varepsilon(\omega) \propto e^{i\phi} (E-E_g+i\Gamma)^n \tag{12}$$

where ϕ is a phase angle and Γ is a broadening parameter. The exponent n has value -1/2 for 1D CP, 0 (logarithmic dependence) for 2D CP and 1/2 for 3D CP. The transitions between descrete exciton levels produce the Lorentzian lineshape with n=-1.

2.3 Modulation Techniques

The common feature of "external" modulation techniques is that a sample parameter is modulated in a periodic fashion and the component of reflectivity with the same frequency (ΔR) is measured. This component - normalized to the dc part of reflectivity (R) - then is registered. The registered signal can be written as[45]:

$$\frac{\Delta R}{R} = \alpha(\varepsilon_1,\varepsilon_2)\Delta\varepsilon_1 + \beta(\varepsilon_1,\varepsilon_2)\Delta\varepsilon_2 \tag{13}$$

This relation can be derived by differentiating the Fresnel formula for the normal incidence reflection. The Seraphin[45] coefficients α and β are functions of photon energy, and their sign and relative magnitude determine the lineshape in different spectral regions.

Suppose that the parameter of the crystal that is modulated affects the energy gap E_g and/or the broadening parameter Γ. Consider the change in ε when

such a perturbation is applied to the crystal:

$$\frac{\Delta\varepsilon}{\Delta\xi} = \left[\frac{\partial\varepsilon}{\partial E_g}\frac{dE_g}{d\xi} + \frac{\partial\varepsilon}{\partial\Gamma}\frac{d\Gamma}{d\xi}\right] \propto e^{i\phi}(E - E_g + i\Gamma)^{n-1} \qquad (14)$$

Here ξ is the modulated parameter (yet unspecified) and $\Delta\xi$ is the modulation amplitude. The expression Eq.(14) shows that $\Delta\varepsilon$ is proportional to the first derivative of the dielectric function over the energy. This expression adequately describes the modulation spectra when the modulation does not destroy the translational symmetry of the crystal. It has equal application for temperature, uniaxial stress, hydrostatic, and pressure[34,46] modulation.

The above-mentioned types of modulation have one thing in common: they result in a small change of the band structure of the crystal. The electron (and hole) distribution is unperturbed by the modulation. Although the band structure parameters change as a result of the modulation, the carriers adjust to the changes rapidly. Terefore, the carriers have an equilibrium distribution at any given moment.

Application of the electric field as the modulating perturbation will have quite a different effect. There will, of course, be some modulation of the bandgap due to the Stark effect leading to the modulation of the type described by Eq.(14). A much stronger modulating effect, however, will be caused by

the acceleration of electrons in the electric field perturbing their energy distribution[35-39]. We shall follow the treatment of the effect suggested by Shen and Pollak[47] which is mathematically simple (though not rigorous) and physically transparent.

Being accelerated by the electric field $\mathcal{E}$ for the duration of time t the electron gains energy δE:

$$\delta E = e^2 \mathcal{E}^2 t^2 / 2m_{\parallel}^* \tag{15}$$

where $m_{\parallel}^*$ is the effective mass of the electron in the direction of the electric field. Averaging the energy gain over the -t/2 to t/2 period, we get

$$\delta E = e^2 \mathcal{E}^2 t^2 / 24m_{\parallel}^* \tag{16}$$

then the change in the dielectric constant due to application of the field $\mathcal{E}$ is:

$$\Delta\varepsilon = \varepsilon(E+\delta E,\Gamma) - \varepsilon(E,\Gamma). \tag{17}$$

In the low field regime, i.e.

$$\delta E < \Gamma \tag{18}$$

we can make a Taylor's series expansion:

$$\Delta\varepsilon = \delta E \left(\frac{d\varepsilon(E,\Gamma)}{dE}\right) = \frac{e^2 \mathcal{E}^2 t^2}{24m_{\parallel}^*} \cdot \frac{d\varepsilon(E,\Gamma)}{dE} \tag{19}$$

Now let us substitute quantum- mechanical operator $i\hbar(d/dE)$ for time t. Eq.(19) becomes:

$$\Delta\varepsilon = \frac{1}{3} (\hbar\Omega)^3 \left(\frac{d^3\varepsilon(E,\Gamma)}{dE^3}\right) \tag{20}$$

where

$$(\hbar\Omega)^3 = e^2 \mathcal{E}^2 \hbar^2 / 8m_{\parallel}^* \tag{21}$$

is the characteristic electro- optic energy of the system.

The electric field- induced change of the dielectric function is, therefore, proportional to the third derivative of the ϵ with respect to energy. Thus the electro- modulation spectra must give sharper structures than the first- derivative techniques (Eq.(14)). From the above equation it also follows that in a low- field regime the lineshape $\Delta\epsilon$ simply scales without distortion as the square of the modulating field amplitude . The expression Eq.(18) gives the limit for the low field regime. If we take $t = \tau = h/\Gamma$ to be the average collision time, then the energy gain prior to collision will be:

$$\delta E = e^2 \mathcal{E}^2 t^2 / 24 m_{\parallel}^{*} = (\hbar\Omega)^3 / 3\Gamma^3 \qquad (22)$$

and the low field limit condition becomes:

$$(\hbar\Omega)^3 / 3\Gamma^3 < 1/3 \qquad (23)$$

Thus the above description is valid whenever $\hbar\Omega < \Gamma$. As a rule of thumb, whenever $\Delta R/R < 10^{-4}$, the sample is in low- field regime. But it is useful to check the regime using the following simple rule: experimentally, the low field regime is recognized by the lineshape scaling as $\mathcal{E}^2$.

According to Eqs.(13,20) the signal $\frac{\Delta R}{R}$ resulting from the electromodulation in a low- field regime will be proportional to the third derivative of the

dielectric function. This lineshape is called the third derivative functional form (TDFF). Taking a particular example of the 3D CP using Eqs.(12,13,20,21) we find for TDFF:

$$\frac{\Delta R}{R} \propto L(E,\Gamma) = \frac{1}{E^2}\mathrm{Re}[Ce^{i\theta}(E - E_g + i\Gamma)^{-5/2}] \quad (24)$$

where C is a proportionality coefficient and $L(E,\Gamma)$ is the lineshape function. Since its conception by Aspnes et al[35-37], the TDFF has been used successfully to describe the electromodulation spectra of the group IV and III-V materials[48].

Recently, Raccah, et al[17,18] have reported that in $Hg_{1-x}Cd_xTe$ with a high defect density ($\cong 10^5$ etch pits per cm^2), the electrolyte electroreflectance (EER) spectra contain contributions from the first- and second derivative terms as well as the usual third- derivative functional form. They have ascribed these additional terms to the electrostriction and polarization of defects by the modulating electric field. These authors have found that in $Hg_{1-x}Cd_xTe$ and related materials with high defect density, a generalized functional form (GFF) must be employed to fit the EER spectra. The lineshape of the GFF is given by[17,18]

$$L(E,\Gamma) = \sum_{j=1}^{p} C_j E^{-2}[(\hbar\Omega_j)^3 L(E,5/2)$$

$$- 4\Delta\sigma^2 L(E,3/2) - 4\Delta E_j L(E,1/2)] \quad (25a)$$

where

$$L(E,n/2) = \cos\left(\Omega_j - \frac{n\Phi}{2}\right)\left[(E - E_{g,j})^2 + \Gamma^2\right]^{-n/4} \quad (25b)$$

with

$$\Phi_j = \tan^{-1}[\Gamma_j/(E - E_j)] \quad (25c).$$

In Eq.(25a) the term $(\hbar\Omega)^3$ is given by Eq.(21) and p is the number of CP's under considerstion. The term $\Delta\sigma^2$ results from polarization of the defects by the modulating electric field, while ΔE_j can arise from piezoelectric strain in non- elemental semiconductors. Note that in Eqs.(25) the term L(E,5/2) is equivalent to Eq.(24) while the other terms L(E,3/2) and L(E,1/2) are related to the second and first derivatives of the dielectric function respectively.

To analyse electromodulation lineshape using TDFF - parameters C, E_g, Γ and θ of Eq.(24) are varied until the best fit is achieved. When using the GFF, the parameters C_j, $\Delta\sigma^2$, ΔE_j, $E_{g,j}$, Γ_j and Ω_j of Eqs.(25a) and (25b) are varied. Assuming a fit to a single critical point: in the case of GFF, there are 2 more variable parameters available than in the TDFF case. Hence it is not surprising that GFF gives good fit to a wider variety of lineshapes than TDFF.

2.4 Electromodulation Methods

2.4.1 Electroreflectance.

There are contact and contactless methods based on electromodulation. Photoreflectance[49] and electron beam electroreflectance[50] are examples of contactless methods. Electrolyte electroreflectance (EER) is a contact technique. In this method the sample is immersed into a cuvette with electrolyte. The modulating voltage is applied between the sample and the Pt counter electrode which is also immersed into electrolyte. This creates an electric field near the sample surface and thus the electromodulation is achieved. The probe light beam is aimed at the sample through a transparent window or a transparent wall of the cuvette.

Another (contact) modification of electromodulation is electroreflectance (ER) in a metal-insulator- semiconductor (MIS) configuration.[51] The device gate must be semitransparent. The electric field is supplied by the modulating voltage at the gate of the device. The light beam is aimed at the sample surface through the semitransparent gate. Apparently, the EER method is simpler to implement, whereas the ER in a MIS configuration allows for a much greater temperature range. We use the latter method in this work.

2.4.2 Photoreflectance

A completely contactless way to induce the modulating electric field in semiconductors was found by Wang, Albers and Bleil[49]. They used a second intense beam of light from the laser (pump beam) to intermittently illuminate the surface. They observed the modulated component of reflectance which, as they proved, was due to the modulation of the surface electric field by the light. This method later received the name of photoreflectance (PR).

The predominant mechanism of PR in bulk semiconductors is a reduction of the surface (interface) field through a recombination of the minority carriers with a charge in the surface (interface) states[52,53]. This mechanism is shown schematically in Fig.5 for a n-type semiconductor. In the pump-off state there exists some bandbending (which may be caused by the surface states) which leads to a certain surface electric field. In the pump- on state the strong pumping beam generates the electron- hole pairs at the surface (depth of the generation depends on the penatration depth of the light). These pxotoexcited holes drift toward the surface and recombine with the

Secondary light source <u>off</u>

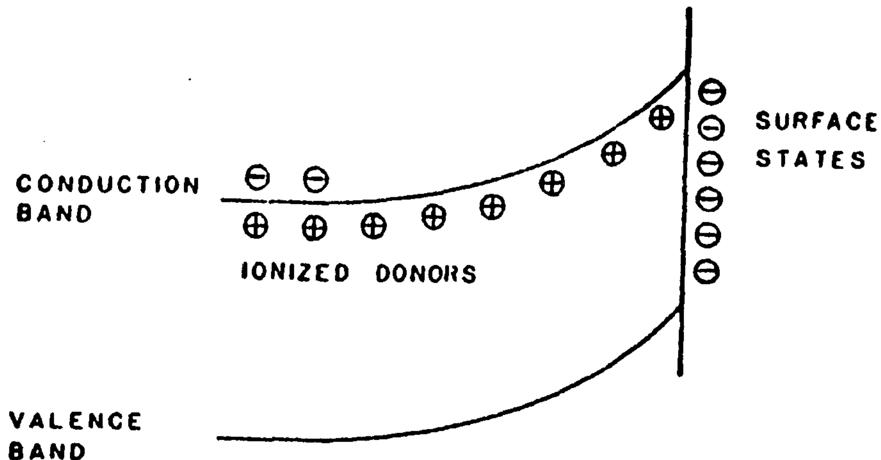

Secondary light source <u>on</u>

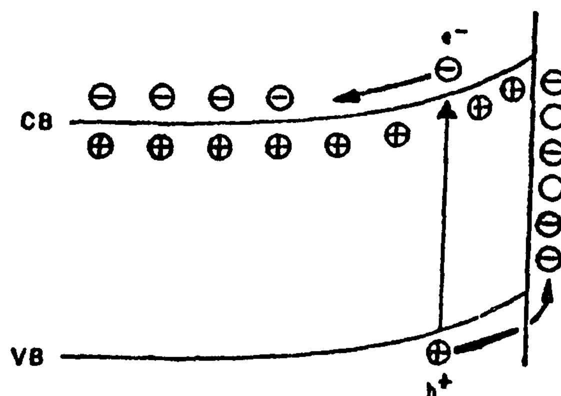

Fig.5

Mechanism of the electric field modulation by light. The bandbending caused by the negatively charged surface states (upper portion of the figure) is reduced when part of the states is neutralized by photogenerated holes.

electrons trapped in surface states thus reducing the band bending (and the surface electric field). During the pump- off part of the cycle the system returns to the initial state. Thus a variation of the electric field necessary for the measurement of the elecromodulation spectrum is accomplished.

The presence of charged surface states is crucial for PR measurements, since they cause the initial band bending. Furthermore, the kinetics of the minoritiy carrier generation- recombination is the main factor determining the PR signal amplitude. Therefore information on the characteristic trap times can be obtained from PR spectra.

Recent studies by Shen et al[54] suggest that not only surface traps, but also bulk traps can participate in the process of creating the modulating electric field. Therefore, aside from the measurements of the electronic band structure parameters, the PR measurements can provide information on both bulk and surface trap states.

It is possible to conduct PR measurements in contact configuration. In this case the initial band bending may be supplied by an external electric field with the result that the presence of the surface states is not crucial for the PR effect. We shall not discuss this mechanism in detail, since we do not use the

contact modification of PR in this work.

2.4.3 Experimental Details

The diagram of the ER setup is shown in Fig.6. Light from a 150 Xe arc lamp is passed through a monochromator (PTI model 01-002). The monochromatic light is focused onto the sample by means of either a spherical mirror or a lens. The modulating voltage (square wave with frequency ≅ 200 Hz) is supplied by a function generator (HP model 3311a), which also provides the reference signal for the lock- in amplifier (SR-510 by Stanford Research Systems).

The application of the modulating voltage to the sample in the case of EER and ER in the MIS configuration has been described above. The incident light is passed through the neutral density filter. The filter is driven by the computer to achieve servoing action, which will be described later in detail. The light is then collected by the photodetector, using an additional lens if necessary. We have used a number of photodetectors: photomultiplyer tubes (PMT with S-1 response for 8000-11000 Å or S-20 response for 2000-8500A spectral regions) and a silicon photodiode (EG&G HUV-2000B). The computer (IBM XT) controls the monochromator scanning and collects and processes data

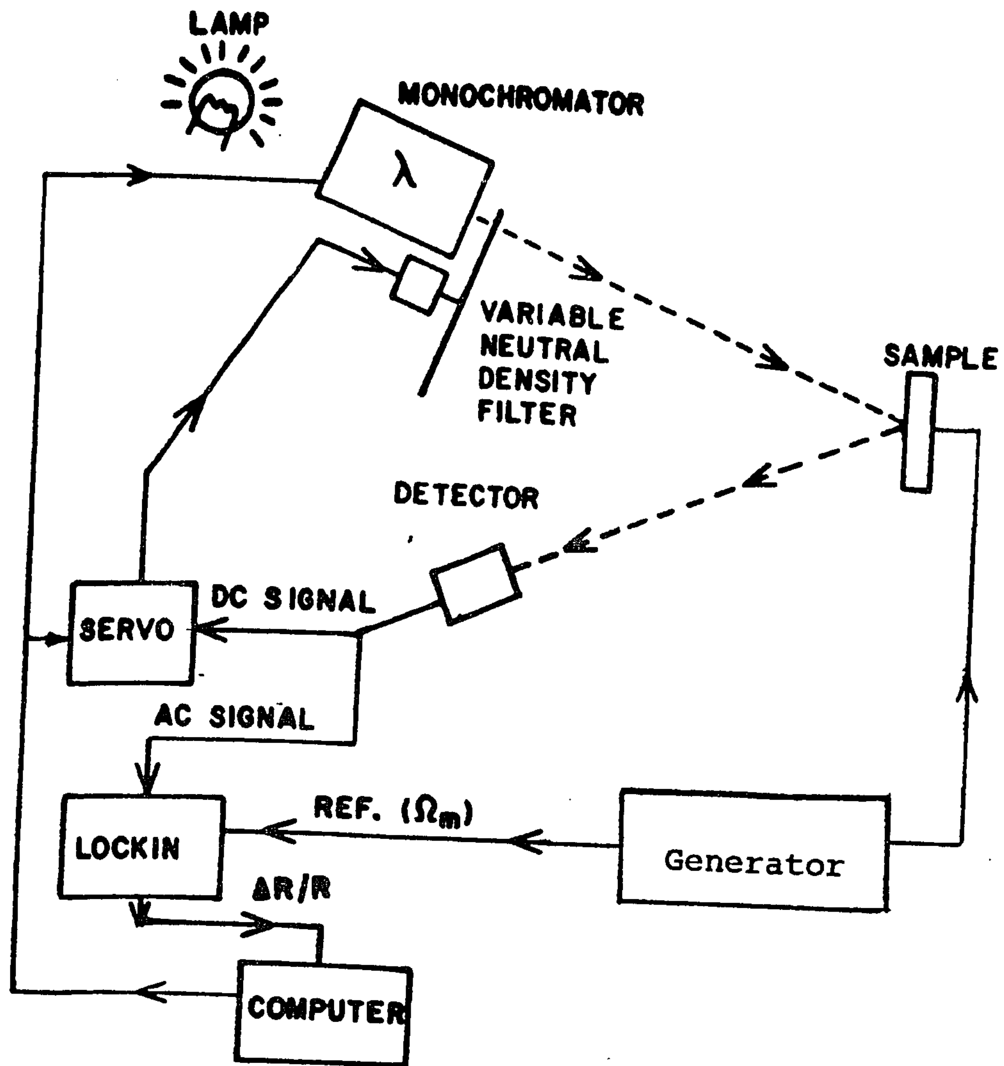

Fig.6

Electroreflectance setup.

from the detector.

We shall now describe the data aquisition and servo functions of the setup.

The intensity of light reflected from the sample has a constant component I_{dc} (received by the computer from the detector) which is equal to:

$$I_{dc} = I_0 R \qquad (26a)$$

where I_0 is the intensity of the incoming beam. The computer also receives the voltage proportional to the alternating component ΔI caused by the modulation from the lock- in amplifier. This component can be written as:

$$\Delta I = I_0 \Delta R \qquad (26b)$$

Performing the numerical division the computer obtaines the final result:

$$\Delta I / I_{dc} = \Delta R / R \qquad (26c)$$

However, letting the I_{dc} part of the intensity vary will have an effect on the ac sensitivity of the detector. If I_{dc} becomes too large, the detector will 'saturate' and become completely insensitive to the alternating component. To alleviate this problem, the computer drives the neutral density filter to obtain a constant value of the I_{dc} (preset by operator).

The diagram of the photoreflectance setup is presented in Fig.7. The ER setup, with minor modifications, was used for the PR experiment. The main

difference between the two is the part which produces the electromodulation. In the PR setup the modulation is produced by the laser beam incident on the sample surface. The pump beam is chopped to alternate the magnitude of the electric field at the surface. The lock- in amplifier is synchronized to the chopper.

The laboratory is equipped with the Innova-K1000 Kr laser and CR-6 Ar laser (both by Coherent, Inc.) and a number of low- power (up to 5 mW) He-Ne lasers by Metrologic Inc. We used laser lines of different wavelengths - the use of particular lines will be discussed later.

The only modification in the optical path of the probe beam is the filter (long- or band pass) placed between the sample and the detector. The filter is needed to cut off the light produced by the scattering of the pumping beam from the sample surface. Without the filter scattered light would reache the detector, the constant ac component of the signal would be picked up by the lock- in amplifier and recordered as a part of the signal.

The pump beam leakage places limitations on the pumping power that may be used. The constant background signal does not present a problem in, itself, since it can be subtracted instrumentally or digitally. It is,however, the spurious variation of the background

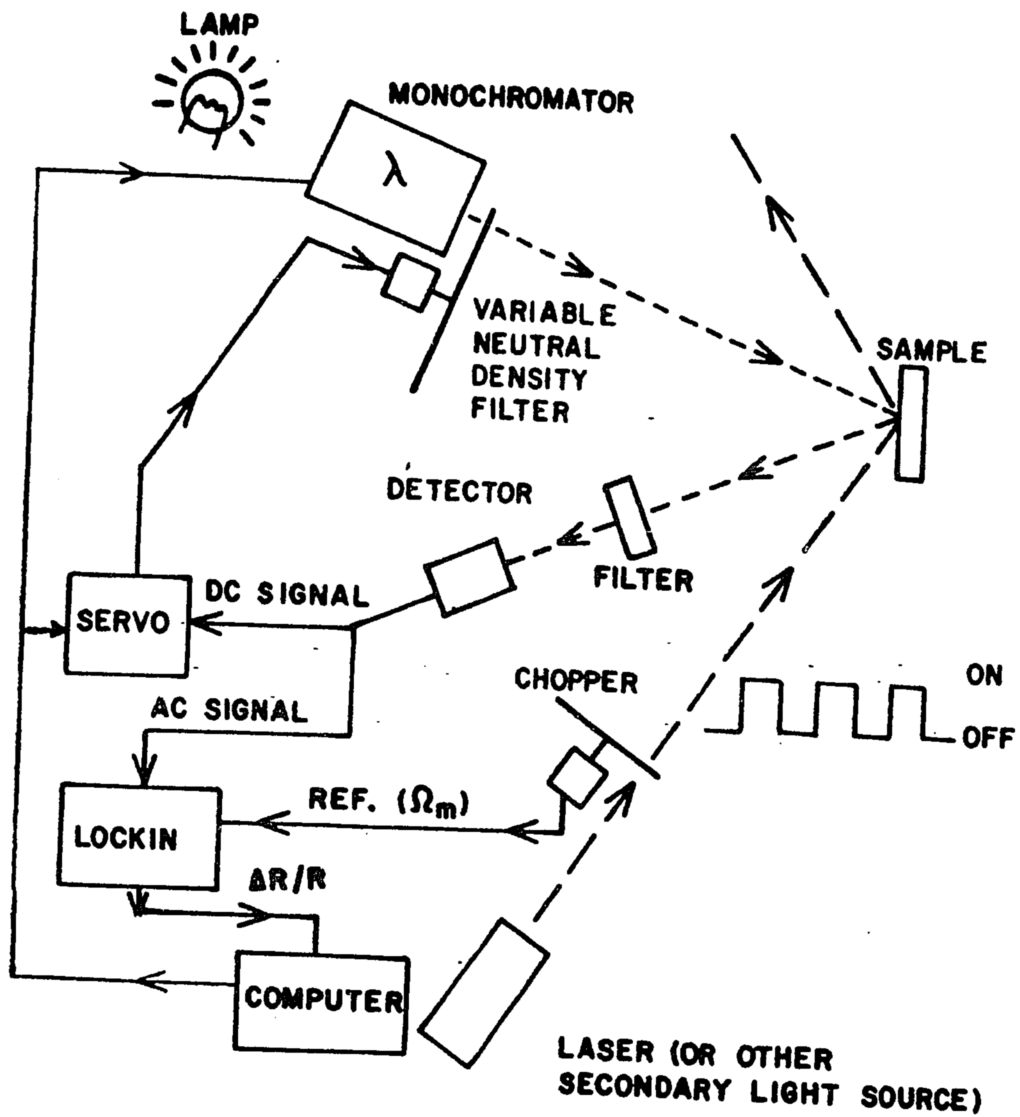

Fig.7

Photoreflectance setup

that can not be eliminated and must be considered when choosing the power of the pumping beam. A further consideration, when choosing the pumping power, is the heating of the sample, which must be avoided because at a certain level one may start seeing the thermomodulation spectrum rather than electromodulation one. Another situation in which the sample heating must be avoided is when the temperature of the surface is considered important. The scattering of the pump beam from the surface of the samples we used was so large that we could not use a pumping power density higher than 10 mW/cm^2 which is not enough to heat the sample to cause the last two problems discussed.

CHAPTER III

Results and Discussion- Modulation Spectroscopy

3.1 Review: Dependence of the Electronic Transition Energies of $Hg_{1-x}Cd_xTe$ on Composition and Temperature.

The compositional dependence of the electronic transition energies has been a subject of both theoretical and experimental investigation. To explain such dependence, the virtual crystal approximation (VCA) is most commonly used. In this approximation the effect of alloying is averaged over the lattice sites. The cation potential in $A_{1-x}B_xC$ material ($\bar{V}_x$) is replaced by a weighted average of the cation potentials in AC and BC compounds (V_a and V_b):

$$\bar{V}_x = xV_a + (1-x)V_b \quad (27)$$

and the calculations are done following the same schemes as as those applied to parent binary compounds.

According to Eq.(27) $\bar{V}_x$ is linear in composition x. However, the energy gaps are not linear functions of the potential $\bar{V}_x$. Thus, in band structure calculations the energy gaps are non-linear functions of composition x. Therefore, the variation of the energy gaps generally is not expected to be linear in x. The compositional

variation of the energy gaps can be described by an empirical nonlinear relation[5]:

$$E_i=a_i+b_i x+c_i x^2=a_i+b_i' x+c_i' x(1-x). \qquad (28)$$

The deviation from linearity is described by the bowing parameter c_i.

However, in many cases the experimental values of c are considerably larger than the theoretical numbers. This difference is generally ascribed to alloy potential fluctuations not taken into account in the VCA calculations.

Band structure calculations done for $Hg_{1-x}Cd_xTe$[3,4,11] predict nearly linear dependence of the fundamental energy gap on the composition x. Also, a great number of experimental measurements of the fundamental energy gap in $Hg_{1-x}Cd_xTe$ material has been done utilizing optical absorption[12], magnetoabsorption[13] and other techniques[14]. The compositional dependence of the fundamental energy gap proved to be very close to linear. For example, the results of Ref.13 can be fitted well to the expression which is linear in x:

$$E_0(x,T)=-0.30+5\cdot 10^{-4}T+(1.91-10^{-3}T)\cdot x \quad \text{(Ref. 13)} \qquad (29)$$

The measurements indicate that at $x\cong 0.15$ at 77K the reversal of the Γ_6-Γ_8 order occurs causing the semiconductor - semimetal transition.

The importance of disorder in understanding the

band structure of $Hg_{1-x}Cd_xTe$ is best illustrated on the higher lying critical points for which the compositional dependence of energy deviates significantly from linearity. Several groups attempted to obtain theoretically the correct bowing parameter for the E_1 and $E_1+\Delta_1$ critical points. The experimental values of the bowing parameter, found in literature, fall in a range 0.6 eV to 0.86 eV.

A comparison of the above experimental data with two empirical pseudopotential calculations can be made. Value of the bowing parameter obtained in VCA approximation by workers of Ref.21 for the E_1 transition is $C_{VCA}(E_1)$= 0.28 eV which is significantly lower than the experimentally observed values. This group employed the empirical pseudopotential method. Workers of Ref.12 used the coherent- potential āpproximation which takes into account the potential fluctuations. The value of the bowing parameter obtained by this group is $C(E_1)$=0.71 eV, which is very close to experimental values (see Table I). This supports the view that only a part of the bowing can be explained by the VCA approach and that disorder effects must be considered to explain the compositional dependence of the energy gaps in pseudo binary alloys.

The understanding of the compositional dependence of energy gaps is important for the material

Table I

Compositional dependence of the E_1 and $E_1+\Delta_1$ electronic transition energies in $Hg_{1-x}Cd_xTe$.

Critical point	a (eV)	b (eV)	c(eV)
E_1	2.147±0.005[a] 2.15[b]	0.44±0.02[a] 0.35[b]	0.7±0.1[a] 0.86[b]
$E_1+\Delta_1$	2.778±0.005[a]	0.47±0.02[a]	0.6±0.1[a]

Values of parameters a, b, and c of Eq.(28) obtained by fitting the compositional dependence of the E_1 and $E_1+\Delta_1$ transitions. All data taken at room temperature.

a- Results from Ref.21

b- Results from ref.16.

characterization. In Table I we have compiled some data on the compositional dependence of the E_1 and $E_1+\Delta_1$ critical points. In this work we shall compare the measured E_1 transition energy in $Hg_{1-x}Cd_xTe$ to the known compositional dependence (Table I) in order to determine the composition.

The dependence of the band structure of semiconductors on temperature is another interesting field of study. Experimental studies of the fundamental band gap[12,13] and higher lying critical points[19,56,57] have been performed by a variety of methods.

Theoretical investigations have been generally directed toward obtaining the temperature dependence of the energy gaps, since these are the quantities most commonly measured in experiments. It is recognized that the temperature dependence consists of two components: one is caused by the thermal expansion (lattice dilation term); and, the other results from changes in the lattice vibration spectrum that affect electron energies through the electron- phonon interaction[5,15]:

$$\left.\frac{\delta E_g}{\delta T}\right|_{tot} = \left.\frac{\delta E_g}{\delta T}\right|_{dil} + \left.\frac{\delta E_g}{\delta T}\right|_{el-ph.} \qquad (30)$$

The effect of thermal expansion can be taken into account by relating it to the pressure coefficient of the energy gap $\frac{\delta E_g}{\delta P}$:

$$\left.\frac{\delta E_g}{\delta T}\right|_{dil} = \left(\frac{\delta E_g}{\delta P}\right)\left(\frac{\delta P}{\delta \Delta}\right)\left(\frac{\delta \Delta}{\delta T}\right). \quad (31)$$

Here $\Delta \equiv \frac{\delta V}{V}$ is the dilation; $\frac{\delta P}{\delta \Delta}$ is the compressibility; and $\frac{\delta \Delta}{\delta T}$ is the thermal expansion coefficient. Since each of these quantities is measurable, the dilation term can be determined from the measurements. Typical value of this term for the semiconductor materials is:

$$\left.\frac{\delta Eg}{\delta T}\right|_{dil} = 10^{-4} - 10^{-3} \text{ ev/K}. \quad (32)$$

For many semiconductors ($Hg_{1-x}Cd_xTe$ included), the dilation term provides for about one half of the temperature dependence of the gaps. Therefore, the vibrational component is of the same order as the dilation component. This component has been the subject of active investigation for a number of years. Several ways of treatment were proposed[15].

In 1951 Fan calculated the electron- phonon term as a shift of the electron energy arising from emission and absorption of phonons by electrons. A number of workers followed this approach with improvements mainly directed toward more accurate computation of the matrix element for the electron- phonon interaction.

Another line of investigation is to introduce temperature- dependent corrections to the lattice

potential during the band structure calculations. In 1955 Antonchic - and later Brooks and Yu did it within the frame of pseudopotential technique by introducing temperature dependent form- factors. Yet another approach was explored by Brooks in 1955 and later by Heine and Van Vechten. They relate the energy gap change to change in the lattice vibrational frequencies when an electron gets excited across the gap.

Recently, a number of successful theoretical calculations have been published for the group IV and III-V materials based on the pseudopotential calculations[58]. These calculations not only incorporate the temperature dependent form factors, but also included the self- energy term which contributes considerably tothe temperature shift of the fundamental energy gap. This type of calculations has not yet been done for the $Hg_{1-x}Cd_xTe$.

Apparently, computation of the vibrational contribution to the temperature dependence of the energy gap is closely related to understanding the electron-phonon interaction and the interdependence of the vibrational and electronic spectra of solids. Therefore, it is extremely important to have accurate data on the temperature dependence of the energy gaps available for comparison with theory. The temperature dependence can be closely approximated[58] by the non-linear dependence

introduced by Varshni[59]:

$$E_g(T) = E_g(0) + \frac{\alpha T^2}{(T+\beta)} \qquad (33)$$

where α and β are constants and $E_g(T)$ and $E_g(0)$ are values of the energy gap at temperature T and 0 K correspondingly. We shall use Eq.(33) to describe our results.

The theoretical calculations of the $\frac{\delta E_g}{\delta T}$ are generally quite successfull[15]. The results prove incorrect, however, for the fundamental energy gap of $Hg_{1-x}Cd_xTe$. The experimental values of $\frac{\delta E_g}{\delta T}$ vary through the composition range in the following manner[15]:

$$\frac{\delta E_g}{\delta T} = \left\{ \begin{matrix} x=1 & x\cong 0.5 & x=0 \\ -6 & \cong 0 & 5\cdot 10^{-4}\ \frac{eV}{K} \end{matrix} \right\} \qquad (34)$$

where $E_g = E(\Gamma_6) - E(\Gamma_8)$. The theoretical calculations tend to give the wrong sign for the dependence on the HgTe end of the alloy range. The temperature dependence of other energy gaps are not so peculiar. They are, however, important for a further understanding of the problem. To contribute to the further understanding of this question, we shall measure the temperature dependence of the E_1 gap and transition for $x\cong 0.3$ material. We shall also measure the temperature dependence of E_0 and E_1 energy gaps in CdTe.

3.2 Electroreflectance of $Hg_{1-x}Cd_xTe$ in a Metal-Insulator- Semiconductor Configuration.

3.2.1 Sample Preparation.

Our samples (# RCS-245-4 and ZH-245-3GB) were prepared by Santa Barbara Research Center. The substrates were bulk $Hg_{1-x}Cd_xTe$ with composition x=0.3 (as derived from the growth conditions) grown by the horizontal zone melt. The substrates were chemomechanically polished using a Br_2 solution treatment. The MIS structures were formed by a deposition of 1500 Å of Photox™-SiO_2[60] followed by a 60-Å semitransparent gate.

3.2.2 Temperature Dependence of the E_1 Transition of $Hg_{1-x}Cd_xTe$

In this section we report on our investigation of the temperature dependence of the E_1 transition energy and broadening parameter of $Hg_{1-x}Cd_xTe$ (with the nominal composition x=0.3) using the ER measurements in aMIS configuration. The temperature range was 77- 293 K.

The ER spectra of the sample RCS-245-4 were

Table II

Experimental values of the E_1 transition energy and broadening parameter for $Hg_{1-x}Cd_xTe$ with x=0.3 MIS sample (RCS-245-4) at different temperatures.

T(K)	E_1 (eV)	Γ_1 (meV)
78	2.474 ± .003	62 ± 2
95	2.470 ± .003	70 ± 2
115	2.463 ± .004	76 ± 2
135	2.451 ± .005	76 ± 3
155	2.446 ± .005	81 ± 3
175	2.439 ± .006	82 ± 4
195	2.425 ± .006	85 ± 4
215	2.410 ± .007	93 ± 5
235	2.404 ± .008	92 ± 6
255	2.396 ± .008	96 ± 6
275	2.388 ± .009	103± 7
293	2.384 ± .009	105± 8

taken at eleven different temperatures in E_1 spectral region. The modulation voltage of 2 V peak- to- peak and dc bias of -10 V were used during the measurements. The necessity of this dc bias will become apparent in the ensuing discussion. In the Fig.8 we show the experimental ER spectra at 77 K and 293 K (points). Since the fit to TDFF was not good, we have used the least- squares fit of our spectra to the GFF lineshape to derive the transition energy and broadening parameter. The solid lines in Fig.8 represent the fit results. The values of E_1 and Γ obtained by the least square fit for different temperatures are shown in Table II.

The temperature dependence of the E_1 band gap was fitted by the Varshni relation (Eq.(33)),yielding the follwing parameters:

$$\alpha = -(5.0 \pm 0.2)\cdot 10^{-4}\ \frac{eV}{K} \qquad (35a)$$

$$\beta = 66 \pm 10\ K$$

$$E_1(0) = 2.50 \pm 0.03\ eV$$

The temperature dependence of the transition energy is plotted in Fig.9 (points) along with the fit to Varshni relation (solid line).

The fit to a linear dependence was performed to facilitate the comparison with the available data. It yielded:

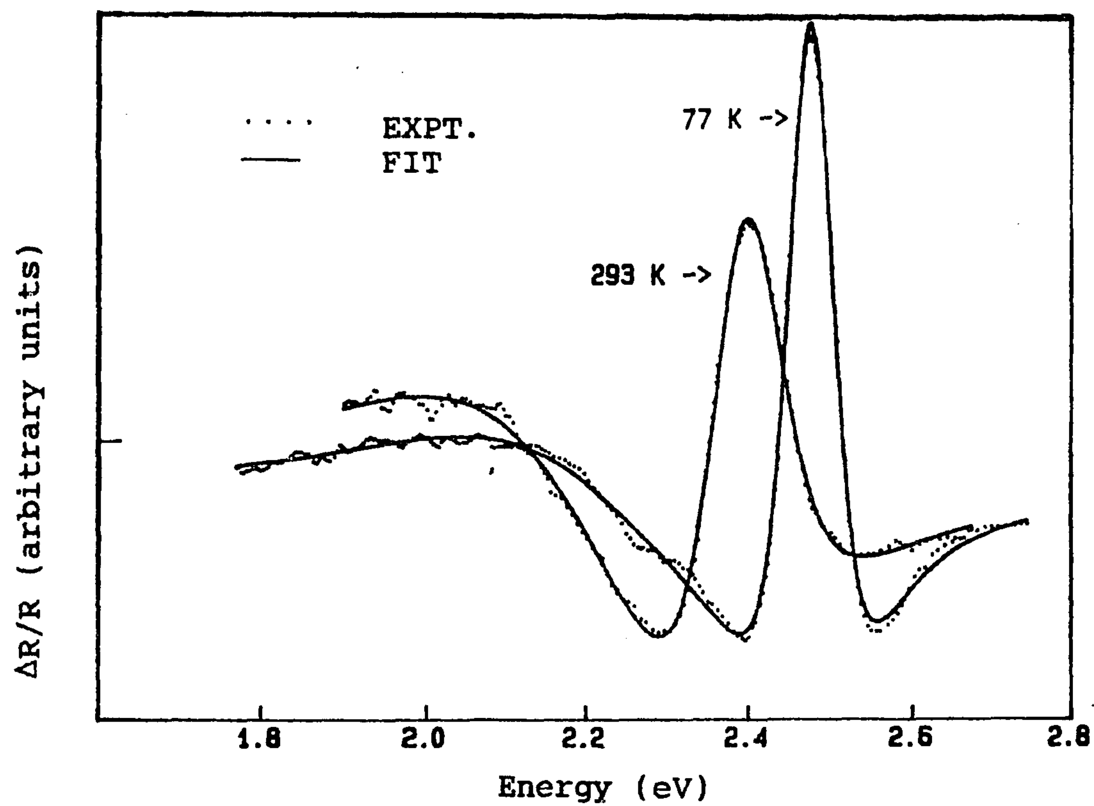

Fig.8

Electroreflectance of $Hg_{1-x}Cd_xTe$ (with x = 0.3) MIS sample (RCS-245-4) at 77 K and 300 K.

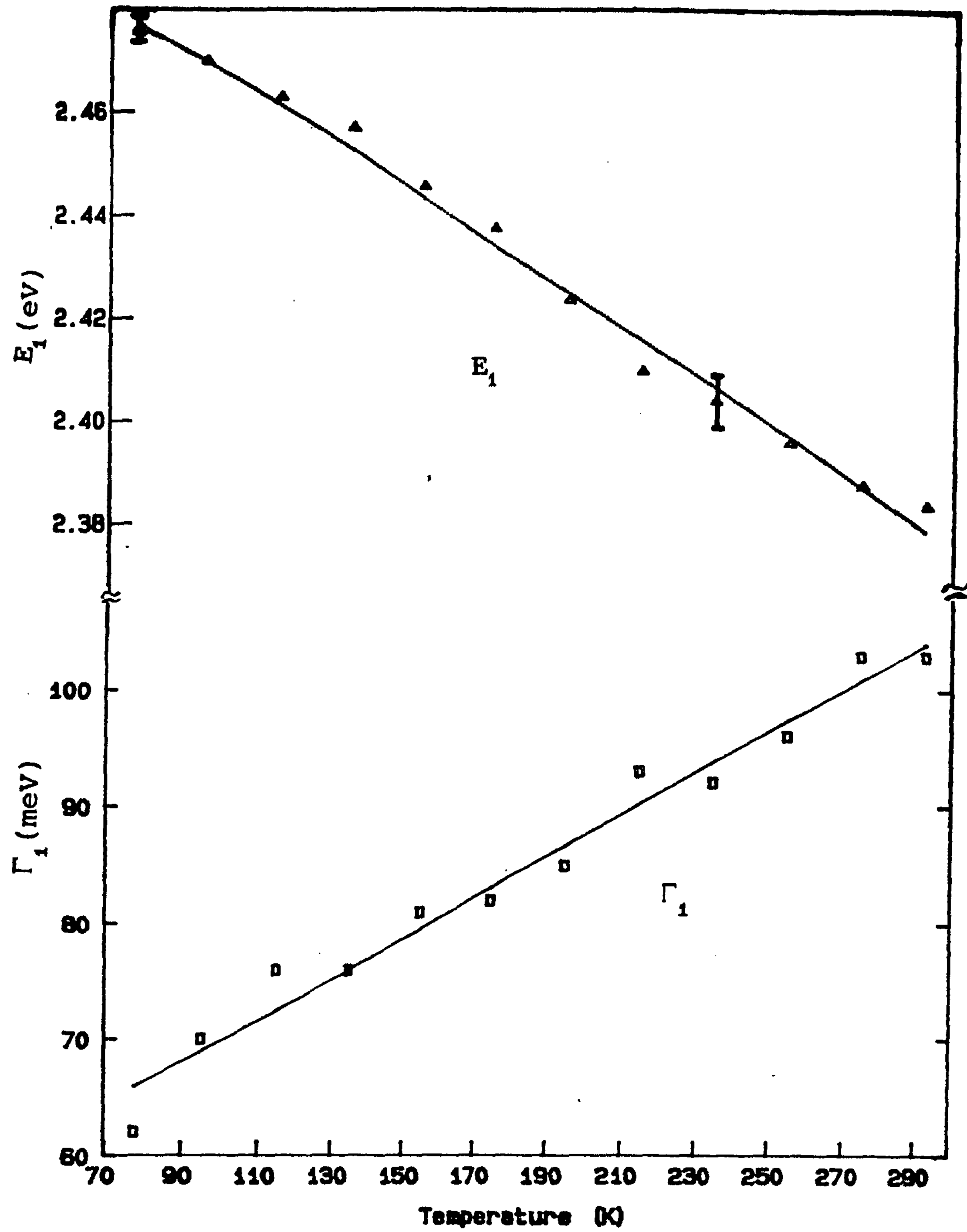

Fig.9

Temperature dependence of the E_1 transition energy and broadening parameter for $Hg_{1-x}Cd_xTe$ ($x \cong 0.3$) MIS sample RCS-245-4.

$$\frac{dE_1}{dT} = -(4.6 \pm 0.3)\cdot 10^{-4}\ \frac{eV}{K} \qquad (35b).$$

The room temperature value of E_1 (2.384 eV) corresponds to the composition $x \cong 0.35$ according to the compositional dependence reported by Viña et al[21]. We found a considerable disagreement between the values reported for the temperature dependence of E_1 energy for the $Hg_{1-x}Cd_xTe$ with approximately the same composition. Berlouis et al[56] measured the dependence using EER in the range 156 - 300 K and obtained $dE_1/dT \cong -5.8\cdot 10^{-4}\ \frac{eV}{K}$ for the x=0.36 sample. Koppel[61] performed reflectivity measurements in the range 8 - 295K and obtained $dE_1/dT \cong -4.35\cdot 10^{-4}\ \frac{eV}{K}$ for the x=0.335 sample. Rodzik and Kisiel's data[57] taken in the range 115 -300 K (also obtained by the reflectivity measuremets) when extrapolated to x=0.35 give $dE_1/dT \cong -3.2\cdot 10^{-4}\ \frac{eV}{K}$.

The value of the broadening parameter $\Gamma \cong$ 62 meV at 77 K is close to the value Γ=66 meV obtained by the photoreflectance method by Amirtharaj et al for a $x \cong 0.3$ sample[62]. The room temperature value of the broadening parameter Γ (103 meV) is larger than the best value reported for $Hg_{1-x}Cd_xTe$[63].

The temperature dependence of Γ should follow the Böse- Einstein statistical function with an average frequency of phonons θ[44]:

$$\Gamma(T) = \Gamma_0[1 + \frac{2}{e^{\theta/k_b T} - 1}] \qquad (36a)$$

where parameter Γ_0 is empirically introduced to account for the broadening at T=0 K. The shape of the experimental curve in Fig.9 suggests roughly linear dependence, however. This is not a total surprise, since the dependence Eq.(36a) becomes quite close to linear at temperatures much higher than θ. Although we do not have a good estimate for the parameter θ, we know that the highest energy of phonons in $Hg_{1-x}Cd_xTe$ is approximately 20 meV. It is conceiveable,therefore, that θ is much smaller than that, thusmaking the temperature dependence of Γ linear in the temperature range of interest. Thus, we fitted the data to the linear relation:

$$\Gamma = \Gamma_L + \gamma T \qquad (36b)$$

which yielded the result:

$$\Gamma_L=52 \pm 2 \text{ meV} \; ; \; \gamma = 0.18 \pm 0.02 \; \frac{\text{meV}}{\text{K}} \qquad (36c).$$

The temperature dependence of the broadening parameter is plotted in Fig.9 (points) along with the fit result (solid line). We could not find data on the temperature dependence of the broadening parameter to compare with our results.

In conclusion we have measured the temperature dependence of the E_1 transition energy and broadening parameter in the range 77 - 293 K using the method of electroreflectance in MIS configuration. Considerable

differences exist between the available results for dE_1/dT which span the interval from $-3.2\cdot10^{-4}$ to $-5.8\cdot10^{-4}\ \frac{eV}{K}$ for the samples with approximately the same composition x. Our result falls close to the middle of this interval. No data was found in the literature on the temperature dependence of the broadening parameter.

3.2.3 Dependence of the Electroreflectance Signal on the Gate Bias.

As mentioned before, the ER technique can be used as a probe of the electric field distribution in the solid as well as the investigation of the electronic band structure. Coupled with the use of a MIS configuration, which makes it possible to control the surface electric field, it becomes a powerful probe of the electronic structure of the insulator- semiconductor interface.

In this section, we report the results of electroreflectance measurements on a MIS sample performed at different gate biases at 77 K. The data yields results concerning the composition of the bulk and the near- surface region of the $Hg_{1-x}Cd_xTe$ substrate.

We have measured the ER spectrum of the ZH-245-3GB sample at 77 K in a spectral region of the

E_1 and $E_1+\Delta_1$ transitions. The spectrum is presented in Fig.10 (points). The modulation amplitude was 1.6 V with no d.c. bias at the frequency 220 Hz. We will show that the spectrum consists of two sets of E_1 and $E_1+\Delta_1$ transitions originating in different parts of the sample. To fit our, data we used GFF lineshapes (Eq.(25)). The solid line in Fig.10 is a least-squares fit of Eq.(25) to the experimental data using p=4, i.e. two sets of E_1 and $E_1+\Delta_1$ transitions denoted E_1^a, $(E_1+\Delta_1)^a$ and E_1^b, $(E_1+\Delta_1)^b$, respectively. Their energies obtained as a result of the fit are indicated by the arrows at the bottom of the figure. In order to demonstrate the necessity of using two sets of transitions we have tried to fit the experimental data using only one set of E_1, $E_1+\Delta_1$ features, i.e. p=2. This fit is shown by the dashed line in Fig.10. It is evident that two sets of features are required to fit the spectrum - particularly the small peak at about 2.3eV (E_1^a) and the region between E_1^b and $(E_1+\Delta_1)^b$.

Since E_1^a and E_1^b are clearly resolved, we shall concentrate on these features. We have studied the d.c. bias dependence of the ER spectra of these two structures. The dotted line in Fig.11 shows the experimental spectra in the region of the E_1^a E_1^b transitions for the bias voltages of -3, -2.5, -2.0, -1.5, -1.0, 0 and +3 V. The solid lines are the least-

squares fit to Eq.(25). In Table III we list the energies, broadening parameters and phases for the E_1^a and E_1^b features at the different bias voltages. Also shown are the relative amplitudes of the third-derivative components of the E_1^a (i.e., $C_a(\hbar\Omega_a)^3$) and E_1^b ($C_b(\hbar\Omega_b)^3$) features, where we have arbitrarily taken $C_b(\hbar\Omega_b)^3 = 1$.

The data in Table III has a number of interesting features. First of all on the basis of the E_1^b transition energy, we can estimate the composition of the $Hg_{1-x}Cd_xTe$ regions responsible for the E_1^a and E_1^b features. Using $dE_1/dT \cong -4.6 \cdot 10^{-4} \frac{eV}{K}$ (our result for the sample # RCS-245-4) we find that room temperature energies of the E_1^a and E_1^b features would be approximately 2.18 and 2.42 eV, respectively. This corresponds[21] to $x_a \cong 0.07$ and $x_b \cong 0.38$.

The broadening parameters for the E_1^a and E_1^b features are $\Gamma_b \cong$ 65 meV and $\Gamma_a \cong$ 90 meV at 77 K. The value of Γ_b is close to that of the RCS-245-4 sample. Assuming that there is about 40 meV broadening of the spectra between 77 K and 293 K (as in case of RCS-245-4 sample), we estimate $\Gamma_b \cong$ 105 meV at the room temperature. For E_1^a feature, we estimate $\Gamma_a \cong$ 130 meV at room temperature which indicates rather poor crystalline quality.

The phases of the ER signal can give information

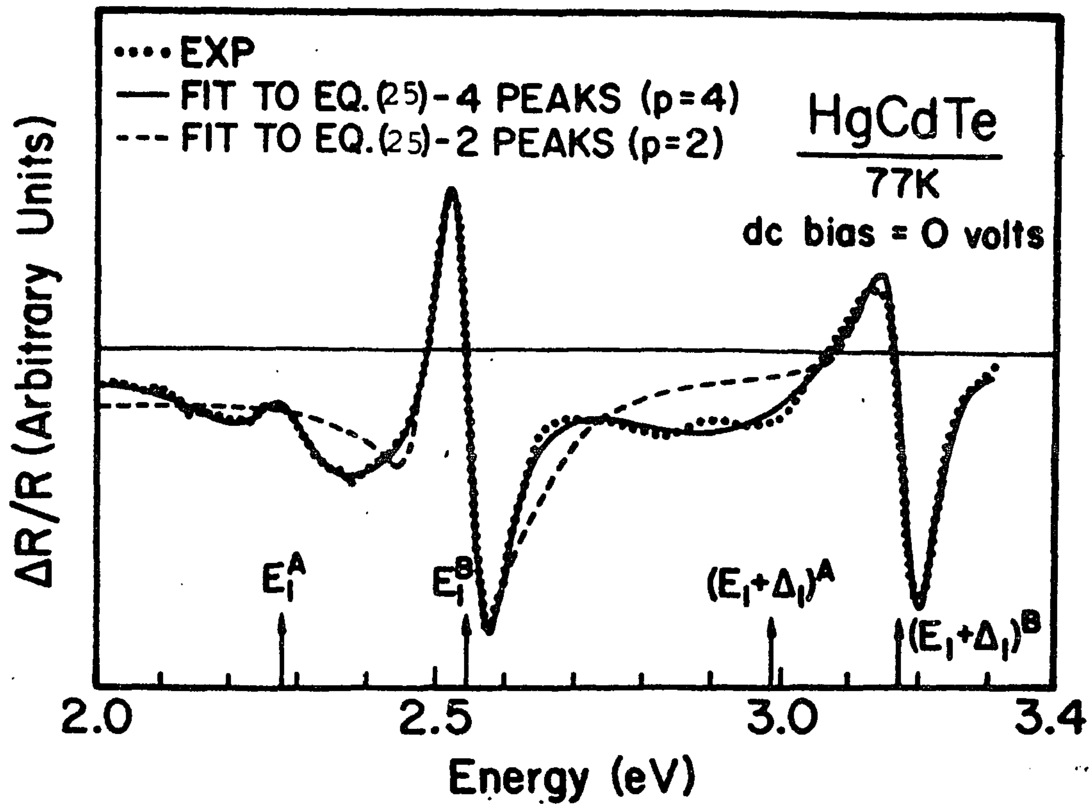

Fig.10

Electroreflectance spectrum of $Hg_{1-x}Cd_xTe$ (with x = 0.3) MIS sample (ZH-245-3GB).

Table III

Energies, broadening parameters and phases obtained for the E_1^a and E_1^b features at various gate biases for MIS sample (ZH-245-3GB).

Gate bias (V)	E_1^a feature			
	E_a^1 (eV)	Γ_a (meV)	Φ_a (deg)	$C_a (\hbar\Omega)^3$
-3	2.26 ± 0.03	99 ± 20	-46 ± 20	0.39 ± 0.2
-2.5	2.31 ± 0.03	87 ± 20	-64 ± 20	0.40 ± 0.2
-2.0	2.30 ± 0.03	86 ± 20	-58 ± 20	0.50 ± 0.2
-1.5	2.29 ± 0.03	94 ± 20	-79 ± 20	1.48 ± 0.2
-1.0	2.30 ± 0.03	96 ± 20	-112 ± 20	1.56 ± 0.2
0.0	2.26 ± 0.03	93 ± 20	-180 ± 30	0.42 ± 0.2
+3.0	2.29 ± 0.03	76 ± 20	-135± 30	0.09 ± 0.2

Gate bias (V)	E_1^b feature			
	E_b^1 (eV)	Γ_b (meV)	Φ_b (deg)	$C_b (\hbar\Omega)^3$
-3	2.52 ± 0.03	61 ± 10	38 ± 5	1
-2.5	2.53 ± 0.03	77 ± 10	53 ± 5	1
-2.0	2.52 ± 0.03	70 ± 10	15 ± 5	1
-1.5	2.55 ± 0.03	67 ± 10	23 ± 5	1
-1.0	2.53 ± 0.03	54 ± 10	-63 ± 5	1
0.0	2.54 ± 0.03	58 ± 10	-75 ± 5	1
+3.0	2.54 ± 0.03	56 ± 10	-100± 5	1

about electric field distributions[36,37]. As discussed above, the amplitude of TDFF (or corresponding term in GFF) is a measure of the modulating electric field in the space- charge region. Also, the inversion of this term indicates the inversion of the carrier type in the in E_1 and $E_1+\Delta_1$ spectral region.space charge region.

Therefore, the phase inversion may be used as an approximate indicator of the flat- band condition. Lastras- Martinez et al[19] have reported the use of this phase inversion to determine the carrier type changes. Note from Table III that between -1.5V and -1.0V of the d.c. bias there is a distinct change of the phase of the B feature. This phase inversion is clearly evident in Fig.11. On either side of the bias range, the phase is fairly constant within the experimental error. This value of the flatband voltage is in good agreement with capacitance- voltage (CV) measurements. Although there are some variations in the phase of the A peak, there is no evidence of phase inversion.

Table III and Fig.11 also show that there is a definite change in amplitude of the two ER features. There is a pronounced increase of A/B ratio for the bias voltages where the B feature goes through the phase flip (i.e. between -1.5 and -1.0 V). Since there is no band bending at this point, the bias dependence of the relative amplitudes yields information about the

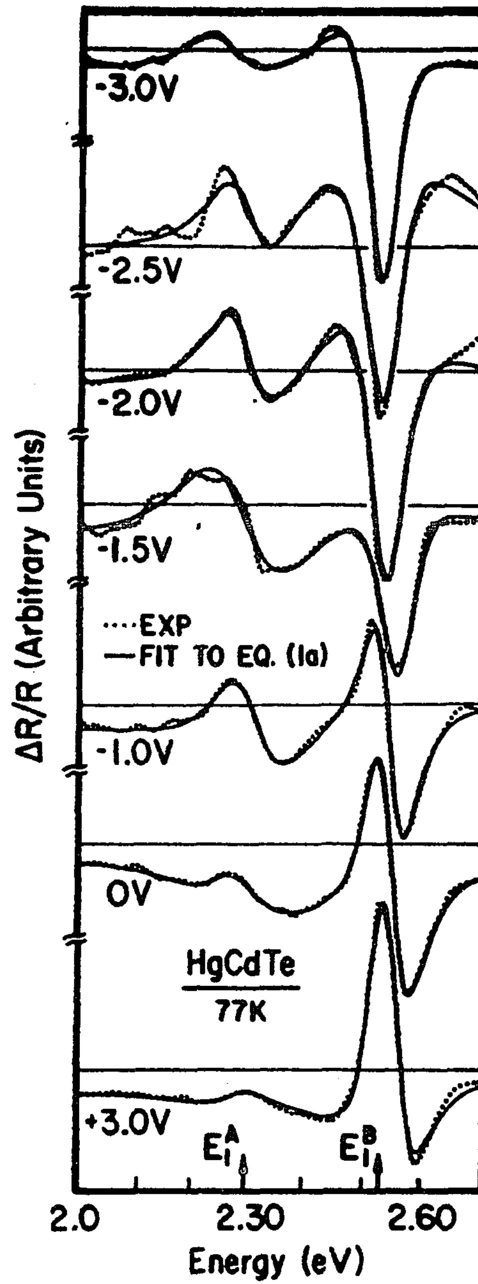

Fig.11

Electroreflectance spectrum of the $Hg_{1-x}Cd_xTe$ (with x = 0.3) MIS sample (ZH-245-3GB) at different gate biases.

relative field distribution of the two regions responsible for the E_1^a and E_1^b features.

The above experimental results clearly indicate that there are two distinct regions in these types of the MIS $Hg_{1-x}Cd_xTe$ samples. There are two ER peaks corresponding to regions of $x \cong 0.07$ and $x \cong 0.38$ with different dependence on the d.c. bias. The $x \cong 0.38$ region goes through the flatband at -1.5 to -1V (at which point the ER signal originated by this region flips phase). Since the other region consists of a semimetal material ($x \cong 0.07$), it is not surprising that the ER signal from this region does not flip phase at this bias.

One of the main questions to be addressed is how the two regions are distributed spatially. Does the composition x vary across the surface or with the depth of the semiconductor? The question can not be answered from ER data alone. However, from the examination of the CV results for high[64] and low[65] frequencies, it is possible to make some comments.

The CV curves[64,65] show no sign of Schottky- type barriers in series with the insulator capacitance. This type of barriers would be expected, if a semimetallic layer were present at the Photox- $SiO_2/Hg_{1-x}Cd_xTe$ interface. In fact the shape of the CV curves is fully accounted for[60,64] by an equivalent circuit which does

not include a Schottky barrier. Therefore, it is unlikely that the low x layer is distributed uniformly over the surface.

There is more evidence that the low- x material is distributed across the surface in islands. Reference 19 reports that a Br_2/methanol etch may leave a cadmium depleted region extending up to 600 Å into the depth of the material. However, the reported variation is only $x \cong 0.02$ over the depth - an order of magnitude smaller than the x variation between the A and B regions. Also, Ref.60 reports a Cd depletion at the $Hg_{1-x}Cd_xTe$ surface due to the exact Br_2 based chemical treatments used to form devices in this study. The variation in effective x value is larger, up to 0.07 (on a base material of $x = 0.3$) but still not as large as seen in our ER results. In Ref.60 the effective value of the surface region was indirectly estimated from the exact surface composition measurements using photoelectron spectroscopy. In the latter case, the surface is sampled over the macroscopic area and the method is only sensitive to the total number of Cd and Hg atoms in the area. Thus, when dealing with the surface of the $x \cong 0.3$ material covered with the semimetallic islands, the method would produce the averaged value of x which is much closer to $x \cong 0.3$ than the actual x in the semimetallic islands.

Thus, since the hypothesis allows the explanation

of the results of Ref.60 without contradicting ours, we assume that the surface of the $Hg_{1-x}Cd_xTe$ material consists of semimetallic islands with the composition x $\cong$ 0.07 spread over the x $\cong$ 0.38 bulk material. There have been no reports of such a two- phase system in the 300 K EER on Br_2/methanol- polished $Hg_{1-x}Cd_xTe$ samples. We have also performed EER on Br_2/methanol- polished $Hg_{1-x}Cd_xTe$ at 300 K and found no evidence of the second lower- energy peak in the E_1 transition region.

We can now give a full explanation as to why the ER spectra of the sample RCS-245-4 were taken at a large negative bias when investigating the temperature dependence of the E_1 transition. As Fig.11 shows, a large negative bias leads to the disappearance of the E_1^a feature. This simplified the fit procedure and allowed for more accurate values of the transition energy and broadening parameter.

We have some additional room temperature data showing that a two- feature structure exists in the E_1 transition range. We have taken a spectrum of a similar sample (# ZH-288) in the E_1 energy region at zero d.c. bias at room temperature. The spectrum is shown in Fig.12. The two- feature structure in the E_1 energy region is apparent. The accuracy of the fit procedure is very low, because the two features are overlapping strongly. Nevertheless, it can be seen from Fig.12, that

the energy separation of the features is approximately 0.25 eV, as in the 77 K spectra. This validates our analysis of the A and B region compositions based on 77 K spectra.

In conclusion we measured ER from $Hg_{1-x}Cd_xTe$ in a MIS configuration as a function of the gate bias voltage. The spectra clearly show the presence of two components corresponding to $x \cong 0.07$ and $x \cong 0.38$ - the latter composition being consistent with the growth conditions, even though somewhat higher. The occurrence of the low- x regions on the $Hg_{1-x}Cd_xTe$ surface appears to be a result of the passivation of the surface by the Photox^{TM} process. There is some evidence indicating that the regions of low- x material are distributed across the surface rather than in depth. The higher- x material is observed to go through the flat- band at the voltage consistent with the CV measurements while the low- x component never passes through the flatband in the bias region used in this study.

3.3 Pump Chopping Frequency Dependence of Photoreflectance in $Hg_{1-x}Cd_xTe$

The mechanism of photoreflectance is based on the reduction of the near-surface electric field by the photo- induced trap charging as illustrated in Fig.5.

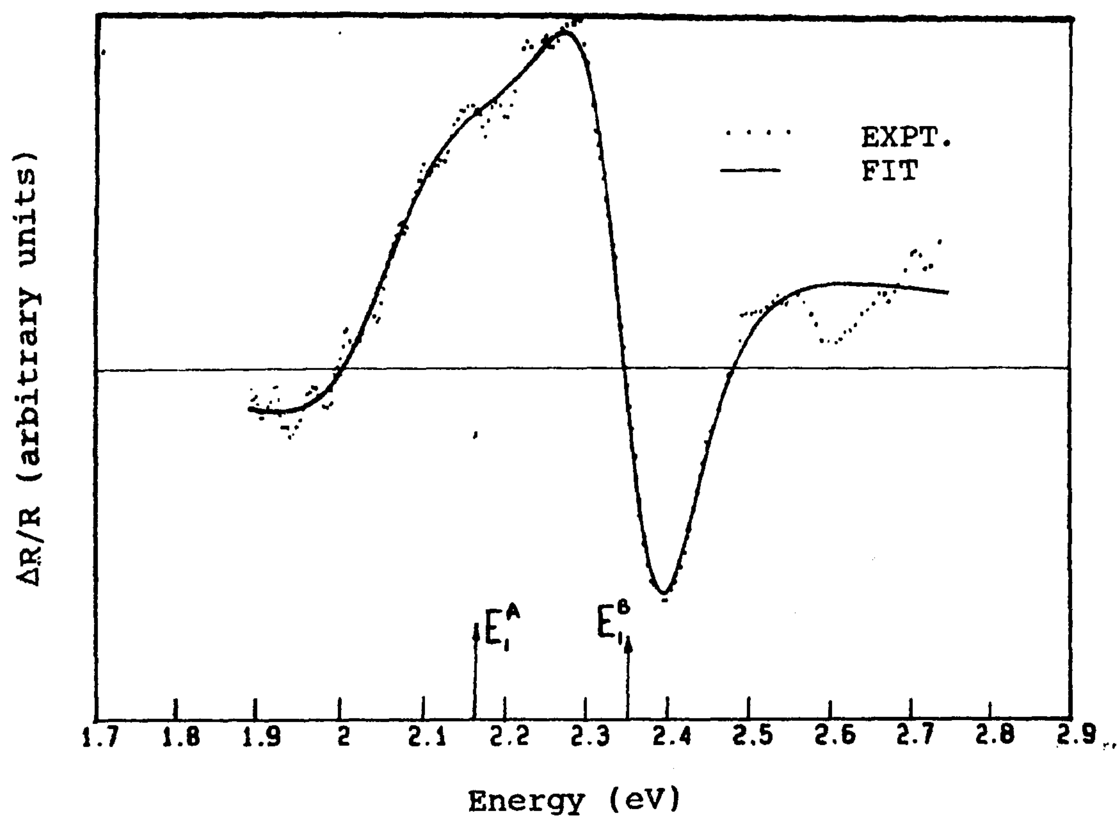

Fig.12

Electroreflectance spectrum of the $Hg_{1-x}Cd_xTe$ MIS (RCS-245-4) sample at room temperature.

The relationship between the characteristic trap lifetimes and the pump beam chopping frequency determines the strength of the PR signal. Therefore, the information on the participating trap lifetimes can be derived from the pump chopping frequency dependence of PR signal.

In this section, we report the results of the PR measurements of $Hg_{1-x}Cd_xTe$ material at different frequencies. The results make it possible to obtain information on the lifetime of the trap states.

Information about the material and/or structure can be obtained from the details of the PR lineshape (energy positions, broadening parameters, etc.), as well as the response to the modulation (pump) perturbation (pump wavelength, modulation frequency[62,66,67], modulation amplitude[68,69], etc.). While considerable attention has been devoted to the lineshape features[33-39], little work has been done in the latter area[62,67]. Recently, the recombination lifetime of electron-hole pairs in GaAs compositional superlattices was obtained from the variation of the PR intensity with frequency (f)[66]. Amirtharaj et al[62] have recently reported the first PR study of $Hg_{1-x}Cd_xTe$ and $Cd_{1-x}Zn_xTe$. For the former material, the 3.39 μm line of a He-Ne laser was employed as the pump excitation with a power density of about 5 mW/cm^2.

We report the results of a PR study at 77 K of $Hg_{1-x}Cd_xTe$ ($0.14 < x < 0.3$) using as pump excitation sources the 4067A line of a Kr+ laser and 4579A line of an Ar+ laser. No PR signal could be obtained for pump wavelengths in the visible region with an energy below the E_1 optical transition. The spectra were studied in the region of the E_1 optical structure. The lineshapes were analyzed by the existing theories of electromodulation by Aspnes[35-37] and Raccah[38,39] yielding interband energies and broadening parameters. In addition, we have investigated the dependence of the PR intensity on pump chopping frequency, f. An analysis of this variation yields a characteristic time which can be related to slow traps[62].

3.3.1 Experimental.

All measurements were made at 77 K in the vicinity of the E_1 critical point of $Hg_{1-x}Cd_xTe$ ($\cong$ 2.3-2.5 eV). Four different samples were studied including bulk, liquid phase epitaxy (LPE) and molecular beam epitaxy (MBE) material. The bulk samples were both n-type ($n \cong 10^{15}$ cm^{-3}, $x=0.3$) and p-type ($p \cong 5x10^{16}$ cm^{-3}, $x=0.3$). The n-type material was achieved by annealing for about 30 days at Hg overpressure. The LPE material consisted of an n-type film ($n \cong 10^{15}$ cm^{-3}) of thickness

10μm having x=0.22 grown on a CdTe (111) substrate. The MBE sample (of thickness 3μm on a CdTe (111) substrate) was also n-type ($n \cong 2.5 \times 10^{16}$ cm^{-3}) but had a nominal Cd concentration of $x \cong 0.14$. The surface of the p-type material was polished by a procedure given in Ref.70. The surfaces of the n-type samples were not processed.

3.3.2 Results

A. LPE $Hg_{0.78}Cd_{0.22}Te$ (n-type)

The PR results using the 4067A pump on this sample are shown in Fig.13 by the dotted curves for f=103 Hz, 600 Hz and 4035 Hz. The spurious background due to the pump leakage has already been subtracted. The lineshapes in Fig.13 are quite similar to the ER lineshapes. The chopping frequency dependence of the PR intensity, i.e. $\frac{\Delta R(f)}{R}/\frac{\Delta R(0)}{R}$ for this case is shown in Fig.14 in the range 40-4000 Hz.

B. MBE-$Hg_{0.86}Cd_{0.14}Te$ (n-type)

Figure 15 displays the experimental PR spectrum (dotted curve) at 77 K in the region of the E_1 optical transition using 4067 A pump wavelength at f=100 Hz. The amplitude of the curve is comparable to that in

Fig.13. Note that the energy of the E_1 optical feature for this sample is lower than that of LPE - $Hg_{0.78}Cd_{0.22}Te$ due to the smaller Cd concentration.

C. Bulk $Hg_{0.7}Cd_{0.3}Te$ (n-type)

The experimental data at 77 K for this sample in the region of the E_1 transition is plotted in Fig.16 (dotted curve) using the 4067 A pump for f=100 Hz. The amplitude of the signal from this sample is somewhat smaller than those in Figs.13 and 15.

D. Bulk $Hg_{0.7}Cd_{0.3}Te$ (p-type)

For this sample the PR spectra at 77 K for f=84 Hz, 641 Hz and 3215 Hz using the 4067 A pump are shown in Fig.17 by the dotted curves. The PR signal at 77 K using the 4579 A line of an Ar laser is displayed in Fig.18. We were not able to get a PR signal from this sample (or any other samples) using green-blue, i.e. Ar laser lines in the range 5145 A-4880 A, even with power densities (≅100 mW/cm^2) comparable to the 4067A or 4579A lines. In Fig.19 we have plotted [R(f)/R]/[R(0)/R] as a function of f for this sample. Note that the frequency variation for this sample is less than that for the LPE material (see Fig.14).

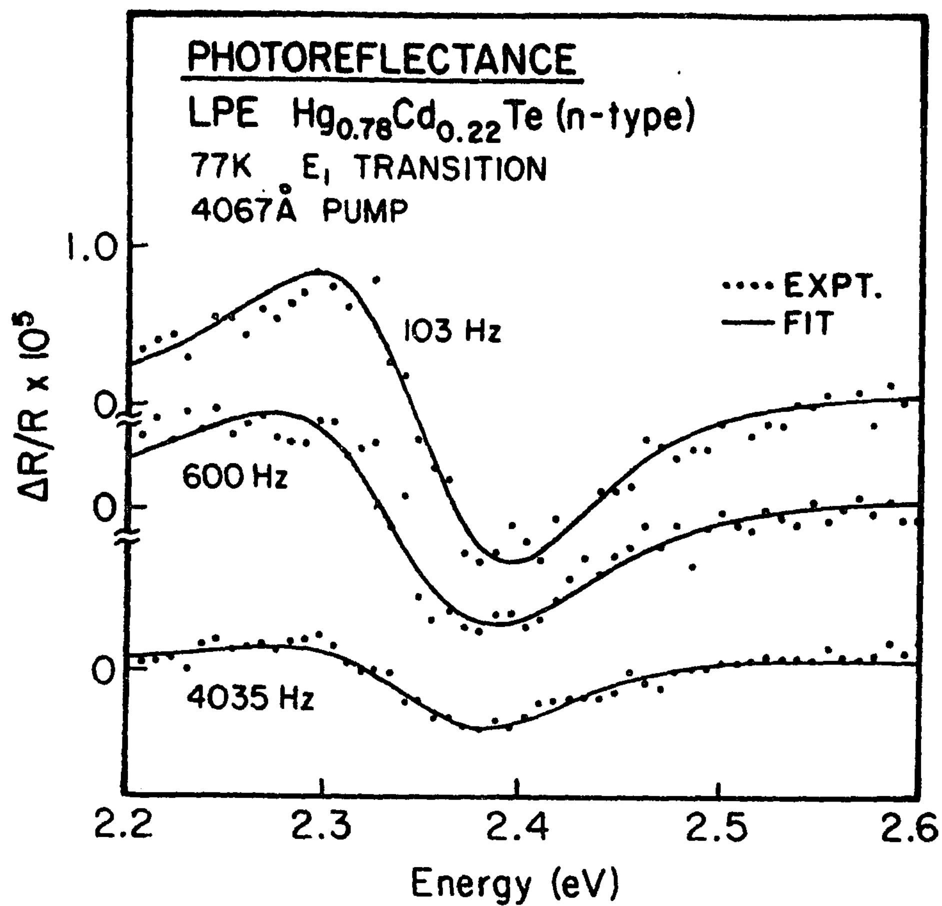

Fig.13

Photoreflectance spectra of the x=0.22 LPE $Hg_{1-x}Cd_xTe$ sample at different chopping frequencies.

3.3.3 Analysis and Discussion

A. Lineshape Analysis

It has been shown that electric-field modulated reflectivity line shape, $\Delta R/R$, in the low-field regime for $Hg_{1-x}Cd_xTe$ can be fit by GDFF given by Eq.(25). For the measurements made with the 4067A pump wavelength there is a spurious background due to stray pump radiation reaching the detector. This background makes it difficult to distinguish between GDFF and TDFF fits to the experimental curves. For all data taken under this condition we have found that both lineshape forms yield comparable results.

The solid lines in Figs.13,15,17 are a least-squares fit of Eq.(25) to the experimental data. The values of E_1 and Γ_1 deduced from the fit are listed in Table IV. We do not report the coefficients for L(E,3/2) and L(E,1/2) since their interpretation is not clear due to the spurious background mentioned above.

The LPE- $Hg_{0.78}Cd_{0.22}Te$ material has also been measured using the 3.39 μm pump[20]. For this sample the values of Γ_1 are about 10% different for the 3.39 μm and 4067A pump wavelength measurements. This may be due to sample inhomogenety since no care was exercised

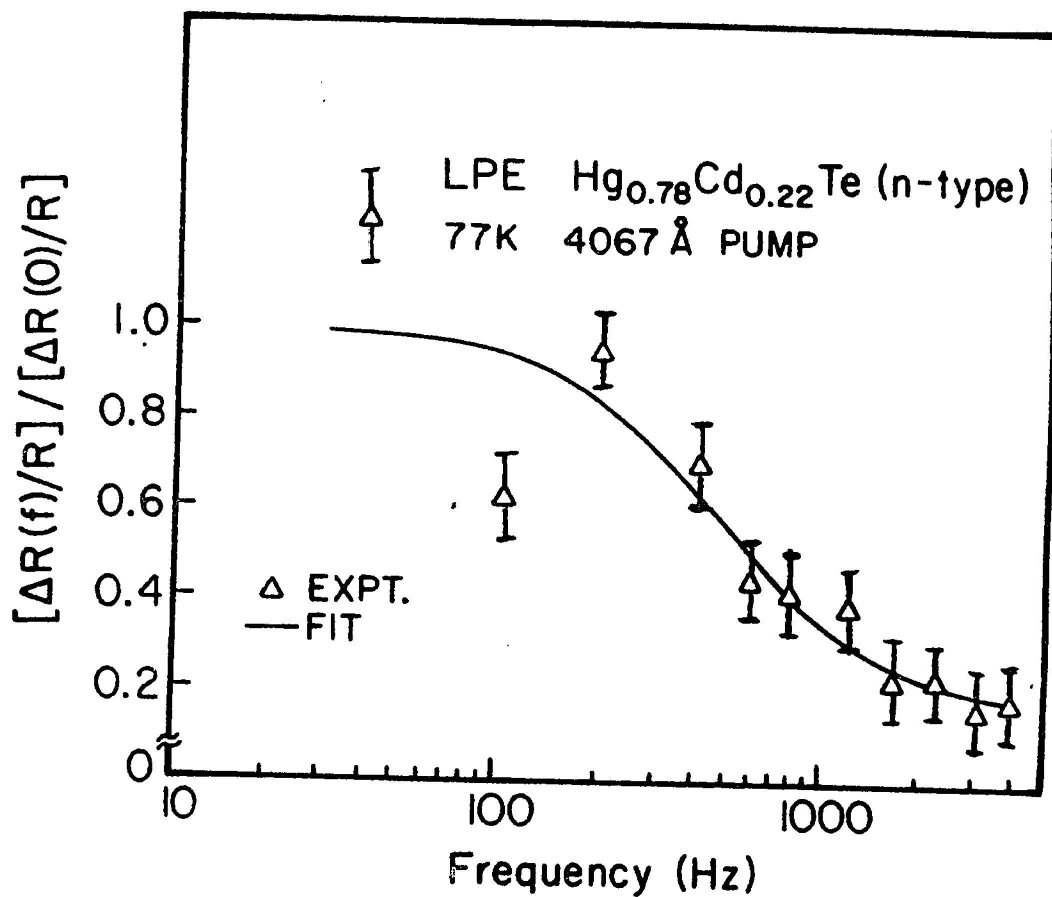

Fig.14

Frequency dependence of the PR intensity for the $x=0.22$ LPE $Hg_{1-x}Cd_xTe$ sample

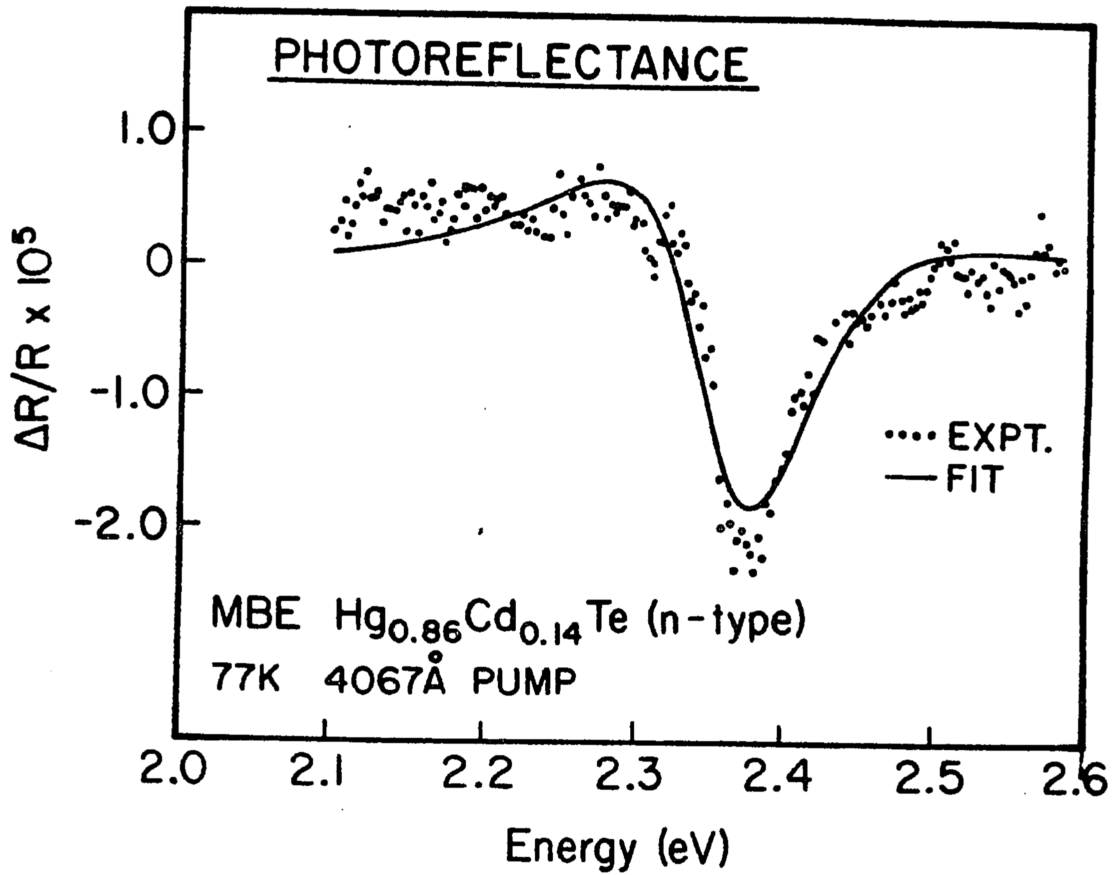

Fig.15

Photoreflectance spectrum of the x=0.14 MBE (n-type) $Hg_{1-x}Cd_xTe$ sample

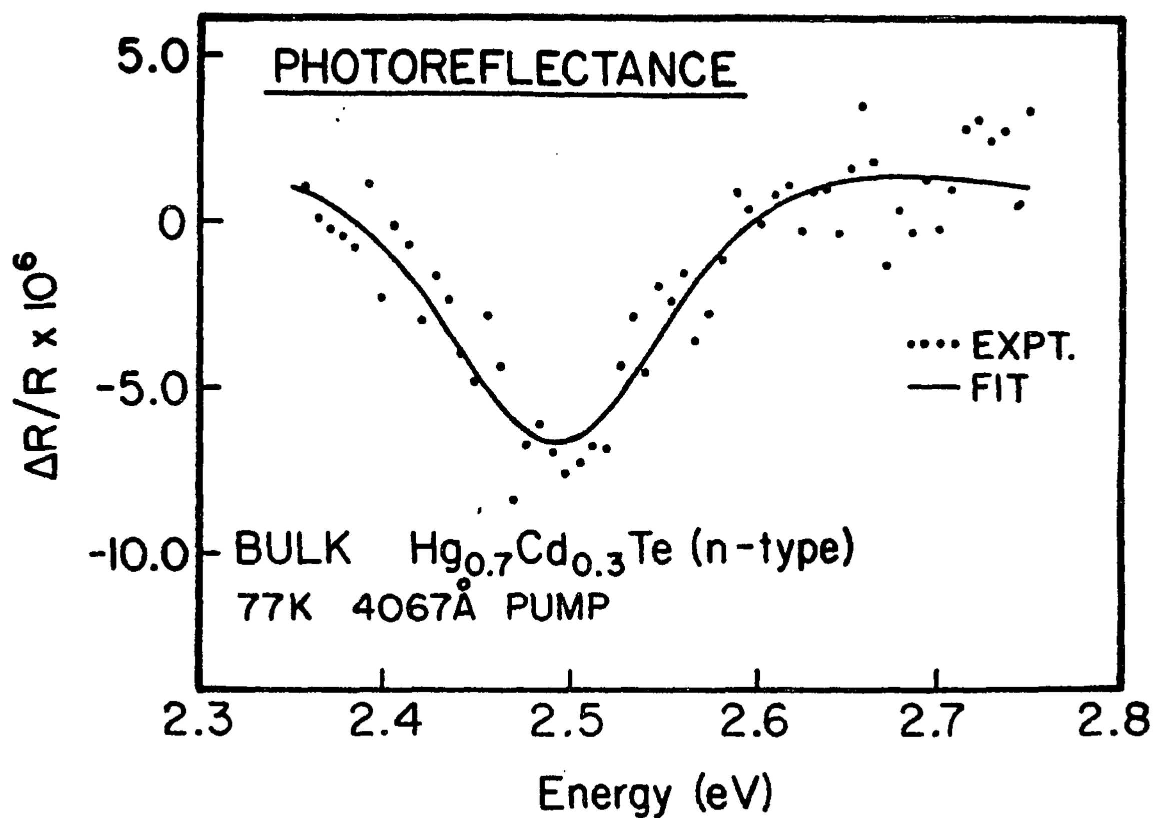

Fig.16

Photoreflectance spectrum of the x=0.3 bulk (n-type) $Hg_{1-x}Cd_xTe$ sample

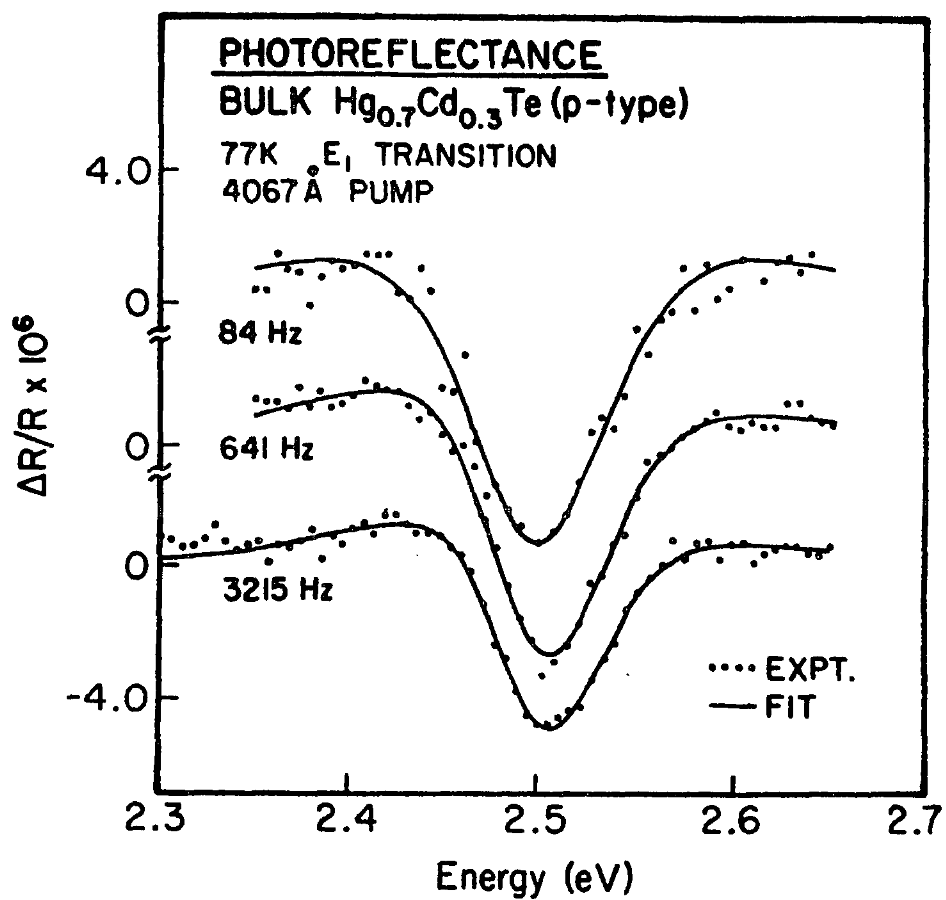

Fig.17

Photoreflectance spectra of the x=0.3 bulk (p-type) $Hg_{1-x}Cd_xTe$ sample taken with 4067 Å pump.

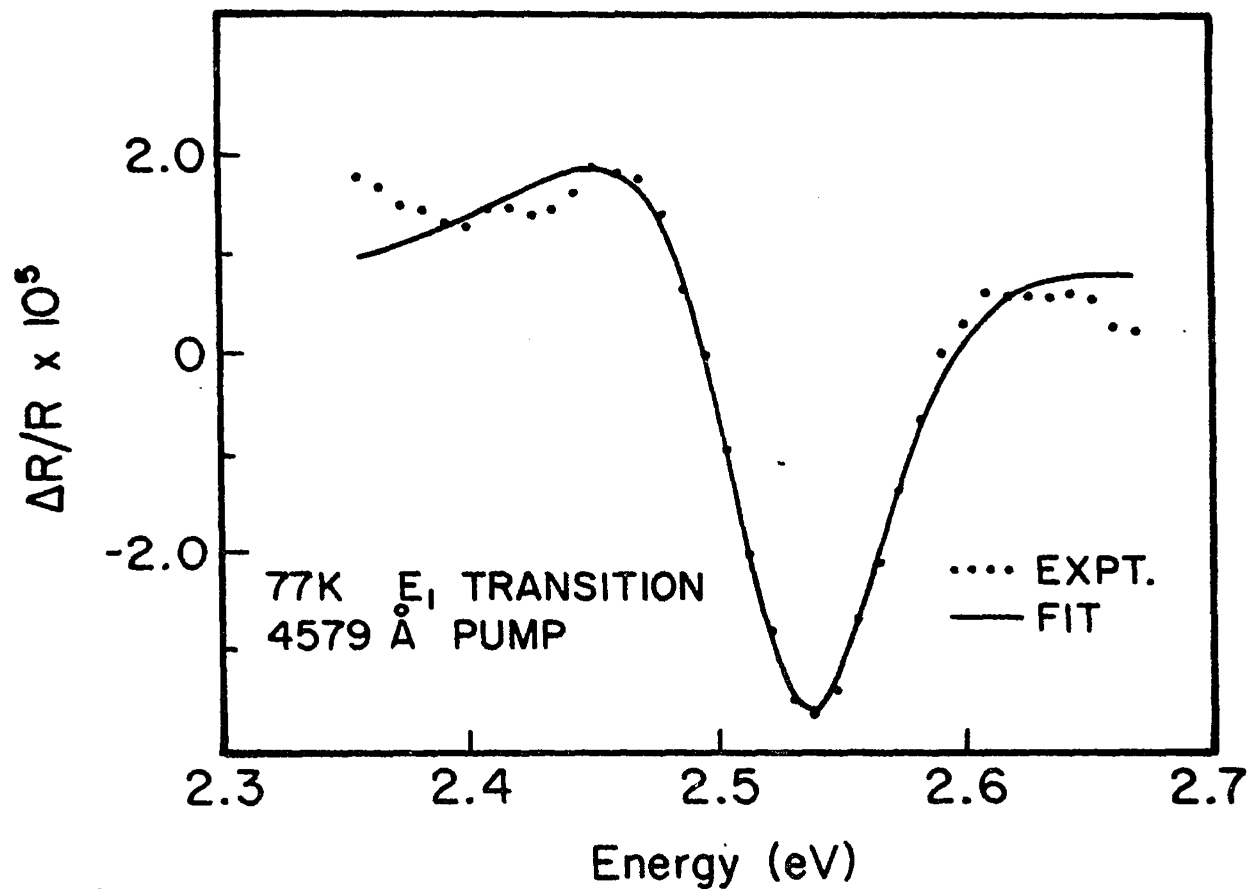

Fig.18

Photoreflectance spectra of the x=0.3 bulk (p-type) $Hg_{1-x}Cd_xTe$ sample taken with 4579 Å pump.

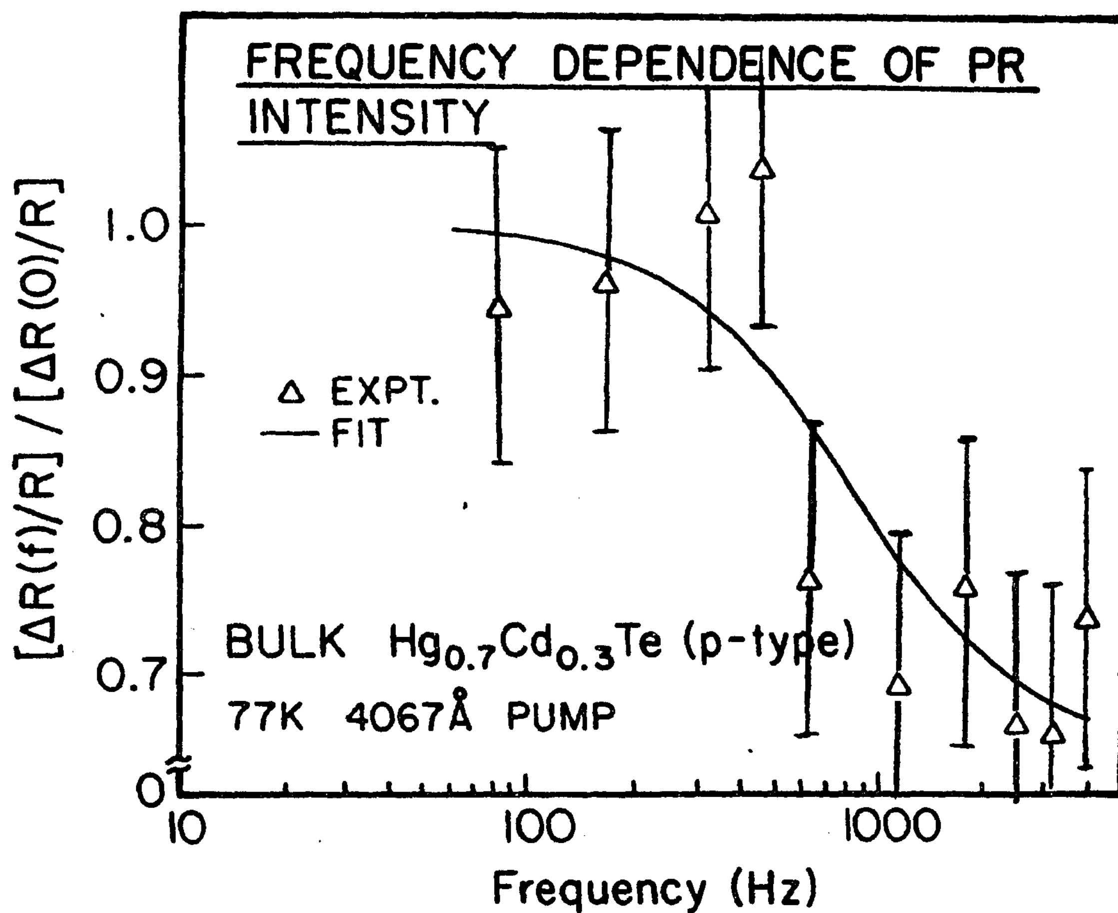

Fig.19

Frequency dependence of the PR intensity for the x=0.3 bulk (p-type) $Hg_{1-x}Cd_xTe$ sample.

to insure that both measurements were taken on the same spot on the sample. The energy of E_1 is consistent with composition $x \cong 0.22$.

The MBE-$Hg_{0.86}Cd_{0.14}Te$ sample has E_1 consistent with $x \cong 0.14$ and a broadening parameter comparable to the LPE sample. Both bulk- $Hg_{0.7}Cd_{0.3}Te$ samples (n-type and p-type) had essentially the same value of E_1. The PR results of Amirtharaj et al at 77 K on LPE-$Hg_{0.7}Cd_{0.3}Te$ has yielded a similar value for E_1[62]. The quality of the n-type sample does not appear to be very good since it has Γ_1 = 146 meV. Of all the samples studied the bulk p-type sample appears to be the best with Γ_1 = 79 meV. However, even this value is not as good as the one obtained previously at 77 K by PR[62] or ER measurements reported in this work.

B. Pump Frequency Dependence of the PR Intensity

The dependence of the PR intensity as a function of the chopping frequency was studied with a view toward obtaining information about the dynamics of the surface electric fields. This variation can be accounted for on the basis of the following considerations. The chopped pump radiation can be considered as a square wave source. When light impinges on the sample, electron-hole pairs are created. These charges are then free to fill

the charge traps and modify the surface electric field strength, somewhat similar to the behavior of a capacitor. We assume that these excess carriers abruptly change the built- in electric field. When the light is switched off the trap population and the electric field strength decays with a characteristic time τ, causing a restoration of the original surface potential. Thus for chopping frequency f it can be shown that the Fourier component of the PR intensity, $\Delta R(f)/R$, can be written as[66]:

$$\frac{\Delta R(f)/R}{\Delta R(0)/R} = \sum_{i=1}^{m} \left[\frac{4 + f^2\tau_i^2[1 - \exp(-\pi/f\tau_i)]^2}{4(1 + f^2\tau_i^2)} \right]^{1/2} \quad (37)$$

where τ_i is the characteristic constant of the i- th trap state.

As an approximate means to extract the effective average time constant τ from the observed modulation frequency dependence of the PR intensity we have used a modified version of Eq.(37). We assumed that only two kinds of interface states were present: one kind with characteristic time τ within the frequency range of our experiment and the other with characteristic time $\tau' \ll \tau$. Then we can write:

$$\frac{\Delta R(f)/R}{\Delta R(0)/R} = \left[\frac{4 + f^2\tau^2[1 - \exp(-\pi/f\tau)]^2}{4(1 + f^2\tau^2)} \right]^{1/2} + A \quad (38)$$

The term A in Eq.(38) represents the contribution from

Table IV

Values of the energy gap (E_1) and broadening parameter (Γ_1) for the E_1 transition at 77 K for several $Hg_{1-x}Cd_xTe$ samples.

Sample	E_1 (eV)	Γ_1 (meV)
LPE $Hg_{0.78}Cd_{0.22}Te$ (n-type)	2.43[a] 2.40[b]	96[a] 110[b]
MBE $Hg_{0.86}Cd_{0.14}Te$ (n-type)	2.36[b]	94[b]
Bulk $Hg_{0.7}Cd_{0.3}Te$ (n-type)	2.49[b]	146[b]
Bulk $Hg_{0.7}Cd_{0.3}Te$ (p-type)	2.50[b]	79[b]
	2.51[c]	78[c]

a) 3.39μm pump measurement form Ref.20

b) 4067 Å pump measurement

c) 4579 Å pump measurement

all the states with $1/\tau' >> 1000$ Hz, i.e., very fast states in relation to our frequency range.

The solid lines in Figs.14 and 19 represent a least-squares fit of Eq.(38) to the experimental data points. The low quality of fit in Fig. 19 is probably a result of using a simplistic model. The obtained values of τ, however, must give a close estimate of the trap lifetimes. These values are listed in Table V along with the τ obtained from the PR experiments using 3.39 μm pump[20]. All three measurements yield time constants on the order of milliseconds. This is consistent with the large number ($\cong 10^{13}$ cm^{-2}) of slow traps with $\tau > 1$ millisecond observed at the $Hg_{1-x}Cd_xTe$ /oxide interface using CV techniques[71]. It should be noted, however, that the LPE $Hg_{0.78}Cd_{0.22}Te$ data presented in Ref.61 contains a large constant background which indicates the presence of a significant number of "fast" traps in addition to the $\tau = 4.4$ msec slow traps. The frequency response of the PR intensity from the same sample recorded using the 4067A pump wavelength indicated a dominant trap level with $\tau = 2.8$ msec (see Fig.14). The apparent differences observed with these two pump wavelengths may be an indication of the variation in the details of the charging and discharging of the traps within the region penetrated by the two pump beams. For instance, traps within about 100A of the

Table V

Values of the time constant τ at 77 K for several $Hg_{1-x}Cd_xTe$ samples.

Sample	τ (10^{-9}s)
LPE $Hg_{0.78}Cd_{0.22}Te$ (n-type)	4.4 ± 1[a] 2.8 ± 0.5[b]
Bulk $Hg_{0.7}Cd_{0.3}Te$ (p-type)	1.7 ± 0.3[b]

a) 3.38 μm pump measurement (from Ref.20)

b) 4067 Å pump measurement

surface and in the native oxide layer will play a more important role in the case of the 4067A pump due to its short penetration depth (≅200A).

In summary, we have measured the excitation wavelength and pump chopping frequency dependence of PR in several $Hg_{1-x}Cd_xTe$ samples at 77 K deep using blue-violet (4579-4067A) pump radiation. Signals have been observed from both n- and p-type material as well as samples fabricated under different conditions - i.e., bulk, LPE and MBE. Both as-grown and polished surfaces produced PR spectra. The spectral lineshapes were fit using existing theories of electromodulation and yielded important information regarding properties of the material such as the interband energies and broadening parameters of the E_1 transition. We have demonstrated that the dependence of the PR intensity on the modulation frequency can be used as a contactless technique to evaluate slow surface (interface) traps which exist in this material. The use of pump wavelengths with different penetration depths may be useful for obtaining some information about the depth distribution of these traps.

3.4 Temperature Dependence of Photoreflectance of Bulk CdTe

In this section we report the PR study of a bulk undoped high- resistivity CdTe sample in the 77- 297 K temperature range. The sample had a number of impurities detected by the secondary ion mass spectroscopy, none of them with a concentration higher than 10^{16} cm^{-3}.

The spectra were taken in spectral regions of E_0 and E_1 gaps. It seems that, although the concentration of residual impurities was less than 10^{16} cm^{-1}, the E_0 optical spectra of the sample at temperatures higher than 202 K were dominated by the transition related to the presence of donor levels. The obtained impurity binding energy was found to be in good agreement with the available data. The temperature dependence of the E_0 and E_1 transition energies and broadening parameters were also obtained and discussed.

3.4.1 Sample Preparation.

In this study we used a sample of CdTe furnished by Santa Barbara Research Center. The sample was cut along the (100) surface. It was polished mechanically using first 1μm and then 0.05μm grit alumina powder. During the first polishing cycle we removed 500μm layer of the material, during the second one- 100μm layer. The mechanical polishing was followed by the chemomechanical polishing by 0.05% Br solution in methanol. The duration

of the chemomechanical polishing was 4 min. In all polishing procedures we used the Politex supreme polishing pads (Rodel, Inc.).

3.4.2. Experimental Results

The PR spectra were taken at eleven different temperatures between 77 K and 300 K. We used a He-Ne laser with 1.5 mW as a pumping source ; the pumping beam produced a spot with diameter ≅ 2mm on the sample. The chopping frequency was approximately 200 Hz. To eliminate the spurious background signal resulting from the pump beam leakage, we used a long-pass filter with cut- on wavelength 7000 Å for the E_0 spectral region. For the E_1 spectral region we used the band- pass filter with the transparency band centered at 3700Å.

A. E_1 Transition

The experimental PR spectra of the E_1 transition are shown in Fig.20 (dots). The spectra have been fit to the TDFF lineshape for the 2D CP[57]. The E_1 transition energies and broadening parameters (Γ_1) obtained as a result of the fit procedure are presented in Table VI. The temperature dependence of the transition energy and the broadening parameter are plotted in Fig.21. The

temperature dependence of the transition energy has been fit to the Varshni relation. The fit resulted in the following parameters:

$$E_1(0) = 3.55 \pm .03 \text{ eV}$$
$$\alpha = -(8.3 \pm 0.4)\cdot 10^{-4} \frac{\text{eV}}{\text{K}} \qquad (39)$$
$$\beta = 140 \pm 60 \text{ K}$$

The solid line in Fig.21 represents this fit result. The temperature dependence of Γ_1 was fit to the linear relation[44]:

$$\Gamma = (58 \pm 3) \pm (7 \pm 1)\cdot 10^{-2} T \text{ meV} \qquad (40)$$

B. E_0 Transition

The sequence of the PR spectra in the E_0 region is presented in Fig.22. This figure contains a surprising feature.

Spectra for the temperatures between 77 and 182 K contain a single peak (which we will call an "A" feature) which can be fit by a TD lineshape for a 3D CP. An example of such fit is shown in Fig.23.

The spectrum taken at 202 K apparently contains two features. We fit this spectrum with two TD lineshapes assuming both CP's to be 3- dimensional as shown in Fig.23. We shall denote the additional (lower-energy) feature as "B" feature. At higher temperatures only the "B" feature is present in the PR spectra. The

energies and broadening parameters obtained as a result of the fit are shown in Table VI. We also plot the E_1 transition energy and it's broadening parameter vs. temperature (as obtained from the fit) in Fig.24.

We have also attempted to fit the "B" feature by the first- derivative lineshape. The χ^2 turned out to be somewhat larger than in the TD fit, but the difference was not large enough to draw any conclusions about the actual nature of the feature.

3.4.3 Analysis and Discussion

We shall first bring our attention to the E_0 spectra.

The presence of the two features which dominate the spectrum in the E_0 region alternately at different temperatures have been observed previously by Camassel et al[10] in the piezoreflectance spectra of CdTe. Following their assumption, we can ascribe the appearance of the "B" feature to the presence of the donor level(s) in CdTe. The donor levels may be caused by the presence of defects or impurities in the material. It is known that a number of impurities are unintentionally introduced in CdTe crystals during growth[72,73]. The resulting impurity levels have been observed by modulation spectroscopies[10,74]. The presence

of the B impurity in CdTe has been recently observed by Amirtharaj et al[74] using the PR method.

Thus we may interpret the "A" peak as arising from the valence band- to- conduction band and the "B" peak as arising from the valence band- to -donor transition. The donor level binding energy is equal to the difference in energy of the "A" and "B" features which at 202 K equals to ≅ 14 meV as seen from Table VI. This value is in agreement with the currently available data. It has been reported that the binding energy of the shallow donor levels computed from the hydrogenic model and corrected for the presence of other impurity atoms equals to ≅ 14 meV.[7,8] Recent optical measurements[72] revealed six different donors in CdTe with binding energies lying between 13.5 and 15 meV.

The value of the binding energy reported by Camassel et al[10] is more than 20 meV at 77 K, but this is a minor discrepancy since this group did not use any lineshape fit to obtain the transition energies.

There is a detail in the behavior of the spectrum that is not explained by this approach. To explain the appearance of the "B" feature we have to assume that, at approximately 200 K, the donor level(s) get ionized and therefore a large number of free states becomes available for transitions leading to appearance of the "B" feature. But what is responsible for the

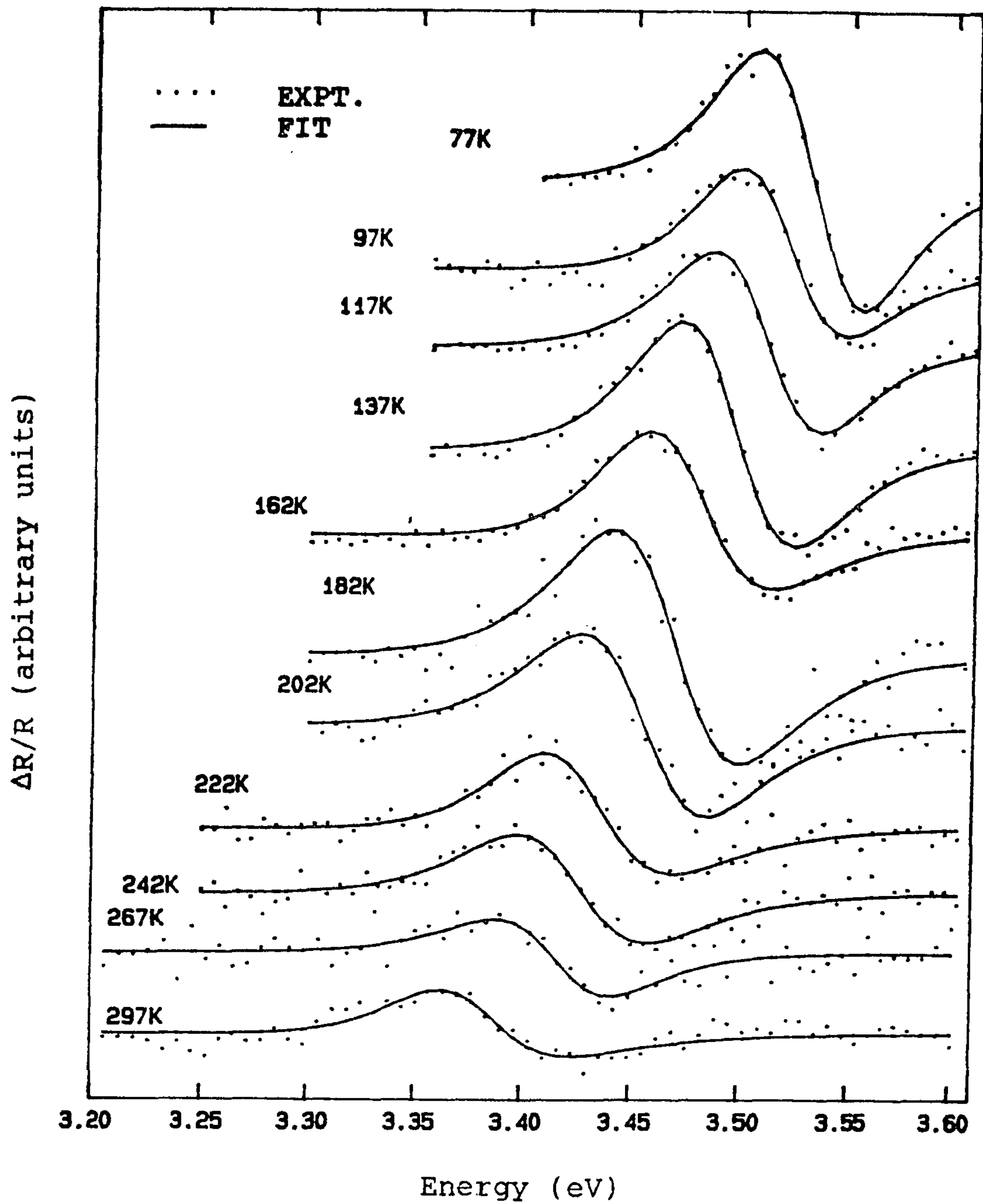

Fig.20

Photoreflectance spectra of the CdTe sample in E_1 spectral region at different temperatures.

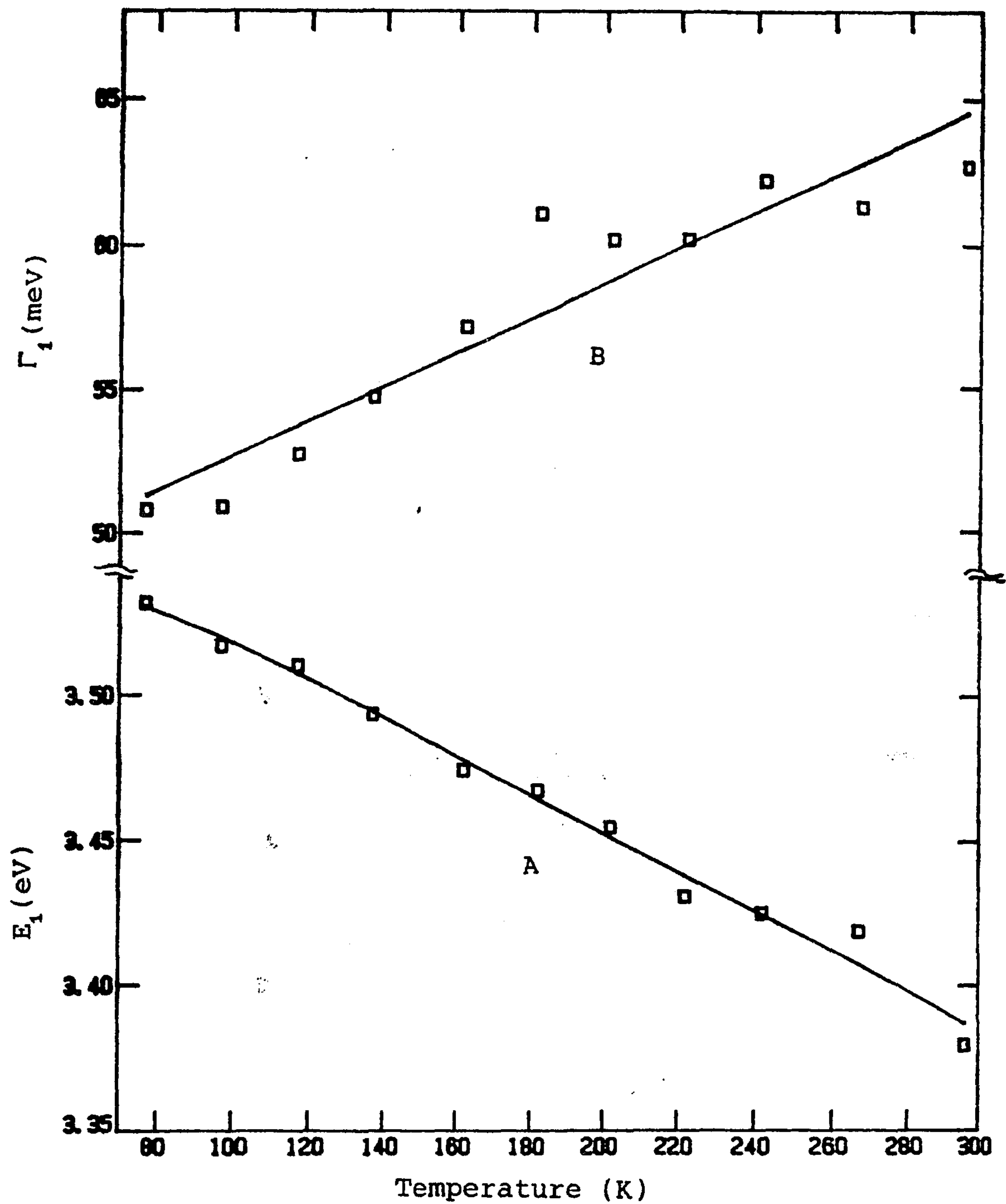

Fig.21

Temperature dependence of E_1 transition energy and broadening parameter for CdTe.
A- transition energy
B- Γ_1 (broadening parameter)

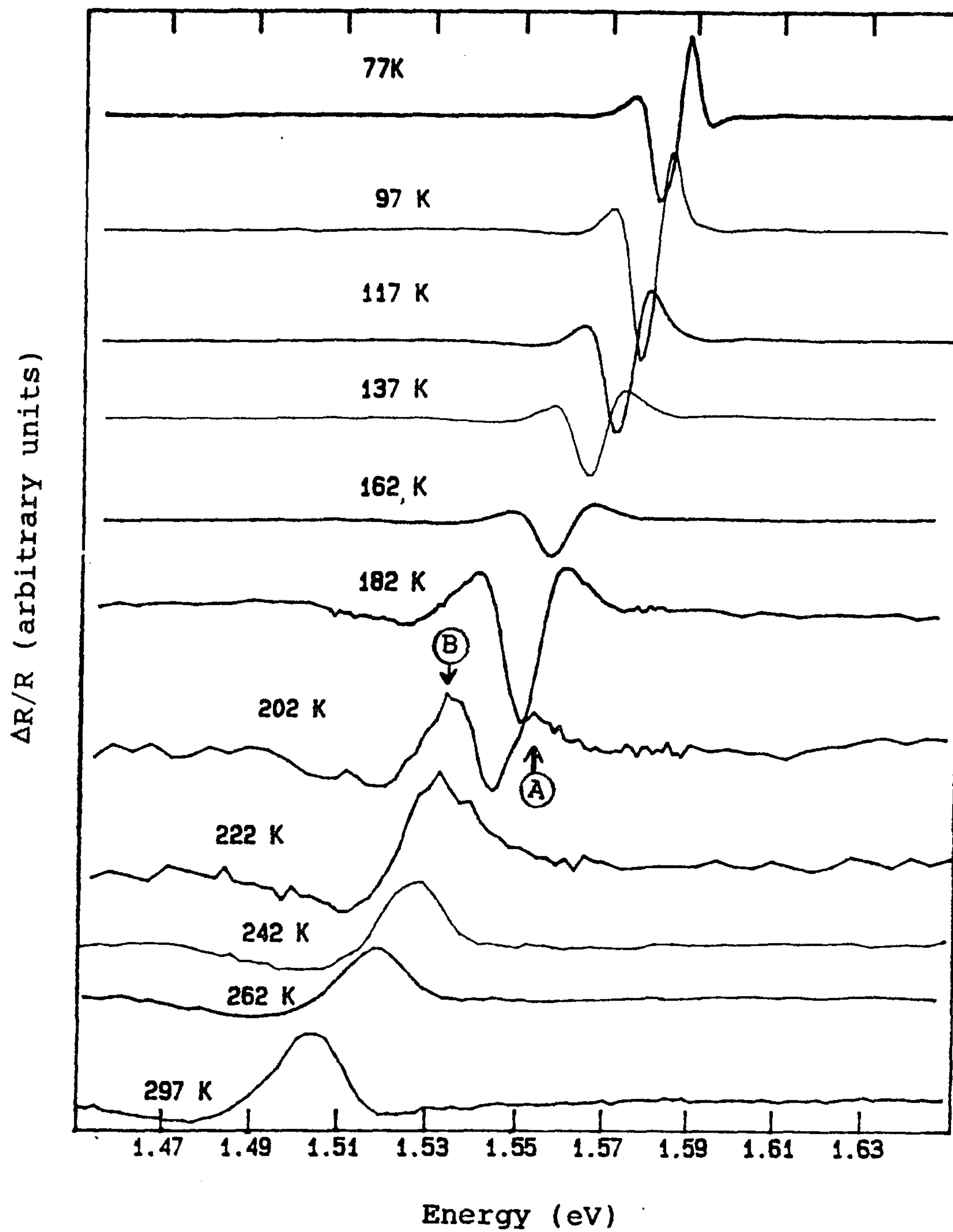

Fig.22

Photoreflectance spectra of the CdTe sample in E_0 spectral region at different temperatures.

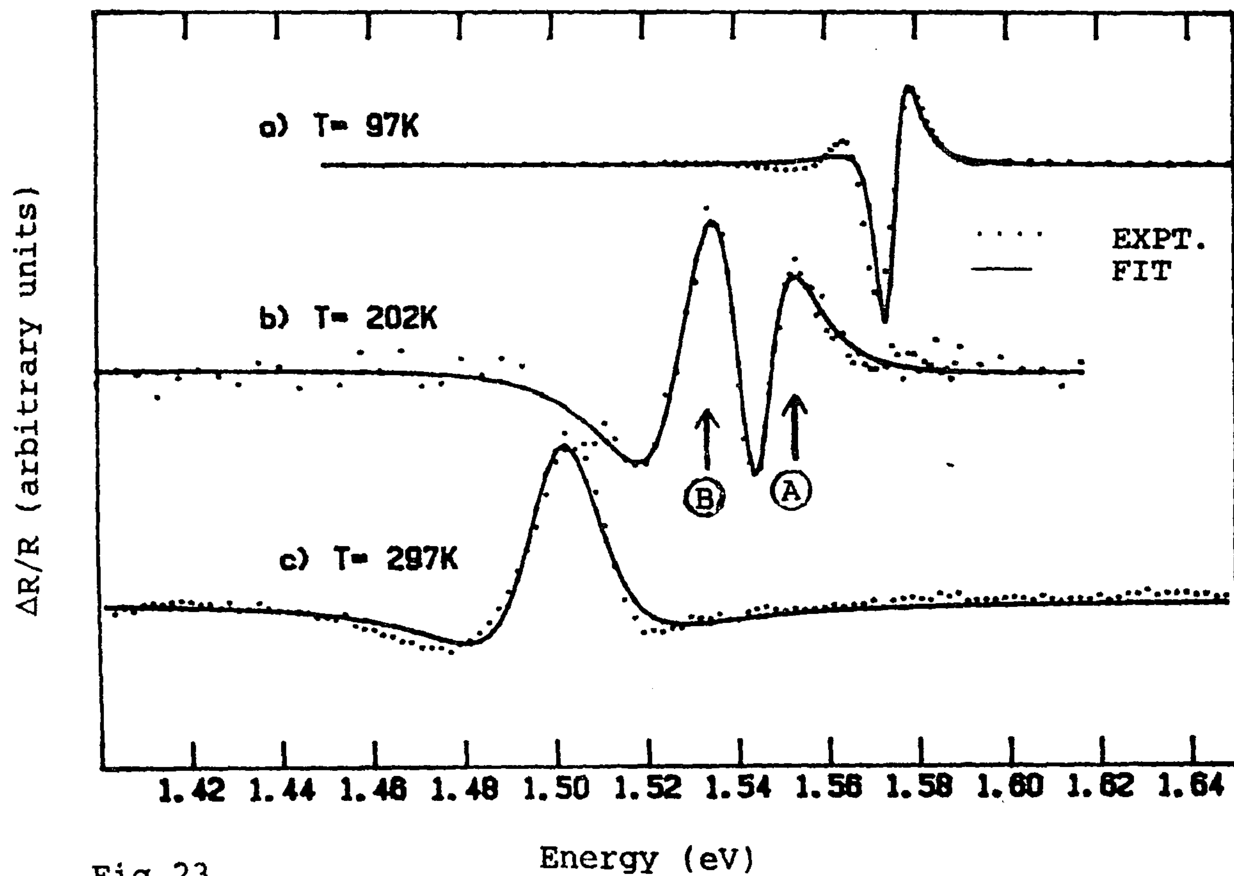

Fig.23

Examples of lineshape fit of the CdTe spectra in E_0 spectral region.
97K and 297K spectra are fit with one transition and 202K with two transitions. TD lineshape for 3D CP was used in all cases.

Table VI

Energies and broadening parameters E_0 for the and E_1 transitions of CdTe at various temperatures.

T (K)	E_0 (eV)	Γ_0 (meV)	E_1 (eV)	Γ_1 (meV)
77	1.584±.003[a]	5.2 ± 0.3[a]	3.511±.005	61±3
97	1.581±.003[a]	4.7 ± 0.4[a]	3.53 ±.01	63±3
117	1.575±.003[a]	5.2 ± 0.4[a]	3.52 ±.01	63±4
137	1.568±.004[a]	6.2 ± 0.4[a]	3.51 ±.01	65±4
162	1.552±.004[a]	7.7 ± 0.4[a]	3.50 ±.01	68±5
182	1.551±.004[a]	7.5 ± 0.4[a]	3.48 ±.01	71±5
202	1.545±.009[a]	9.5 ± 0.7[a]	3.47 ±.01	76±5
	1.531±.008[b]	19 ± 2[b]		
222	1.527±.008[b]	21 ± 2[b]	3.46 ±.01	75±6
242	1.522±.008[b]	19 ± 2[b]	3.43 ±.02	74±6
262	1.514±.008[b]	20 ± 2[b]	3.42 ±.02	77±6
297	1.501±.008[b]	19 ± 2[b]	3.38 ±.03	76±8

a) "A" feature

b) "B" feature

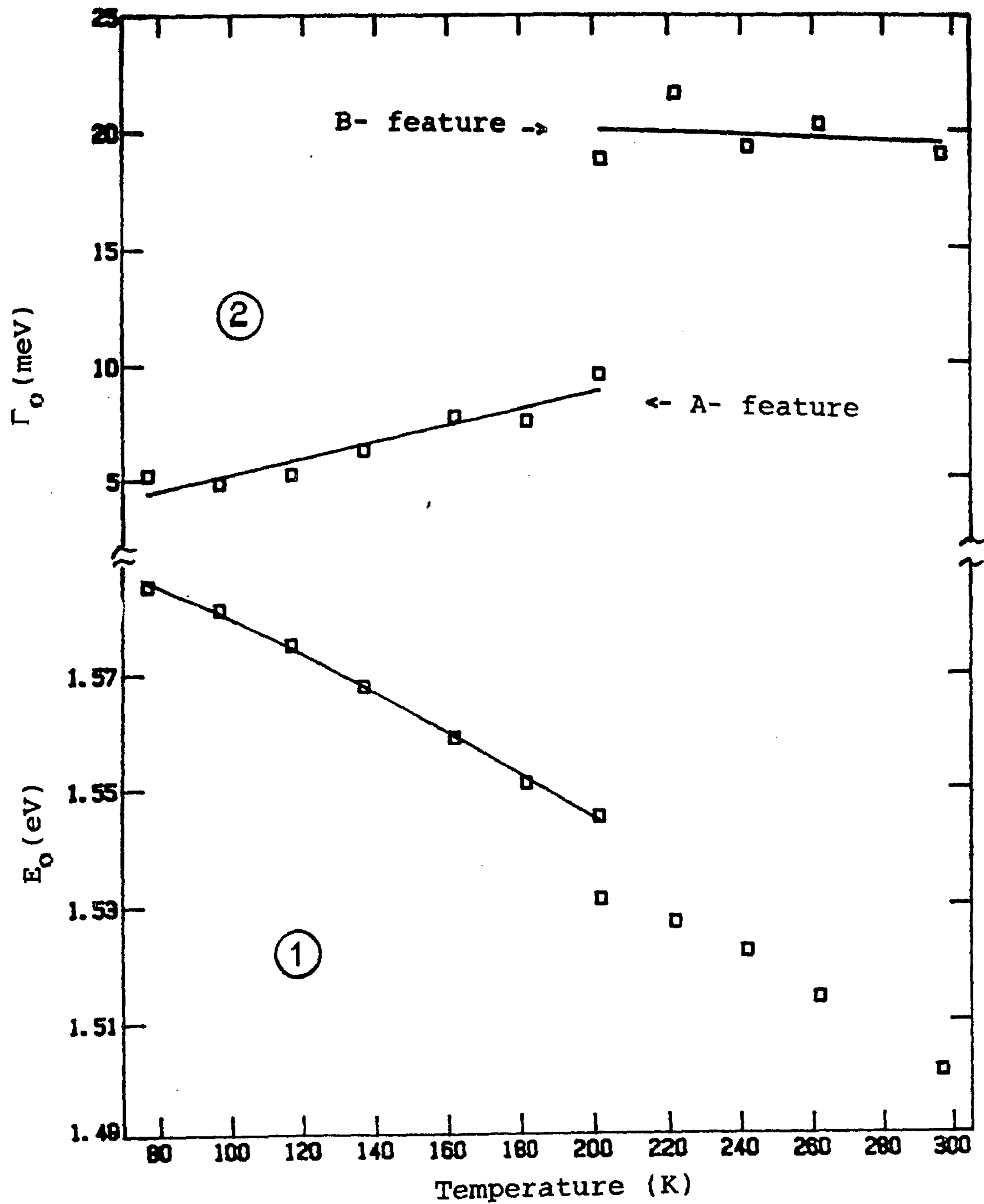

Fig.24

Temperature dependence of E_0 transition energy and broadening parameter for CdTe.
1- transition energy
2- Γ_0 (broadening parameter)

disappearance of the "A" feature is still not answered.

The mechanism involving the impurity- (defect-) related level described above seems to be an appealing explanation for yet another reason. The temperature dependence of the broadening of the "B" feature also provides evidence in favor of the donor level mechanism, as will be discussed later.

Since we assume that the peak "A" represents correctly the energy of the E_0 transition, we concentrate our attention on this peak. The temperature dependence of the "A" peak was fit to the Varshni formula yielding:

$$\begin{aligned} E_0(0) &= 1.596 \pm .005 \text{ eV} \\ \alpha &= -(5.4 \pm 0.1)\cdot 10^{-4} \frac{\text{eV}}{\text{K}} \\ \beta &= 219 \pm 79 \text{ K} \end{aligned} \tag{42}$$

The solid line in Fig.24 represents this fit result. The result of the linear fit yielded:

$$\frac{dE_0}{dT} = -(3.3 \pm 0.2)\cdot 10^{-4} \frac{\text{eV}}{\text{K}} \tag{43}$$

which is consistent with the value $\cong 3\cdot 10^{-4} \frac{\text{eV}}{\text{K}}$ obtained in Ref. 10.

The temperature dependence of the Γ_0 was fit to the linear relation[44]:

$$\Gamma_A = (1.7 \pm .2) \pm (3.5 \pm 0.2)\cdot 10^{-2} T \text{ meV} \tag{44}$$

The temperature dependence of the broadening parameter of the "B" feature was also obtained. It is

almost flat with the temperature coefficient $\cong -5 \cdot 10^{-3}$ $\frac{meV}{K}$. This can be explained within the assumption that the impurity levels are responsible for the "B" feature. Since the broadening introduced by the donor levels (as a result of a small lifetime or a number of long- lived levels 'bunched up') is larger than the broadening introduced by the valence band, we observe only the impurity- related component of the broadening which is almost insensitive to the temperature changes.

The temperature dependence of the E_1 transition has been previously evaluated experimentally by reflectivity[57,75], absorption[76] and thermoreflectance[46] studies. Cardona and Greenway[75] have determined the reflectivity spectra at only two temperatures, i.e. 77 K and 300 K. Although Refs 57, 76 and 46 performed measurements in a range of temperatures, their results are only sufficient to determine the linear dependence, i.e. dE_1/dT. Theoretical calculation of Tsay, et al[77] also lists only dE_1/dT, although it provides the non-linear dependence for other II-VI compounds.

Table VII presents a comparison of our work with the results of prior investigations. To facilitate the comparison, we have evaluated the linear temperature dependence of our data by procedures corresponding to the above works. For example, to correlate our results with Ref.75 we used only 77 K and 296 K points of our

data and obtained:

$$\frac{dE_1}{dT} = (6.8 \pm 0.6)\cdot 10^{-4}\ \frac{eV}{K} \qquad (41)$$

For the sake of completeness we included in Table VII the results of theoretical work of Tsay, et al[77]. As can be seen from the table, the disagreement between the results of Ref. 77 and our data is very large. Unfortunately, Ref. 77 does not list the temperature range used to obtain the value of dE_1/dT. Therefore, one possible cause of the discrepancy may be that the range which we used to compute dE_1/dT (77 K - 296 K), is different from the one used in Ref. 77. More importantly, these calculations were based on estimating only the Debye- Waller term[5] and did not incorporate the self- energy term, which has been shown to dramatically improve the agreement with experiment for GaAs[58]. That may also have been the cause of the disagreement.

In conclusion we have measured dependence of PR signal in E_0 and E_1 transition regions in the 77 K- 297 K range.

We have found that at temperatures higher than 202 K the optical spectra in E_0 region are dominated by transitions from the valence band to a donor level. The temperature dependence of the E_0 transition is in good agreement with the work of Camassel et al[10].

We have obtained, in addition to the linear temperature dependence of the E_1 transition energy in CdTe, the non- linear component of the dependence, i.e., Varsni coefficients α and β. The comparison of the obtained linear temperature dependence to the results of previous investigations showed the best agreement with the work of Rodzik and Kisiel[57], the most recent prior measurement.

Table VII

Experimental and theoretical values of the linear temperature coefficient dE_1/dT of the E_1 optical feature in CdTe. We have evaluated dE_1/dT by procedures corresponding to the relevant previos experimental studies.

This work (10^{-4} eV/K)	Previos results (10^{-4} eV/K)
-6.8 ± 0.6	-5.5[a,c]
-6.8 ± 0.2	-7.05[a,d]
-6.8 ± 0.2	-5.0[a,f]
-6.8 ± 0.2	-5.5[a,f]
-6.8 ± 0.2	-4.5[b,g]

a - Experiment
b - Theory
c - Ref. 75
d - Ref. 57
e - Ref. 76
f - Ref. 46
g - Ref. 77

Chapter IV

Raman Spectroscopy

In recent years, due to the ready availability of lasers, Raman scattering (RS) technique has become one of the most powerful methods for the investigation of elementary excitations in solids. In semiconductors Raman scattering has been used to study phonons, single particle and collective excitations, and the properties of the defects and disorder in semiconductor alloys. Since Raman scattering is a second order process, important symmetry information can be derived from the Raman spectra not available from the first- order processes. Furthermore, since Raman scattering depends on the electron- phonon interaction, the scattering intensity is a function of the electronic band structure. The resonance Raman scattering (RRS) method based on this dependence makes it possible to obtain information on electronic structure of the solids and the electron- phonon interaction.

4.1 Macroscopic Description of Raman Scattering

In Raman scattering experiment, light from an intense, spectrally narrow source of frequency ω_i is absorbed by a sample. A laser is usually used as a light source. One observes the frequency of the light scattered from the sample at lower frequencies ω_s (Stokes' radiation) or higher ones (Anti- Stokes' radiation) . The difference between the two frequencies is due to the fact that not only a scattered photon is created in the scattering process, but also a second excitation (with frequency ω_j) is created (or annihilated). In this work we shall only discuss Raman scattering by phonons. Only optical phonons give rise to Raman scattering as discussed further. The energy conservation can be written as:

$$\hbar\omega_i = \hbar\omega_s \pm \hbar\omega_j \qquad (45)$$

Therefore if ω_i is known, by measuring the ω_s one gets information about the frequency of the created phonon ω_j. We can also write the conservation of momentum:

$$\hbar\vec{k}_s = \hbar\vec{k}_i \pm \hbar\vec{q}_j \qquad (46).$$

The energy of the exciting radiation is in a region where $\hbar\omega_i >> \hbar\omega_j$, since the energy of the visible light photons is approximately 2 eV and the typical phonon energy is of the order of 30 meV. Therefore we can write $|\vec{k}_i| \cong |\vec{k}_s| = k$. The conservation of momentum can then

be written in the form:

$$q_j = 2k\sin\left(\frac{1}{2}\phi\right) = \frac{2\,\omega\, n(\omega)}{c}\sin\left(\frac{1}{2}\phi\right) \qquad (47)$$

where ϕ is the angle between the incident and scattered directions and $n(\omega)$ is the index of refraction of the medium at ω. Thus the wave vector of the phonon involved in the scattering process depends on the scattering angle. For the visible light usually employed in the Raman measurements, the value of k is between 10^4 and $10^5\ cm^{-1}$. This is at least 10^3 times smaller than the wave vector at the edge of the Brillouin zone q_{max}:

$$q_{max} = 2\pi / a_l \qquad (48a)$$

where a_l is the lattice constant. Therefore we can say that RS in perfect crystals probes phonons from the center of the Brillouin zone:

$$q_j \cong 0 \qquad (48b)$$

This is a very important selection rule. Also, note that acoustic phonons will have very small energies at the zone center and due to the capabilities of the equipment used in RS experiments will not be measured.

We can show in a simple way that Raman spectra are due to the modulation of the polarizability of the sample by a vibrational normal mode. The polarizability is a symmetric second rank tensor $\chi_{\mu\nu}$ which relates an electric field E_μ to a polarization P_ν:

$$P_\nu = \chi_{\nu\mu} E_\mu \qquad (49)$$

There is a connection between the polarization of the sample and the measured scattered intensity. We shall assume for simplicity that we are dealing with a single frequency component of the polarization $\vec{P}$ and that we analyze the scattered electromagnetic wave by picking up only a component of the scattered electric field E_s parallel to a unit vector $\vec{\varepsilon}^s$. Then for the measured component of scattering intensity I_s we can write:

$$I_s \propto | \vec{\varepsilon}^s \cdot \vec{P}_s |^2 \tag{50}$$

Let us expand the polarizability of the sample in terms of the vibrational normal coordinates. Dropping the tensor indexes belonging to χ itself we write:

$$\chi = \chi^{(0)} + \chi^{(1)} + \chi^{(2)} \tag{51}$$

where

$$\chi^{(1)} = \frac{\partial \chi}{\partial u_i} u_i \quad \text{and} \quad \chi^{(2)} = \frac{\partial^2 \chi}{\partial u_i \partial u_j} u_i u_j \tag{52}$$

where u_j is a time dependent normal j-th coordinate which can be written as:

$$u_j = u_{j0} e^{i\omega_j t} \tag{53}.$$

Consider now the effect of the electric field E_i incident on the sample. Writing E_i in time-dependent form as

$$E_i = E_0 e^{i\omega_i t} \tag{54}$$

and using Eqs.(49,51-54) we can write

$P = \chi^{(0)} + \chi^{(1)} u_{j0} E_0 e^{i[(\omega_i \pm \omega_j)]t} +$

$$+ \chi^{(2)} u_{jo} E_o e^{i[(\omega_i \pm 2\omega_j)t]} \quad + \ldots \tag{55}$$

The polarization of the sample, and (according to Eq.(50)) the scattered light intensity will have a component with a frequency $\omega_i \pm \omega_j$. This is the part of the scattering intensity which constitutes the first order Raman scattering. The term with the frequency component $\omega_i \pm 2\omega_j$ is the second order Raman scattering.

At this point we will introduce the Raman tensor. It is a tensor $R_{\mu\nu}$ proportional to $\chi^{(1)}_{\mu\nu}$. Different sources use different coefficients of proportionality.We are mentioning this tensor for the sake of completeness only.

4.2 Selection Rules

We can show using the macroscopic theory that only some vibrational modes can be observed by RS (i.e. are Raman active). Let us start with the classical Hamiltonian and assume that it is a function of the vibrational normal coordinates q_j and electric field E_μ. Only the potential energy (Φ) part of the Hamiltonian depends on E_μ and u_j. So instead of using the Hamiltonian, we shall expand Φ around $\Phi(0,0) \equiv \Phi_o$:

$$\Delta\Phi = \Phi - \Phi_o = \left(\frac{\partial^2 \Phi}{\partial E_\mu \partial u_j} \right) E_\mu u_j$$

$$+\frac{1}{2}\left(\frac{\partial^3\Phi}{\partial E_\mu \partial E_\nu \partial u_j}\right)E_\mu E_\nu u_j + \dots \qquad (56).$$

There are no lower order terms since we are expanding at the minimum of the potential energy. The last term can be written as

$$\frac{1}{2}\left(\frac{\partial \chi_{\mu\nu}}{\partial u_j}\right)E_\mu E_\nu u_j \qquad (57)$$

By comparison with Eq.(52), we see that this is the $\chi^{(1)}$ term responsible for the Raman scattering. Thus, in order for RS to exist, we must have non-zero $\frac{\partial \chi_{\mu\nu}}{\partial u_j} \equiv \chi^{(1)}_{\mu\nu,j}$. According to the Newman principle, to fulfill this condition the following must hold (see p.63 of Ref.1):

$$\Gamma(\chi_{\mu\nu})\otimes\Gamma(u_j)\subset\Gamma_1 \qquad (58)$$

that is the direct product of the representations according to which $\chi_{\mu\nu}$ and u_j transform ($\Gamma(\chi_{\mu\nu})$ and $\Gamma(u_j)$, correspondingly) must include a totally symmetrical representation Γ_1. An equivalent statement which is more convenient to deal with can be written:

$$\Gamma(\chi_{\mu\nu})\subset\Gamma(u_j) \qquad (59).$$

Now, let us apply Eq.(59) to the case of zincblende materials. Being a symmetric tensor, $\chi_{\mu\nu}$ transforms as a product $x_\mu x_\nu$. Under the operations of the point group T_d this product transforms according to the following irreducible representations (see Ref.1,78):

$$\Gamma(\chi_{\mu\nu}) = \Gamma_1+\Gamma_{12}+\Gamma_{25}+\Gamma_{15} \qquad (60).$$

The next step is to find the representation for normal coordinates and check if it is contained in the expression for $\Gamma(\chi_{\mu\nu})$. This procedure is described in detail in Refs.1,78. It leads to the result:

$$\Gamma(u_j) = 3\Gamma_{15} \tag{61}$$

meaning that we deal with triply degenerate Γ_{15} phonons (acoustic and optical branch) at the Brillouin zone center. Comparing this to Eq.(59), we find that the phonons are Raman active. Checking the basis functions for the Γ_{15}, we find that they are x, y, and z and therefore the normal coordinates are simply directed along x, y and z axes (i.e. <100>, <010>, and <001> directions) in the crystal.

4.3 Polarization Selection Rules

For opaque samples (such as the ones used in this work), it is usual to use backscattering geometry: both the incoming and outgoing beam directions are selected normal to the surface and opposite in direction[23]. Depending on the relative direction of the incoming beam polarization, outgoing beam analyzer and the orientation of the crystal axes, certain Raman active phonons may not be observed in Raman spectrum. These polarization selection rules come into play, because the scattering intensity is proportional to (compare to Eq.(50))

$$|\varepsilon^{s}_{\mu}\circ\chi^{(1)}_{\mu\nu,j}\circ\varepsilon^{l}_{\nu}|^{2} \tag{62}$$

Therefore, we will be able to find the selection rules for any mode j after finding a particular form of $\chi^{(1)}_{\mu\nu,j}$. To find $\chi^{(1)}_{\mu\nu,j}$ we shall follow the approach of Anastassakis[74]. Consider the last term in Eq.(56):

$$\delta^{3}\Phi = \frac{1}{2}\left(\frac{\partial^{3}\Phi}{\partial E_{\mu}\partial E_{\nu}\partial u_{j}}\right)E_{\mu}E_{\nu}u_{j} = \chi^{(1)}_{\mu\nu,j}\cdot E_{\mu}E_{\nu}u_{j} \tag{63}.$$

Both $E_{\mu}E_{\nu}u_{j}$ and $\chi^{(1)}_{\mu\nu,j}$ transform according to the same representation and their product $\delta^{3}\Phi$ is a scalar. This is possible only if the representation is the totally symmetric Γ_1. Now, since $E_{\mu}E_{\nu}u_{j}$ transforms as Γ_1 and u_j transforms as Γ_{15} of T_d, the product $E_{\mu}E_{\nu}$ must also transform as Γ_{15}, according to the generalized theorem of Unsöld[79]. Using the basis function tables[1] for the T_d, we find that the symmetric product $E_{\mu}E_{\nu}$ transforms as (xy, yz, xz). Therefore, the non-zero components of $\chi_{\mu\nu}$ are χ_{xy}, χ_{yz}, χ_{xz} and components with the reversed order of indexes. Then for the phonons along x, y, and z, we have the following Raman tensors correspondingly:

$$\begin{pmatrix} 0 & 0 & 0 \\ 0 & 0 & d \\ 0 & d & 0 \end{pmatrix}:u_x\ ,\ \begin{pmatrix} 0 & 0 & d \\ 0 & 0 & 0 \\ d & 0 & 0 \end{pmatrix}:u_y\ ,\ \begin{pmatrix} 0 & d & 0 \\ d & 0 & 0 \\ 0 & 0 & 0 \end{pmatrix}:u_z \tag{64}.$$

In this work we have studied Raman scattering from the (110) surface of the zincblende crystals; and, therefore, it is of interest to us to find out the selection rules for this particular case. In this case

$\vec{z}'$ is along (110) direction and we have a choice of two polarization configurations. Let us define two new sets of axes[79,80]:

$$x_2 = \langle 001 \rangle \qquad x_2' = \frac{1}{\sqrt{6}} \langle \bar{1}12 \rangle$$

$$y_2 = \frac{1}{\sqrt{2}} \langle 1\bar{1}0 \rangle \qquad y_2' = \frac{1}{\sqrt{3}} \langle 1\bar{1}1 \rangle \tag{65}$$

$$z_2 = \frac{1}{\sqrt{2}} \langle 110 \rangle \qquad z_2' = \frac{1}{\sqrt{2}} \langle 110 \rangle$$

The Raman tensors relative to the x_2, y_2, and z_2 axes are[79,80]:

$$\begin{bmatrix} 0 & d & 0 \\ d & 0 & d \\ 0 & d & 0 \end{bmatrix} \qquad \frac{1}{\sqrt{2}}\begin{bmatrix} 0 & 0 & -d \\ 0 & 0 & d \\ -d & 0 & 0 \end{bmatrix} \qquad \frac{1}{\sqrt{2}}\begin{bmatrix} 0 & 0 & d \\ 0 & 0 & d \\ d & d & 0 \end{bmatrix} \tag{66}$$

$$u_{x_2} - \mathrm{TO} \qquad u_{y_2} - \mathrm{TO} \qquad u_{z_2} - \mathrm{LO}$$

Similarly the Raman tensor for the x_2', y_2', z_2' system can be obtained. The polarization selection rules are given in Table VIII. Note, that only TO phonons are allowed for backscattering from [110] face.

4.4 Microscopic Theory

Raman scattering is a result of indirect photon-electron- phonon interaction[23]. With the help of the Fermi's Golden rule we may write the following for the scattering cross section σ[81]:

$$\sigma \propto |\varepsilon^{s}_{\mu} \circ \chi_{\mu\nu,j} \circ \varepsilon^{l}_{\nu}|^2 \propto |W_{fi}|^2 \qquad (67)$$

where W_{fi} is the matrix element for scattering the photon from the state i to state s with the creation of the given phonon. The process is illustrated in Fig.25a. The lowest order contribution to W_{fi} is third order in interactions[81]:

$$W_{fi} \propto \sum_{\lambda_1 \lambda_2} \frac{\langle 0;s,\bar{n}+1|H'|\lambda_1\rangle\langle\lambda_1|H'|\lambda_2\rangle\langle\lambda_2|H'|0;i,\bar{n}\rangle}{(E_{\lambda_1} - E_{o,i})(E_{\lambda_2} - E_{o,i})} \qquad (68)$$

where:

$\langle 0;i,\bar{n}|$ is the initial state with the electronic system in ground state, $\bar{n}$ phonons and the photon in the initial state.

$\langle 0;s,\bar{n}+1|$ is the final state with the electronic system in ground state, $\bar{n}+1$ phonons and the photon in scattered state.

$\langle\lambda_1|$ and $\langle\lambda_2|$ are the intermediate states of the system and

$E_{i,o}$ E_{λ_1} and E_{λ_2} are the energies of the initial and the two intermediate states.

H' is the total perturbation

$$H' = H_R + H_{EL} \qquad (69),$$

which includes the interaction of the radiation with the electrons H_R and the electron-phonon interaction H_{EL}.

There are six possible orderings that can contribute to W_{fi} in Eq.(68). The term contributing strongly to RS and having the strongest

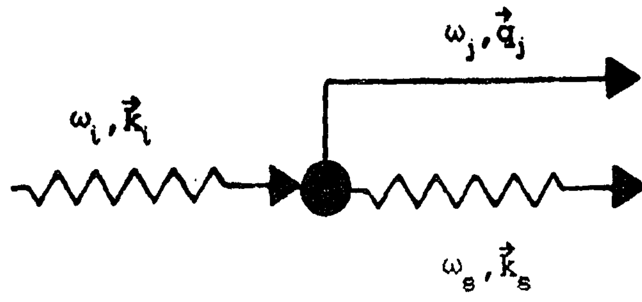

(a)

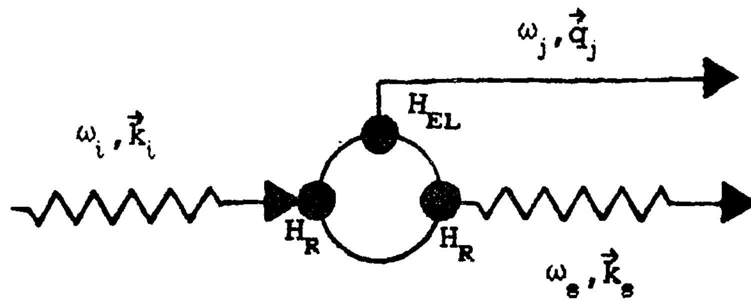

(b)

<u>Fig.25</u>

First order Raman scattering.
(a)- General description of the process. Scattering of the incident photon $(\omega_j, \vec{k}_i)$ with creation of the phonon $(\omega_j, \vec{q}_j)$and scattered photon $(\omega_s, \vec{k}_s)$.
(b)- The three- step scattering process described in text. There are five other diagrams with the different order of interactions which contribute to the scattering process (a)

Table VIII

Polarization selection rules for Raman scattering from (110) surface.

Polarization configuration	Phonon mode		
	$LO(z_2)$	$TO(x_2)$	$TO(y_2)$
$z(x_2,x_2)\bar{z}_2$	0	0	0
$z(x_2,y_2)\bar{z}_2$	0	0	d^2
$z(y_2,y_2)\bar{z}_2$	0	d^2	0
	$LO(z_2')$	$TO(x_2')$	$TO(y_2')$
$z(x_2',x_2')\bar{z}_2$	0	$2/3d^2$	$1/3d^2$
$z(x_2',y_2')\bar{z}_2$	0	$2/3d^2$	0
$z(y_2',y_2')\bar{z}_2$	0	0	$4/3d^2$

resonance[78,81,82] is depicted in Fig.25b. It can be viewed as a three step process:

1. The absorption of the incident photon causes a virtual transition leading to the creation of the electron- hole pair.

2. The phonon is absorbed (or created) which process causes the change of the state of the electron-hole pair.

3. The emission of the final photon which is accompanied by the annihilation of the electron- hole pair.

Transitions 1 and 3 are caused by the electron-radiation interaction H_R and transition 2 by the electron- lattice interaction H_{EL}. The energy is conserved only for the process as a whole whereas the wave vector is conserved for each step. The virtual intermediate states of the system are the states of the electron- hole pairs. Contribution of this term to $\chi_{\mu\nu}$ is[78,82]:

$$\chi^{(1)}_{\mu\nu} \propto \sum_{\mu\ \nu} \frac{\langle 0|p_\mu|m\rangle\langle m,\bar{n}\pm 1|H_{EL}|l,\bar{n}\rangle\langle l|p_\nu|0\rangle}{(E_m - h\omega_s)(E_l - h\omega_i)} \qquad (70)$$

where $\langle 0|$, $\langle m|$, and $\langle l|$ are the ground and two intermediate states of the electronic system; $\langle l,\bar{n}|$ is the wavefunction describing the electron- phonon system with $\bar{n}$ phonons and electronic system in state l; ω_i and ω_s are the frequencies of incident and scattered

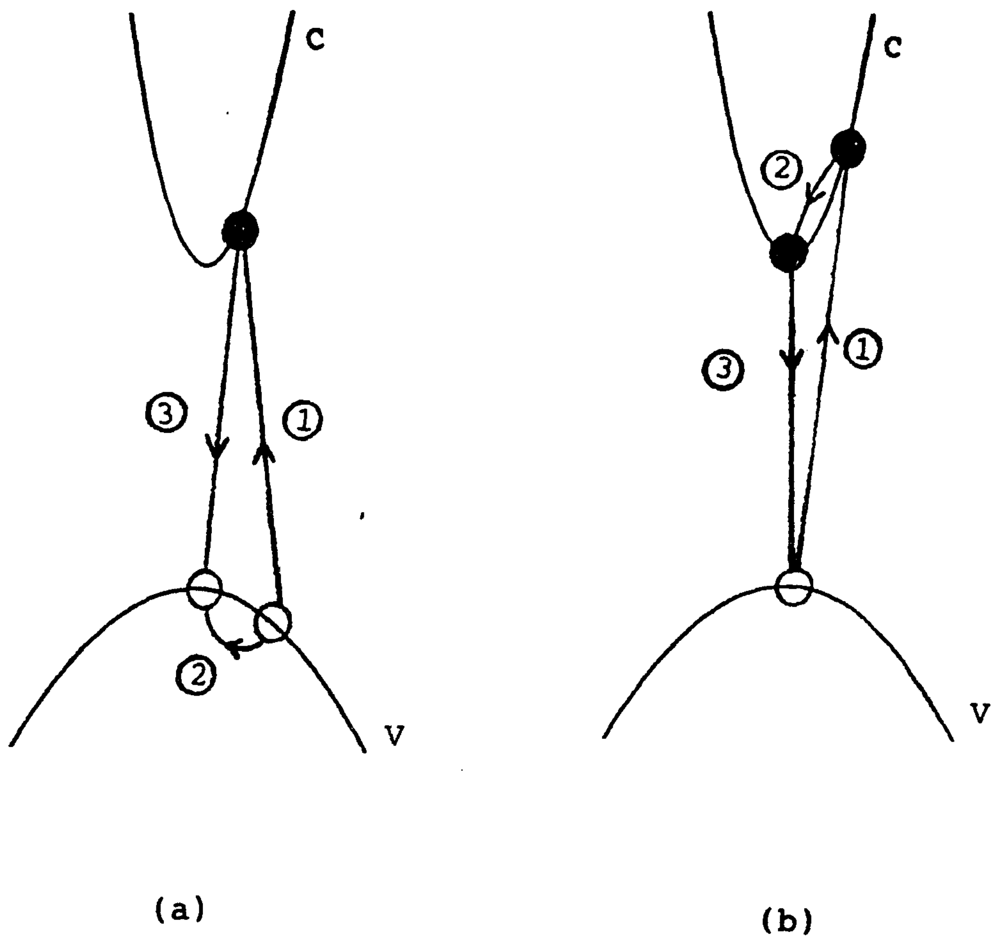

Fig.26a

Diagrams of the transitions producing two- band contributions to the Raman tensor.

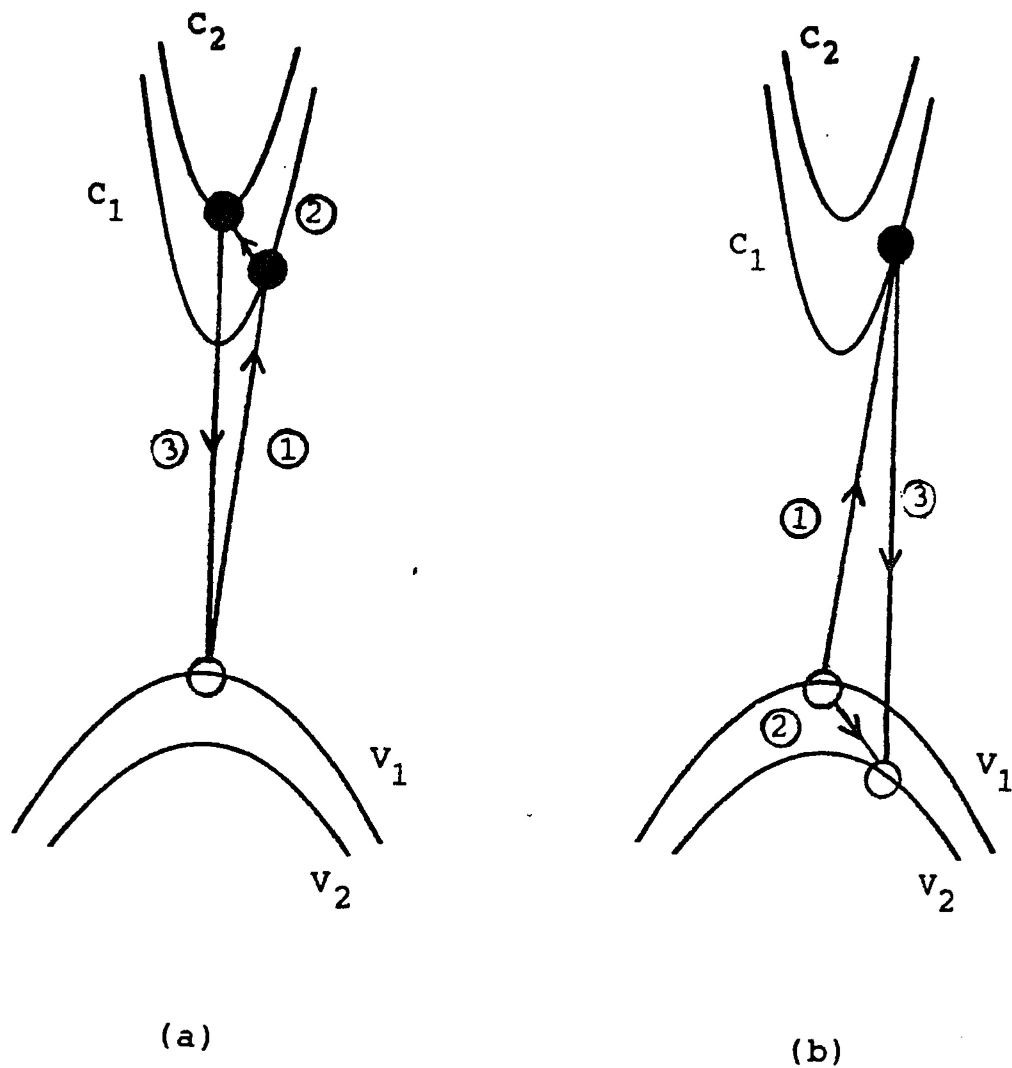

Fig.26b

Diagrams of the transitions producing three- band contributions to the Raman tensor.

beam and E_l, E_m are the energies of the electronic system in intermediate states. Five other terms contributing to $\chi^{(1)}$ can be found in Ref.82. One can think of various kinds of intermediate states for the processes described by Eq.(70). The intermediate states may be thought of as the ground and excited one-electron states of the crystal[82]. For the semiconductor crystal with empty conduction bands and filled valence bands we can have the processes pictured in the Fig.26a,b. Calculations have also been done assuming the intermediate states to be of the excitonic nature (both free[78,81] and bound[83] excitons have been considered).

4.5 Resonance Raman Scattering

It follows from Eq.(70) that when the energy of either the incident or scattered light is close to the energy of an electronic transition in a solid, the scattering amplitude is enhanced. This phenomenon is called the resonance Raman scattering (RRS). The RRS can be used to study both electronic and vibrational properties of solids. The information about the electronic properties can be derived from light reflection or absorption experiments independently. Use of this information together with the results of RRS allows to obtain a great deal of information on the

nature of the electron- phonon interaction (see review articles Ref.78,84).

Sometimes vibrational LO- modes forbidden by the usual symmetry selection rules (see Table VIII), can be observed in RRS near resonance. The mechanisms of RRS which lead to this forbidden scattering are reviewed by Menedez and Cardona in Ref.78 and 84. Their investigation have shown that:

1. External electric fields (such as the ones caused by the band bending at the surface) can introduce new terms in Eq.(56). These terms will have selection rules different different from the ones obtained for atom displacement [Eq.(57)]. We shall refer to this effect as a surface field (SF) effect.

2. Observation of vibrations with a non-zero wave vector will also produce forbidden scattering. In this case, the scattering cross section is proportional to q^2. We shall refer to this effect as a linear- q (LQ) effect.

3. Intra- band Fröhlich interaction, when included into H_{EL}, will produce forbidden terms. This is the interaction of the long- range electric field produced by the LO phonons with the electrons.

4. Godolin and Rashba[85,86] introduced higher-order, impurity- induced, LO- phonon scattering also leading to forbidden terms near electronic resonances.

The first two mechanisms belong to the class of morphic effects[79,80]. The (LQ) effect is observed in the spectral regions with large absorption. The RS probes a layer of the sample equal to the penetration depth of the light. This thin layer may not have the full symmetry of the crystal. In the case of the (SF) effect, the full crystal symmetry is relaxed by the presence of the electric field at the surface. Thus χ may depend explicitly on the spatial dispersion of the phonon displacement ($\nabla u_j = iu_j q_j$) and the external electric field E_j. As we can see, in the case of (LQ) mechanism, χ depends on the wave vector q. The expression for scattering cross section Eq.(51) can be generalized further by including terms which reflect the dependence of χ on the wave vector (q) and the external electric field (E):

$$\chi^{(q)} = \frac{\partial \chi}{\partial \nabla u_j} iu_j q_j \qquad (71a)$$

$$\chi^{(E)} = \frac{\partial \chi}{\partial u_j \partial E_k} u_j E_k \qquad (71b).$$

The polarization selection rules for these two mechanisms are identical. They can be found using the method we employed for the deformation potential-induced RS (See Refs.(79,80)).

The Frölich interaction mechanism can be explained as follows[78]: Let us consider IR- active phonons in

zincblende material. where a longitudinal polarization, resulting from the vibration exists. The polarization induces the electric field of the magnitude $\mathcal{E}$ which, in turn, produces a potential $i\mathcal{E}/q$. This potential is actually a part of the electron- phonon interaction H_{EL} which produces the forbidden scattering. Between the electronic states l and j such that:

$$\vec{k}_j = \vec{k}_l - \vec{q} \qquad (72)$$

the matrix elements of the H_{EL} are:

$$<(n+1),j|H_{EL}|n,l> = C_F\left[\frac{\delta_{jl}}{|q|} + <j|\frac{\vec{q}\cdot\vec{p}}{|q|}|l>(1-\delta_{lj})\right] \qquad (73)$$

The Frölich constant C_F is given by:

$$C_F = -i\left(\frac{\omega_{LO}}{2V_c}\right)^{1/2}\left(\frac{1}{\varepsilon_\infty} - \frac{1}{\varepsilon_{rf}}\right)^{1/2} \qquad (74)$$

where ε_∞ and ε_{rf} are the values of the dielectric function for very high frequencies (but still lower than the fundamental band gap energy) and very low frequencies. The first term in Eq.(73) is singular at q=0 and represents the intraband scattering. The divergent nature of this term in the $q \to 0$ limit is the source of the anomalies observed. The second term is nonsingular and represents the interband scattering. Raman tensor for forbidden LO scattering has been calculated using the singular (intraband) term of Eq.(73) by different investigators[78,81,83,87], each employing a different assumption concerning the nature

of the intermediate states. The matrix elements of Eq.(73) have been computed between the uncorrelated one-electron states[78,87], free excitonic states[81], and states of the excitons bound to impurities[83].

The last mechanism, proposed by Godolin and Rashba, constitutes, in effect, a fourth order process[85,86].They considered the effect of impurities on the first- order LO- scattering. The lowest- order scattering with participation of the impurity is shown in Fig.27. The incident photon creates an exciton which first scatters on the impurity and then on the phonon. The last interaction includes the term of H_{EL} which comes from the Frölich interaction. The scattering cross section of this mechanism is comparable to that of the Frölich interaction, since this mechanism involves the scattering on impurities which relaxes the wave vector conservation and permits a larger number of phonons to participate.

The important distinction between the Frölich interaction mechanism and impurity- induced scattering is that the resonance of the former is at $\hbar\omega_L = \hbar\omega_o + \hbar\omega_{LO}$ (outgoing resonance), whereas the latter has a resonance at exactly $\hbar\omega_o + \hbar\omega_{LO}/2$ (halfway between the ingoing and outgoing resonances).

The feature common to both mechanisms is that the tensor $\chi^{(1)}_{\mu\nu}$ is diagonal, i.e.

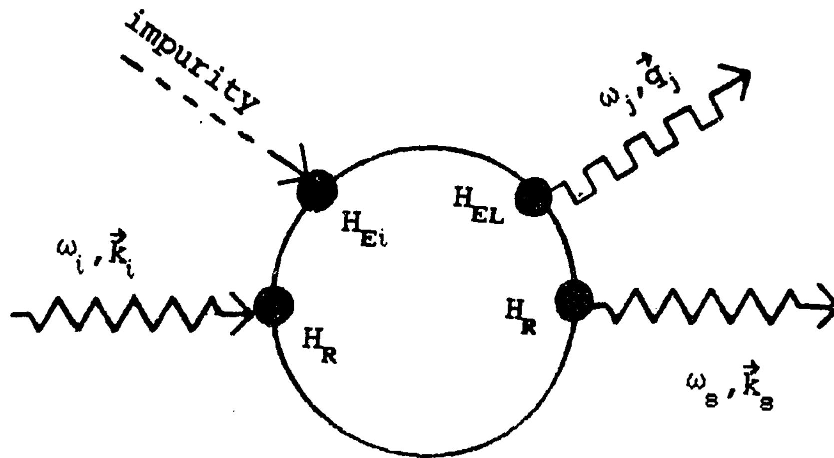

Fig.27

Diagram of a typical term contributing to the impurity induced scattering mechanism.
Note the extra scattering process (H_{Ei}) in comparison to the process on Fig.24. This interaction leads to the relaxation of the momentum conservation and, therefore the phonons with large wavevectors participate in the Raman scattering process.

$$\chi^{(1)}_{\mu\nu} = \begin{bmatrix} f & 0 & 0 \\ 0 & f & 0 \\ 0 & 0 & f \end{bmatrix} \tag{75}$$

which means that only $\vec{\varepsilon}_l \uparrow\uparrow \vec{\varepsilon}_s$ polarization is observed. This feature clearly distinguishes the last two mechanisms proposed for forbidden LO scattering from the morphic effects.

4.6 Experimental

Fig.28 shows the experimental setup for the Raman scattering measurements. The collimated monochromatic beam from a Ar ion laser (CR-6, Coherent, Inc.) was used as the incident radiation. We have used all possible green and blue lines of the Ar laser to measure the dependence of the RS cross section on the energy of the incident light. When the Ar gas plasma lines fell into the range of Raman measurement, we passed the incident beam through the interference filter before it reached the sample. The beam was then focused on the sample by a cylindrical lens (focal length= 80 mm). This allowed us to focus the beam into a line (approximate dimensions 0.3x4 mm) rather than a point, thus reducing the incident power density and minimizing the sample heating. We did not exceed a laser power of 200 mW. The backscattered light was collected at the entrance slit

of the spectrometer by a camera lens (focal length 135 mm, f=1.8). The large index of refraction of the sample[5] (≅ 4) ensured that both incident and scattered angles inside the semiconductor were small. The system of mirrors used to deliver the incident beam to the sample turned the beam's polarization in such a way that it was polarized in a horizontal plane. By introducing one more mirror, it was possible to make the polarization plane vertical. Therefore we had a choice of two perpendicular polarizations of the incident beam.

For the study of the polarization selection rules, we used a sheet analyzer (produced by Melles Griot, Inc.). Since the grating monochromator used in this work has a througput sensitive to the polarization of the analyzed light, the beam had to be depolarized before entering the monochromator. For tis purpose a "polarization scrambler" was placed in front of the entrance slit. The scrambler was a slightly wedged, approximately 3/4" thick, polished plate of single crystal quartz. Since the thickness of the plate varied slightly from point to point on the plate, the linearly polarized light passing it at different points had it's polarization turned by a different angle. Therefore, after traversing the "scrambler" the lineary polarized light became depolarized.

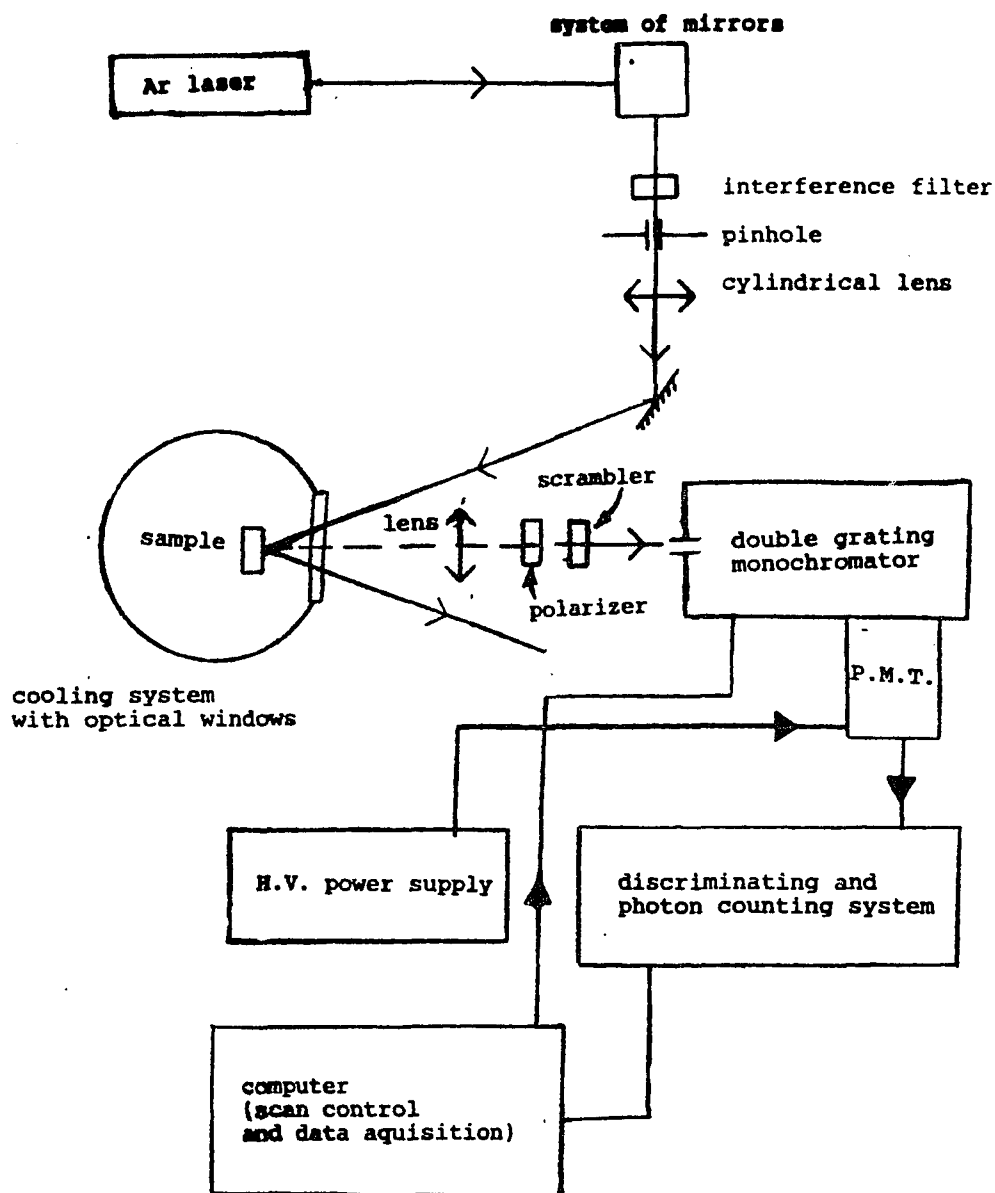

Fig.28

The experimental setup for the Raman scattering measurements.
P.M.T. stands for photomutiplier tube.

We used an SPEX 1401 0.85-meter double grating monochromator to analyze the spectrum of the scattered light. It was outfitted with an RCA N-40436 photomultiplier with cooled GaAs cathode. The signal was registered by the discriminating and photon counting system (SPEX DPC-2). The monochromator scanning system and the photon counter were interfaced with an IBM-XT computer, which controlled the scan and collected data, using in-house written software.

All our Raman measurements were done at low temperatures (77 K and 10 K). To acheive these temperatures, the samples were placed in a transfer line cooling system (Air Products LT-110-3) outfitted with optical windows made of fused quartz.

Two approaches can be used to derive the dependence of the Raman cross section on the energy of the incident light from the experimental results[78]. The first one computes the cross section using the geometry of the setup; the known spectral response of the monochromator and the detector; and, the dielectric constant of the material. The second approach - which we used in our investigation - compares the intensity of the Raman signal at each incident wavelength to that of the etalon.

We used CaF_2 as an etalon. CaF_2 is a well known[23,78] material with a constant Raman scattering

cross section in the spectral region that was investigated by us (≅ 2.4-2.7eV). We placed a thin (1mm) plate of CaF_2 on top of our samples' surfaces while measuring the Raman spectra. If the incident beam was focused slightly above or below the interface between the sample and the etalon a signal from the etalon would be affected. We estimate that the accuracy of the referance signal measurement was ±15%.

4.7 Review: Vibrational Spectra of $Hg_{1-x}Cd_xTe$

The vibrational spectra of the binary HgTe and CdTe compounds are well known. Raman measurements of these materials were carried out by Mooradian and Harman[24]. Their results are listed in Table IX. More detailed Raman study of HgTe was performed by Amirtharaj et al[70].

Compositional dependence of LO and TO phonons in $Hg_{1-x}Cd_xTe$ was investigated using both FIR reflection[27,28] and Raman scattering techniques[26]. In Fig.29, we show the compositional dependence of TO and LO phonon energies measured by Talwar et al[28] along with the results of theoretical calculations. As was discussed before, $Hg_{1-x}Cd_xTe$ displays a two-mode behavior.

In Fig.4, we show a Raman spectrum of

$Hg_{0.8}Cd_{0.2}Te$. measured by Amirtharaj et al[29]. Peaks at 122 and 140 cm^{-1} were identified as "HgTe-like" LO and TO phonons. A feature at 156 cm^{-1} was identified as degenerate "CdTe- like" LO and TO peaks. There is some question, however, whether this is a local vibration or the propagating phonon mode. For instance, Bedel et al[88] found that a similar mode in $AlIn_{0.8}P_{0.2}$was a local vibration. We shall address this question later.

These are the Raman peaks that are expected in a pseudo binary alloy with the two-mode behavior. Except for these anticipated features, samples of HgTe and some samples of $Hg_{1-x}Cd_xTe$ display a feature at approximately 107 cm^{-1} (see Refs.(27-29)) which is seen in Fig.4. This feature has been assigned to vibrations of Hg atoms substituted on Te sites[28,29]. This explanation seems reasonable, in view of reports that excessive load of Hg is required to grow stochiometric samples of $Hg_{1-x}Cd_xTe$[89]. However, the decisive evidence for such an assignment has not been presented.

A peak at 135 cm^{-1} was not seen in any samples of CdTe or HgTe by workers of Ref.29 or by any other group. Referring to known occurrences of fraction separation and Te precipitation in $Hg_{1-x}Cd_xTe$, Amirtharaj et al[29] proposed that the feature might be caused by the short-order clustering - the mechanism put forth in a similar case by Verleur and Barker[31]. Kozyrev et al[32] adopted

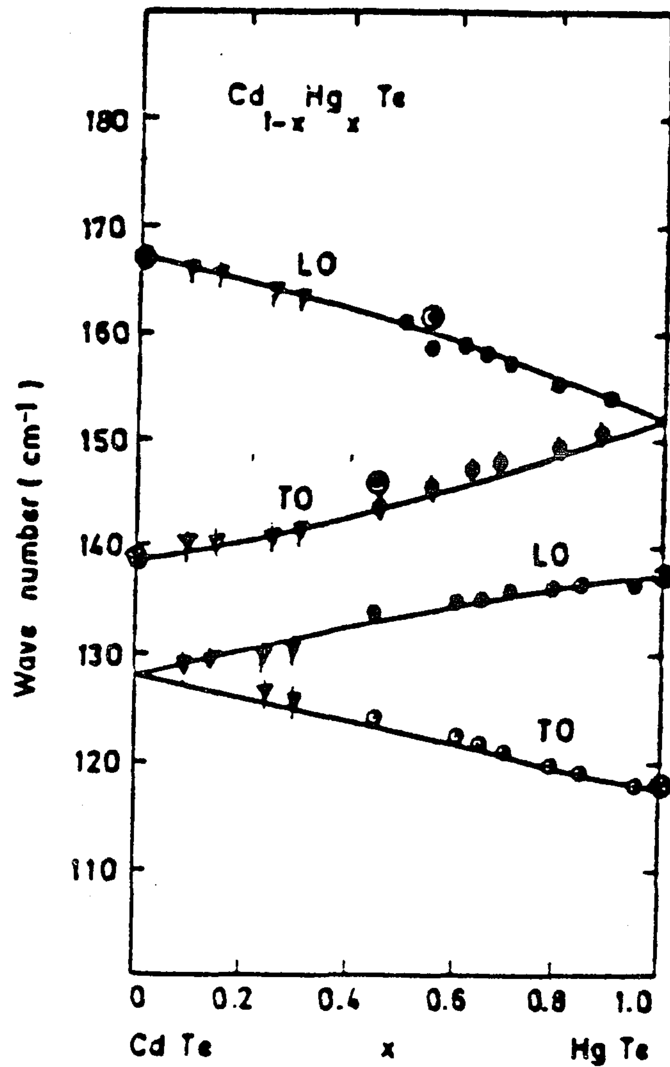

Fig.29

Compositional dependence of the vibrational frequencies in $Hg_{1-x}Cd_xTe$ (from Ref.28).

Table IX

Phonon energies as measured by Raman scattering.

After Ref.24.

Material	HgTe	CdTe
TO phonon (cm^{-1})	116	140
LO phonon (cm^{-1})	139	171

this mechanism to explain the FIR spectra of $Hg_{1-x}Cd_xTe$. They found that a considerable degree of short- range clustering was necessary to explain the results in the x= 0.4- 1.0 composition range.

Recent work by Fu and Dow[32] puts forth a different interpretation. They computed the spectral density of states for phonons in $Hg_{1-x}Cd_xTe$ using the recursion method. Their computation yields a vibrational mode around 135 cm^{-1} which is an integral part of the $Hg_{1-x}Cd_xTe$ vibrational spectrum. The computation does not take any clustering effects into consideration.

4.8 Sample Details

In this study we used two samples of $Hg_{1-x}Cd_xTe$ (with the composition x= 0.2 and x= 0.3) furnished by Santa Barbara Research Center. The samples were cut perpendicular to a <110> direction. They were polished mechanically using first 1μm and then 0.05μm grit alumina powder. During the first polishing cycle we removed 500μm layer of the material, during the second one- 100μm layer. The mechanical polishing was followed by the chemomechanical polishing using 0.05% Br solution in methanol. The approximate duration of the chemomechanical polishing was 4 min. In all polishing procedures we used Politex supreme polishing pads

(Rodel, Inc.).

The x=0.3 sample was the one used for the PR experiments (n- type bulk material in section 3.2). The E_1 and Γ_1 values for this sample are listed in Table IV.

4.9 Results and Discussion

We have used the Resonance Raman spectroscopy (RRS) to determine the local or non- local origin of the "CdTe- like" feature. We also used the RRS to obtain information on the mechanism of the forbidden Raman scattering in $Hg_{1-x}Cd_xTe$.

In this study we investigated the forbidden LO-scattering near resonance. We have measured Raman spectra in the backscattering configuration from the (110) surface of two $Hg_{1-x}Cd_xTe$ samples: one with composition x=0.2 at 10K and the other x=0.3 at 10K and 77K. The spectra taken with the various lines of Ar laser are shown in Figs.30-32. Some of the data displays a significant "sloping" background which is probably due to elastic scattering.

To allow an easier determination of the position and relative intensity of the spectral features, we used the following procedure to subtract the background: first, two sets of points were selected outside the

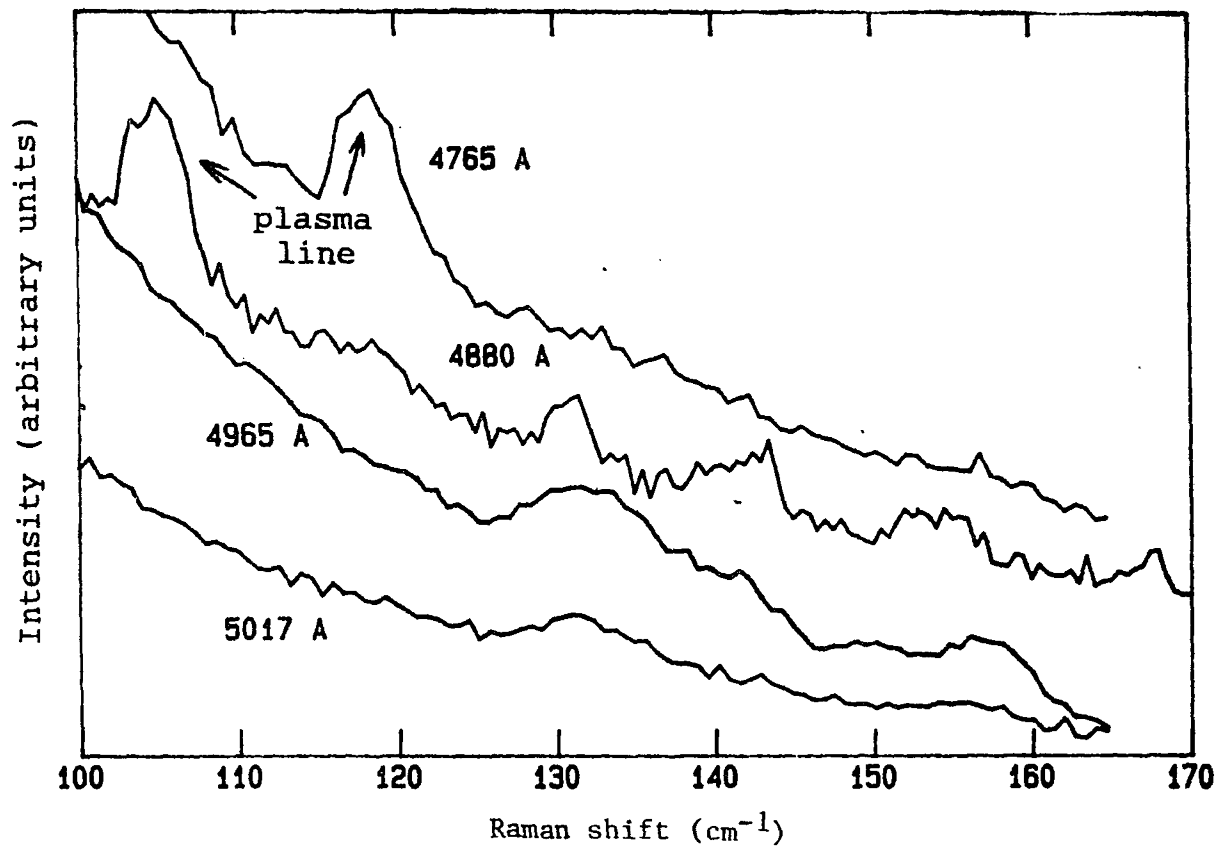

Fig.30

Raman scattering spectra for $Hg_{1-x}Cd_xTe$ x=0.3 sample at 77K.
The spectra are taken from a (110) face, scattered light polarization not analyzed.The peaks at $118cm^{-1}$ for the 4765A line and $104cm^{-1}$ for 4880A line originate from Ar gas plasma.

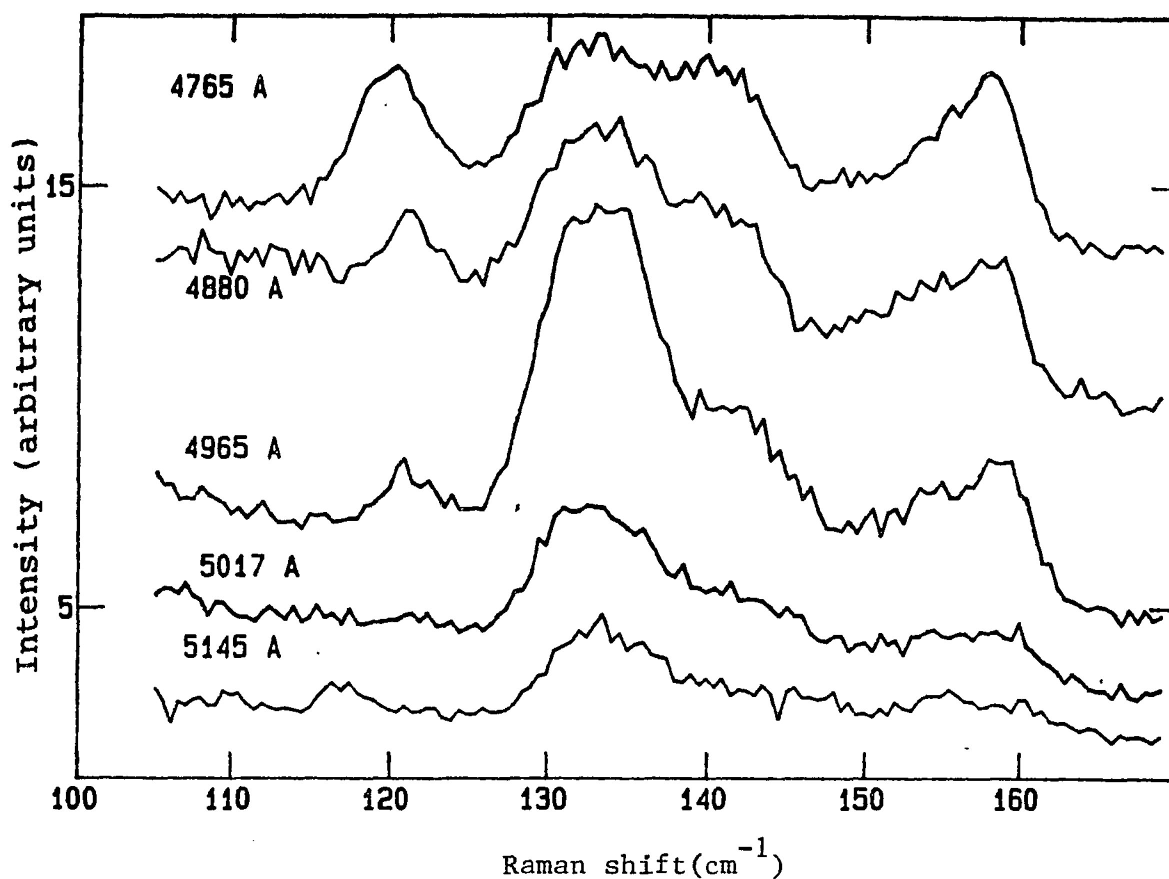

Fig.31

Raman scattering spectra for the $Hg_{1-x}Cd_xTe$ x=0.3 sample at 10K.
The spectra were taken from (110) face, scattered light polarization not analyzed. The $118cm^{-1}$ peak on the spectrum taken with 5145A laser line originates from the Ar gas plasma.

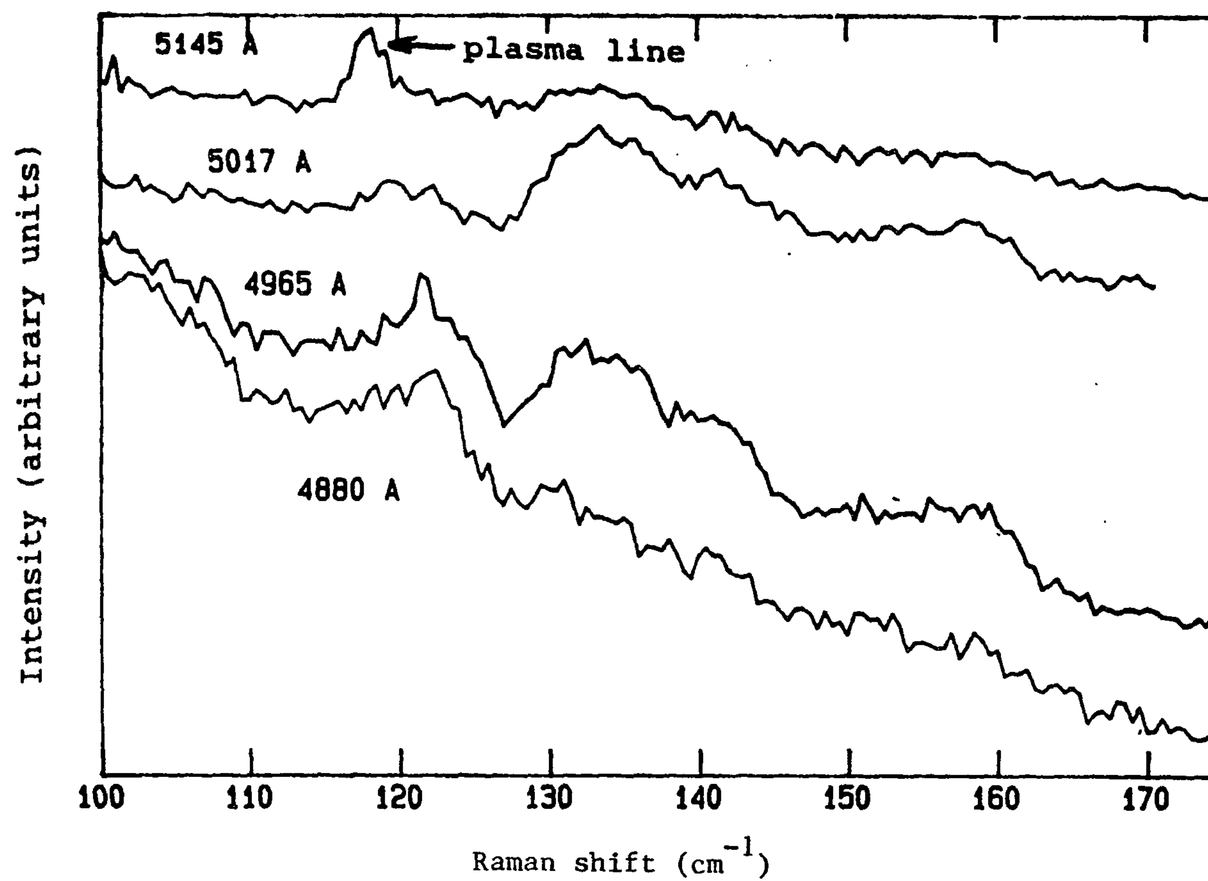

Fig.32

Raman scattering spectra for the $Hg_{1-x}Cd_xTe$ x=0.2 sample at 10K.
The spectra were taken from (110) face, scattered light polarization not analyzed.

region containing sharp Raman features. These are the points which belong to the featureless background (below $112cm^{-1}$ and above 162 cm^{-1} on the Raman shift scale) which arises from elastic scattering.

Then, these points were fit to a lineshape describing the bell- shaped spectrum of the laser line which is observed in the Raman spectrum due to elastic scattering. Based on our experience, Lorenzian lineshape centered on the zero Raman shift energy provides a good approximation to such a background:

$$\mathscr{L}(A,\Gamma,E) = \frac{A}{E^2+\Gamma^2} + B \qquad (76).$$

This lineshape with adjustable parameters A and B and fixed Γ was fit by the least square method to the set of points chosen. The parameter Γ was chosen to be equial to the value of the monochromator linewidth ($4.5cm^{-1}$) which corresponds to the slit setting we used. The obtained background was subtracted from the experimental spectrum. Examples of the procedure are shown in Figs.33 and 34. The compositional dependence of vibrational frequencies predicts rather small differences between the peak positions for x=0.2 and x=0.3 samples (see Ref.28, also Fig.29). Therefore, it is not difficult to make an assignment of the features for both samples based on previous investigation of the x=0.2 alloy[25,29,70]. For the x=0.2 sample we have: "HgTe-like" TO at $122cm^{-1}$; "clustering mode" at $134cm^{-1}$;

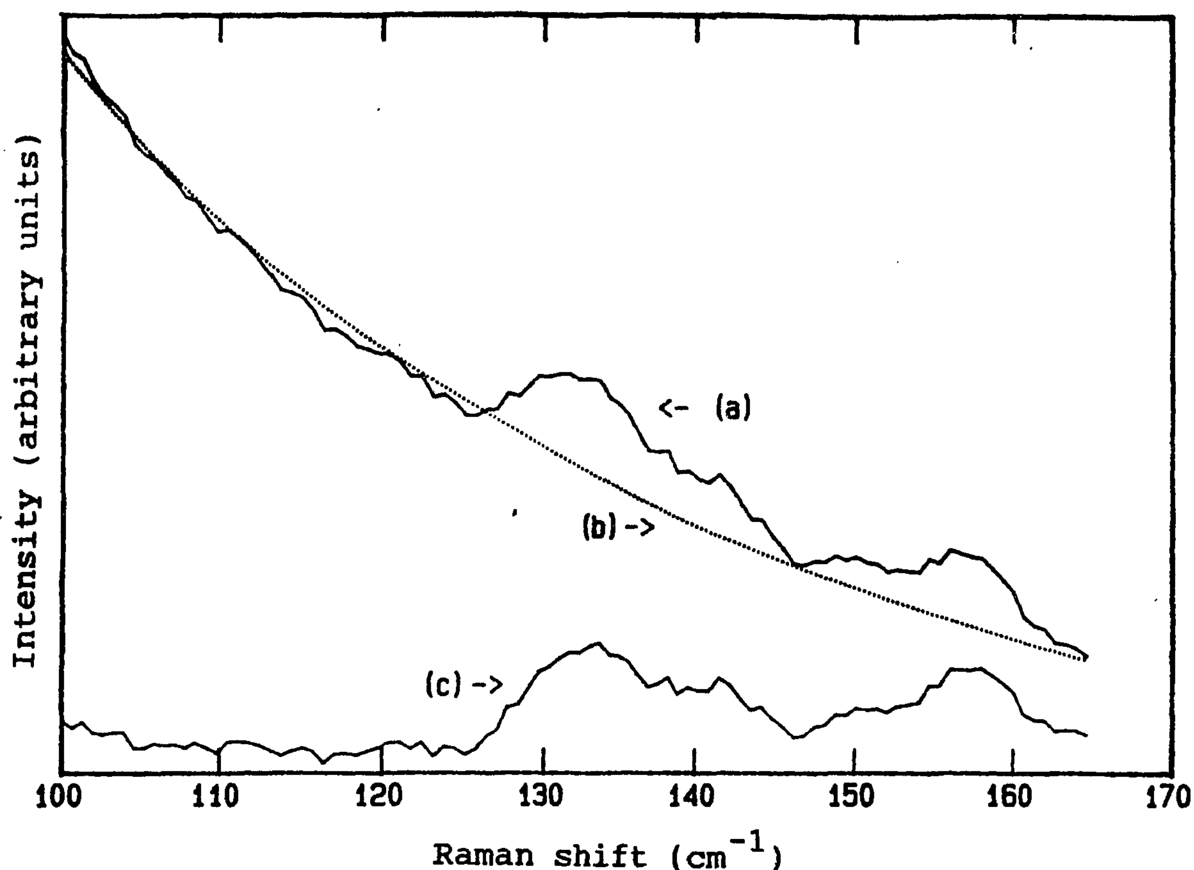

Fig.33

The procedure of subtracting the elastic scattering background from the spectra of $Hg_{1-x}Cd_xTe$ x=0.3 sample, taken at 77K, with 4965A excitation.
(a)- the experimental spectrum
(b)- the elastic scattering background obtained by the least square fit of Eq.(76) to the points below 112cm^{-1} and above 162cm^{-1}
(c)- the result of the background subtraction.

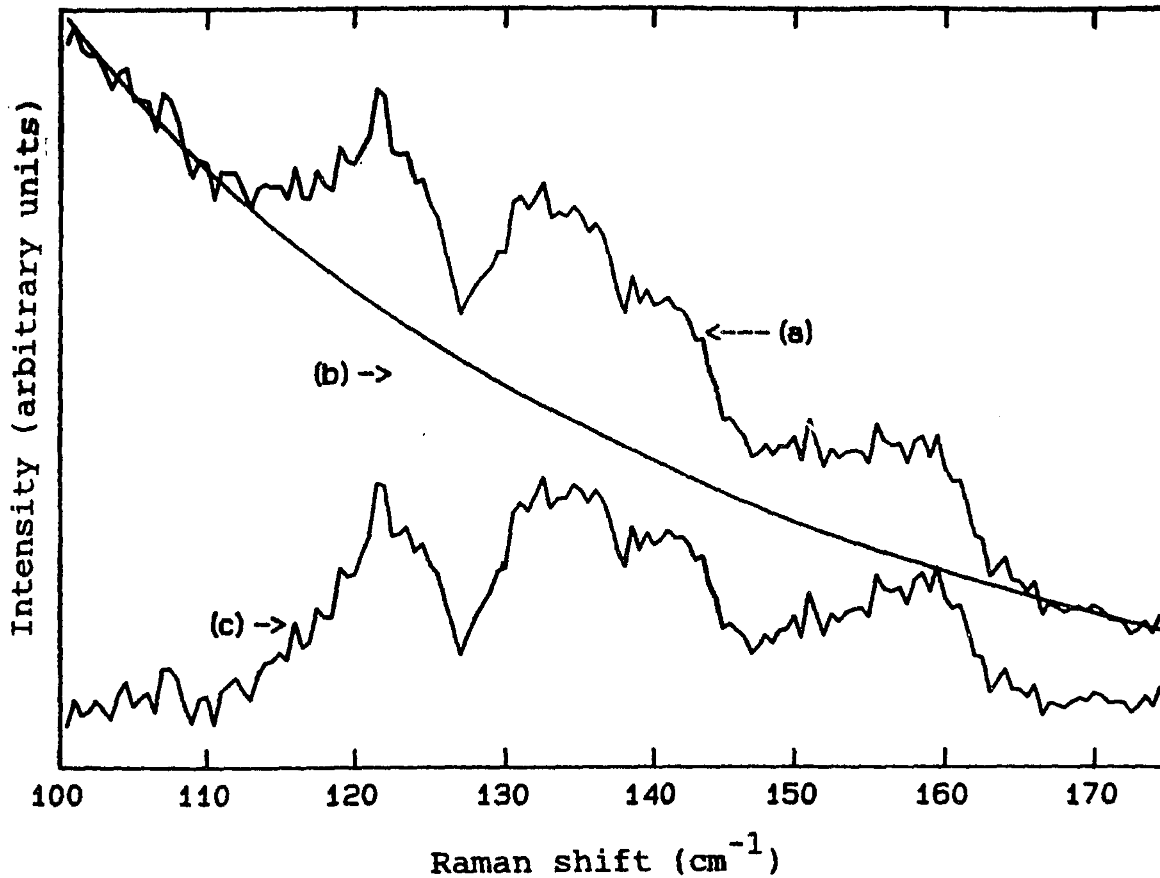

Fig.34

The procedure of subtracting the elastic scattering background from the spectra of $Hg_{1-x}Cd_xTe$ x=0.2 sample, taken at 10K, with 4965A excitation.
(a)- the experimental spectrum
(b)- the elastic scattering background obtained by the least square fit of Eq.(76) to the points below $112cm^{-1}$ and above $162cm^{-1}$
(c)- the result of the background subtraction.

"HgTe-like" LO at 140 cm^{-1} . A peak at 158 cm^{-1} is a "CdTe- like" LO with a small TO contribution (we shall abbreviate it as "LO+TO"). This peak has a shoulder at the low- energy side.

We shall discuss the origin of this shoulder later in the text. We give similar assignments for the x=0.3 sample: "HgTe-like" TO at 122cm^{-1}, "clustering mode" at 133cm^{-1}, "HgTe-like" LO at 140 cm^{-1} . A peak at 158 cm^{-1} is a "CdTe- like" LO+TO. It has a shoulder at the low- energy side just as in the x=0.2 case.

A. The Mechanism of Forbidden LO Scattering

We have chosen to study scattering from a (110) surface because the deformation potential-induced LO-scattering is forbidden by the polarization selection rules for any combination of incident and scattered beam polarizations (see Table VIII and Ref.90). This greatly simplifies our task, since we do not observe the interference of the forbidden with allowed scattering[84,91], which would make the picture much more complicated. We are also able to make certain conclusions about the nature of the forbidden scattering based on the polarization selection rules.

The scattering from a(110) surface (measured using 5145 Å line of the Ar laser) has been reported by Tiong et al[25]. They attributed the observed spectra to morphic

effects[79,80] -i.e. the surface field induced (SF) scattering and the linear-$\vec{q}$ dependent (LQ) effects. They noted, however, that a discrepancy excisted between the polarization selection rules for the (SF) and (LQ) spectra and the ones observed experimentally. The workers of Ref.25 have found that for the set of axes x_2', y_2', z_2' (defined in Eq.(65)) for configurations with parallel directions of incident and scattered polarizations, the scattering cross section is large; whereas, for the polarization directions perpendicular to one another, the cross section is almost zero. Nevertheless, the polarization selection rules for morphic effects scattering allows the scattering for all combinations of polarizations in the x_2', y_2', z_2' axes[79,80]. They were forced to conclude that the scattering cross section was small in the crossed polarization configuration because the corresponding polarizability derivatives occasionally turned out to be small.

We feel that a more likely mechanism of the forbidden LO- scattering is either the intraband Frölich interaction (which adds a diagonal tensor to the crystal polarizability) or the impurity- induced mechanism (which, also, has the diagonal Raman tensor). For such a tensor, the crossed polarization configuration scattering is forbidden in any set of axes. To check the

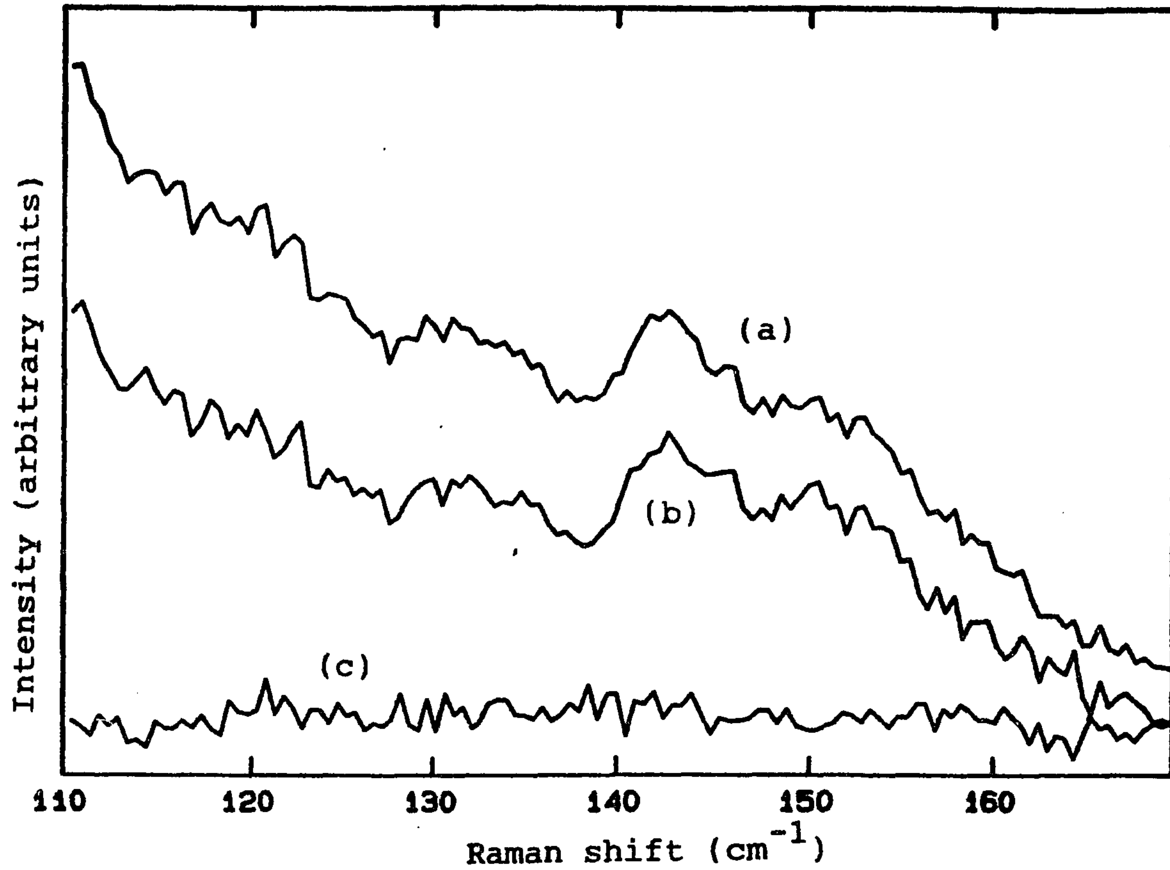

Fig.35

Polarization selection rules study on $Hg_{1-x}Cd_xTe$ x=0.3 sample.
Spectra taken at 77K. The axes denoted as in Eq.(65).
(a)- $z_2(x_2',x_2')\bar{z}_2$
(b)- $z_2(y_2',y_2')\bar{z}_2$
(c)- $z_2(x_2',y_2')\bar{z}_2$

Tiong et al's[25] hypotesis that the tensor components are occasionally small,we repeated the polarization selection rules measurement for the same set of axes on a sample with different composition (x=0.3). The measured spectra are shown in Fig.35. The crossed-polarization configuration is forbidden for x=0.3 samples too. Therefore, it is unlikely that the correspondent polarizability components are accidentally small.

The comparative study of the intraband Frölich interaction and impurity induced scattering[84] showed that the intraband Frölich interaction mechanism is important only in extremely pure crystals. Investigation of the Cd rich $Hg_{1-x}Cd_xTe$[91] also showed that the forbidden LO scattering is caused by impurity induced scattering. The difference in resonance energies (≅10 meV) is much smaller than the bandwidth of the E_1 transition (it equals 145 meV for the x=0.3 sample at 77K). Therefore, in our case, the resonance energy could not be used to distinguish which of the two mechanisms was responsible for the forbidden scattering. However,we may have evidence favoring impurity induced scattering in our case. The low energy shoulder of the $158cm^{-1}$ feature may be caused by the fact that in the case of impurity induced scattering the wave vector conservation is relaxed. The phonons with wave vector q values as big

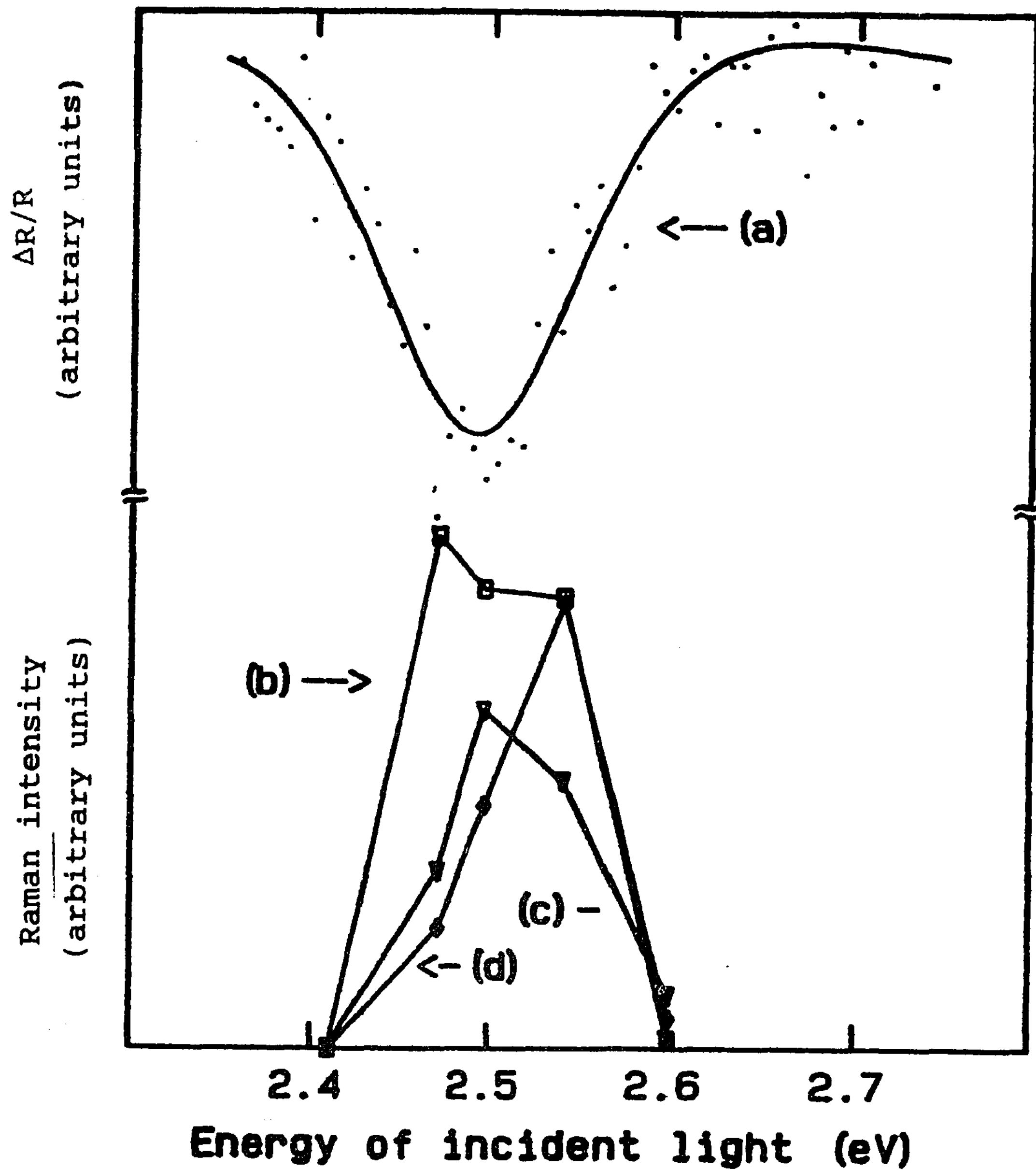

Fig.36

Comparison of PR and RRS results for $Hg_{1-x}Cd_xTe$ x=0.3 sample at 77K.
(a)- PR spectrum: experimental results are shown by points and the least square fit to Eq.(25) is shown by the solid line. The fit yields E_1=2.49 eV, Γ= 146 meV.

(b)- Clustering mode intensity
(c)- "HgTe- like" LO mode intensity
(d)- "CdTe- like"LO+TO mode intensity

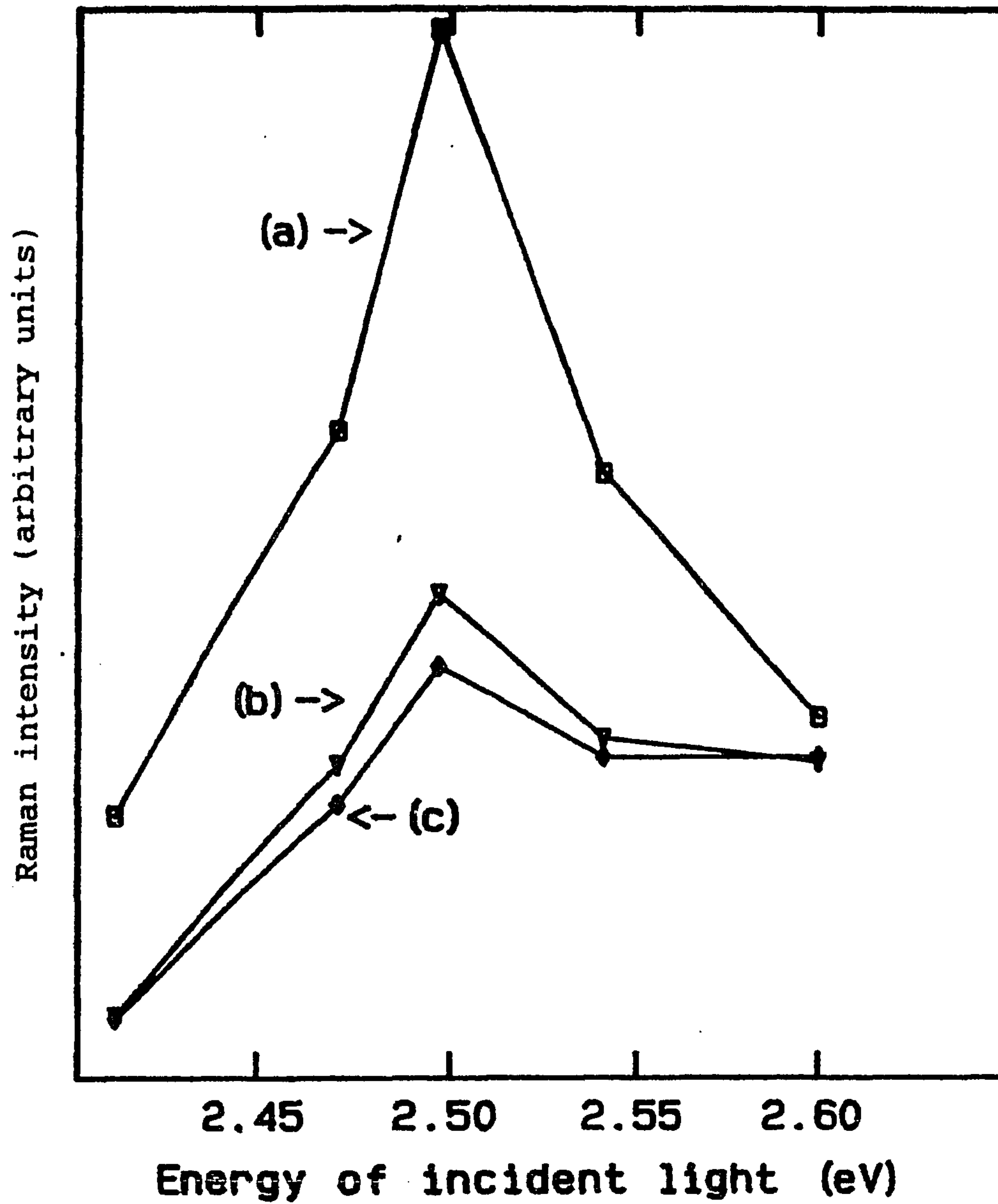

Fig.37

RRS results for $Hg_{1-x}Cd_xTe$ x=0.3 at 10K.

(a)- Clustering mode intensity
(b)- "HgTe- like" LO mode intensity
(c)- "CdTe- like"LO+TO mode intensity

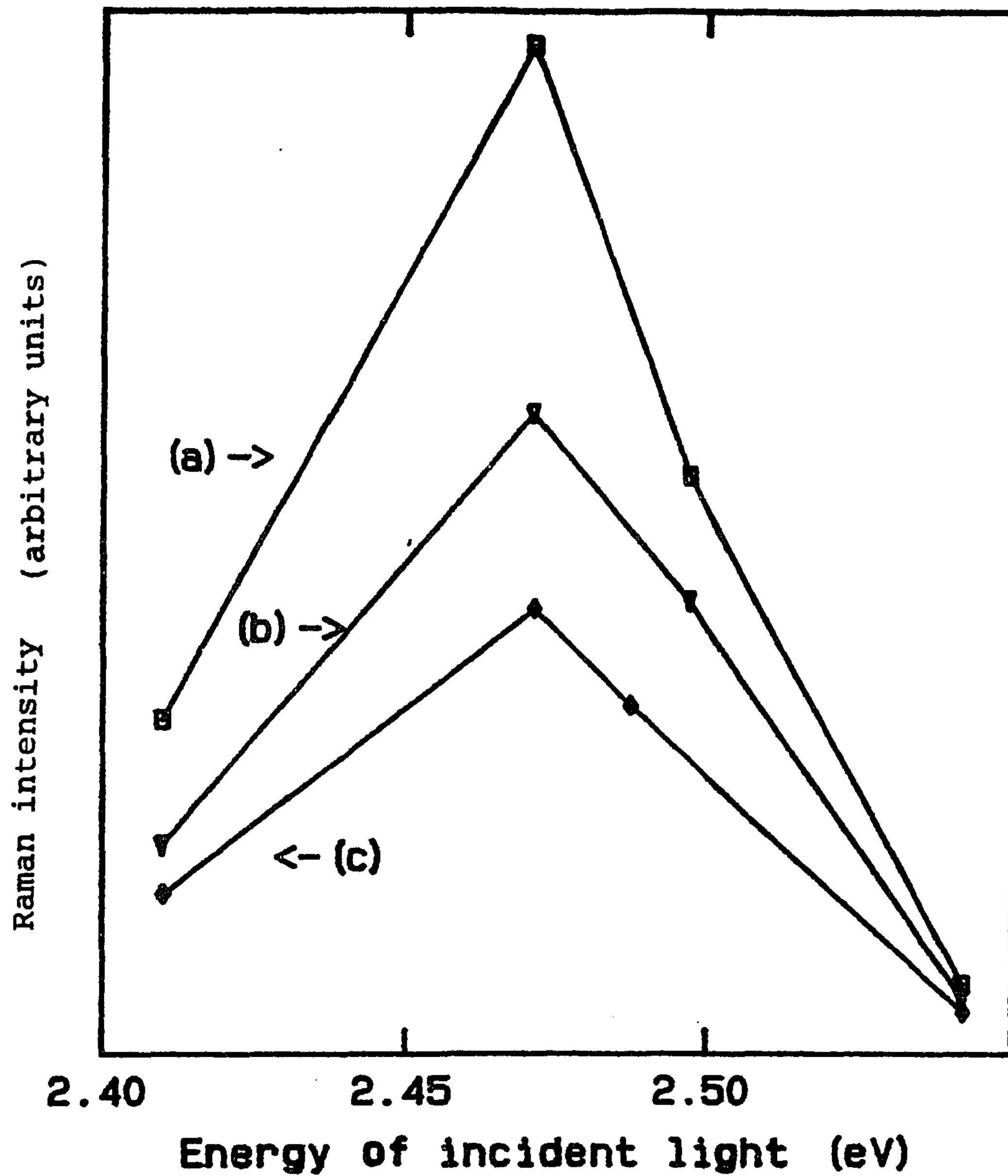

Fig.38

RRS results for $Hg_{1-x}Cd_xTe$ x=0.2 at 10K.

(a)- Clustering mode intensity
(b)- "HgTe- like" LO mode intensity
(c)- "CdTe- like"LO+TO mode intensity

as 20% of q_{max} (wave vector at the Brilluoin zone edge) participate in Raman scattering[84].

Since $q \neq 0$ LO phonons have lower energy than the ones at the zone center, this type of q- conservation relaxation may lead to the appearance of a signal on the low energy side of the $\vec{q}=0$ Raman peaks[90,92]. We do not consider this conclusive evidence since there are other possible explanations for this occurrence. For instance, we may be seeing the "clustering modes" reported in Ref.30. We also noted that this low energy shoulder was not present on the near- resonance spectra taken from the (110) surface of $Hg_{0.8}Cd_{0.2}Te$ by Tiong et al[25].

B. The Propagating nature of the "CdTe- like LO+TO" Mode

We have plotted the dependence of the Raman intensity normalized to the reference CaF_2 signal for LO peaks and the clustering peak vs. the incident light energy in Figs.36-38. For the x=0.3 sample we have also taken the photoreflectance spectrum at 77K (see Fig.16) in order that the observed RRS spectrum could be compared to the results of the direct measurement of the electronic E_1 transition (see Table IV). It is clear that all three peaks have resonances around the same energy. From the Fig.37 and Table IV, it is also clear that this energy is close to the E_1 transition energy.

The fact that both "HgTe- like" LO and "CdTe-like" LO+TO modes resonate at the energy of the E_1 transition of $Hg_{1-x}Cd_xTe$ provides a very important insight into the nature of the "CdTe- like" LO+TO mode. We have already mentioned that LO and TO "CdTe- like" modes should extrapolate to the energy of vibrational mode of the single substitutional Cd atom in HgTe when x is small. As seen in Fig.29. these modes are quite close to one another in energy for x=0.2 and x=0.3. Raman spectra display only one feature in this energy region (see Fig 4). By using the Raman selection rules, this feature has been shown to have mainly LO character for the samples with x=0.2[25,29,70]. An interesting question arises: are we dealing with propagating "CdTe- like" LO and TO phonons belonging to the "average" crystal; or, is this an impurity mode belonging to Cd in HgTe? In view of a rather dramatic result obtained by Bedel et al[88], this is not a trivial question. For $InAs_{0.8}P_{0.2}$ a similar "InP- like" mode was found to be a localized impurity mode. We shall follow the method of analysis used by this group and apply it to our results.

It has been shown[93,94] that substitutional impurities can generate Raman active vibrational modes which can either be localized in the vicinity of the defect (localized modes) or can propagate through the crystal (in-band modes). The impurity modes can

propagate through the crystal when, they fall into the energy range of the allowed vibrations of the host crystal.

The resonant Raman scattering experiments performed on the doped crystals[93,94] confirmed that the in-band modes are resonantly enhanced, when the incident light energy is near the energy of the host crystal electronic transitions. In contrast, the localized modes are coupled to the electronic levels of the impurity and are enhanced when the incident light approaches the enegry of the electronic transitions associated with the impurity. In the case of the P impurity in InAs, the impurity vibrational mode must be localized, since it does not fall within the allowed vibrational energy range of the InAs. The "InP- like" peak, observed in $InAs_{0.8}P_{0.2}$, resonated at the energy of incident light close to the InP E_1 gap; whereas, "InAs- like" LO phonon had a resonance at the energy of the E_1 transition in $InAs_{0.8}P_{0.2}$. Therefore, it was inferred that the "InP-like" mode was a localized mode of the P impurity in InAs and, as a result, coupled to a local part of the electronic wave function close to the P atom.

The case of the Cd substitutional impurity in HgTe is similar to the P impurity in InAs to the extent that the impurity vibrational mode must be localized. The Cd impurity vibrational mode does not fall into the

allowed energy range as can be seen from the compositional dependence of the phonon energy (see Fig.29). Therefore, if the "CdTe- like" peak was due to an impurity mode, it would have resonant enhancement at the energies close to E_1 transition of CdTe rather than at the energy of $Hg_{1-x}Cd_xTe$ E_1 transition. Thus, we conclude that the "CdTe- like" feature is actually due to the LO and TO phonons belonging to the crystal rather than an impurity mode.

In conclusion, we have investigated the mechanism of the symmetry forbidden LO-scattering near the E_1 electronic transition energy on two $Hg_{1-x}Cd_xTe$ samples with composition x=0.3 and 0.2. The symmetry selection rules favor two mechanisms: the intraband Frölich interaction and the impurity- induced mechanism introduced by Gogolin and Rashba. We have found evidence in favor of the impurity- induced mechanism.

We have also investigated the resonance energies of RRS in the same samples. The "CdTe-like" LO+TO mode has a resonance at the energy of the E_1 electronic transition as do the "HgTe-like" LO and "clustering modes". This identifies the "CdTe-like" LO+TO mode as the propagating phonon rather than the Cd impurity-localized mode in HgTe.

Chapter V

Light Induced Charging of $Hg_{1-x}Cd_xTe/SiO_2$ Interface.

Passivation of $Hg_{1-x}Cd_xTe$ by the deposition of a foreign insulator such as SiO_2-Photox™ has become technologically important principally due to its chemical inertness coupled with the resultant high quality interfaces[60]. The Photox™ process is a modification of the chemical vapor deposition technique of obtaining SiO_2 layers[49].

It is important to have information about interface traps since they can limit the carrier lifetimes in junction devices or, when charged, alter the effective gate bias of metal-insulator-semiconductor (MIS) devices. The $Hg_{1-x}Cd_xTe$ interface in the MIS configuration has been studied in the frequency range $1-10^7$Hz[95-98]. Work in the $1-10^3$Hz region on the $Hg_{1-x}Cd_xTe/SiO_2$-Photox™ interface[98] revealed a considerable number of interface traps ($>10^{13} cm^{-2} eV^{-1}$). Illumination effects in the very low frequency domain ($\cong 10^{-5}$Hz) on $Hg_{1-x}Cd_xTe$ MIS devices fabricated with a native oxide indicated a total trap density in the oxide

as high as $6 \cdot 10^{13}$ cm^{-2} [99].

In order to gain further information about the states at or near the $Hg_{1-x}Cd_xTe/SiO_2$-Photox^{TM} interface we have investigated the influence of illumination (with and without gate bias) in the wavelength (λ) range 0.22-1.0 μm on the C-V characteristics of an MIS device at 77 K.

5.1 Theory of Capacitance- Voltage Measurements

We shall briefly review the theory of C-V measurements and their use for evaluation of the density of the charged traps in the insulator. Let us consider the band diagram of the unbiased ideal MIS device. This device is realized when the difference between the metal and semiconductor workfunction (ϕ_{ms}) is zero (see Fig.39):

$$\phi_{ms} = \phi_m + (\chi + \frac{E}{2e} - \phi_b) = 0 \qquad (77)$$

where χ is the semiconductor electron affinity, ϕ_b is the potential barrier between the metal and the insulator and ϕ_m is the metal work function.

In this ideal device, the bands of the semiconductor are flat when there is no bias on the metal electrode. Consider the MIS device based on the n-type semiconductor. Biasing this ideal device will lead to the following changes (see Fig.40):

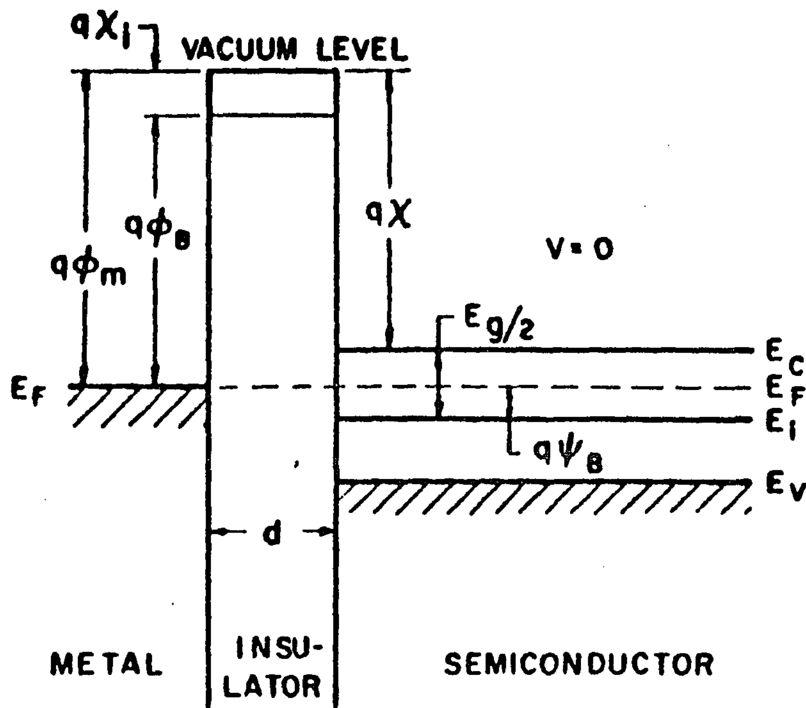

Fig.39

Band diagram of the ideal unbiased MIS device (n- type semiconductor); after Ref. 100.

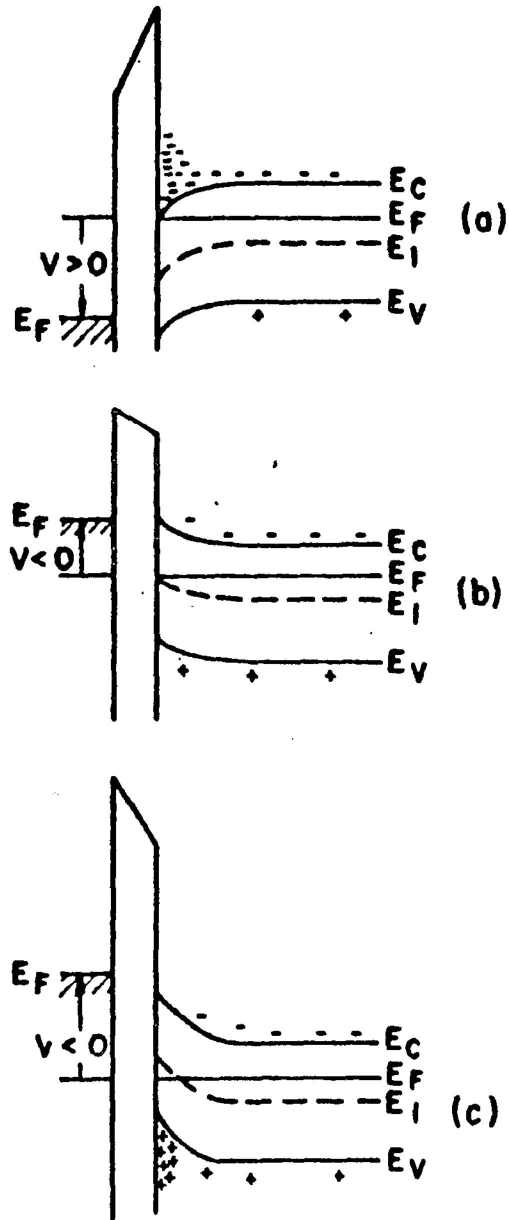

Fig.40

Band diagram of the ideal MIS device under bias (n- type semiconductor); after Ref. 100.

a. Negative bias will cause depletion of the electrons from the surface (i.e., create the depletion layer).

b. Application of a slight positive bias will lead to an accumulation region at the surface of the semiconductor.

c. Increasing the negative bias will lead to the inversion of the conductivity type near the surface of the semiconductor (create inversion layer).

The capacitance of the MIS device (C) can be viewed as a result of the series connection of the capacitance of the insulator (C_i) and the capacitance of the depletion- inversion region (C_d)[100,109]:

$$C = \frac{C_i C_d}{C_i + C_d} \tag{78}$$

Thus, one can explain qualitatively the shape of a typical capacitance-voltage (C-V) curve (see Fig.41). We shall consider only the low frequency case pertaining to our work. In this case, the frequency of the probe voltage is lower than the characteristic frequencies of the generation-recombination processes that determines the hole concentration. Large positive or negative bias creates a highly conductive layer of electrons or holes (deep accumulation or depletion) at the surface and (in low frequency regime[100]) effectively eliminates C_d from the equivalent circuit. Then we have

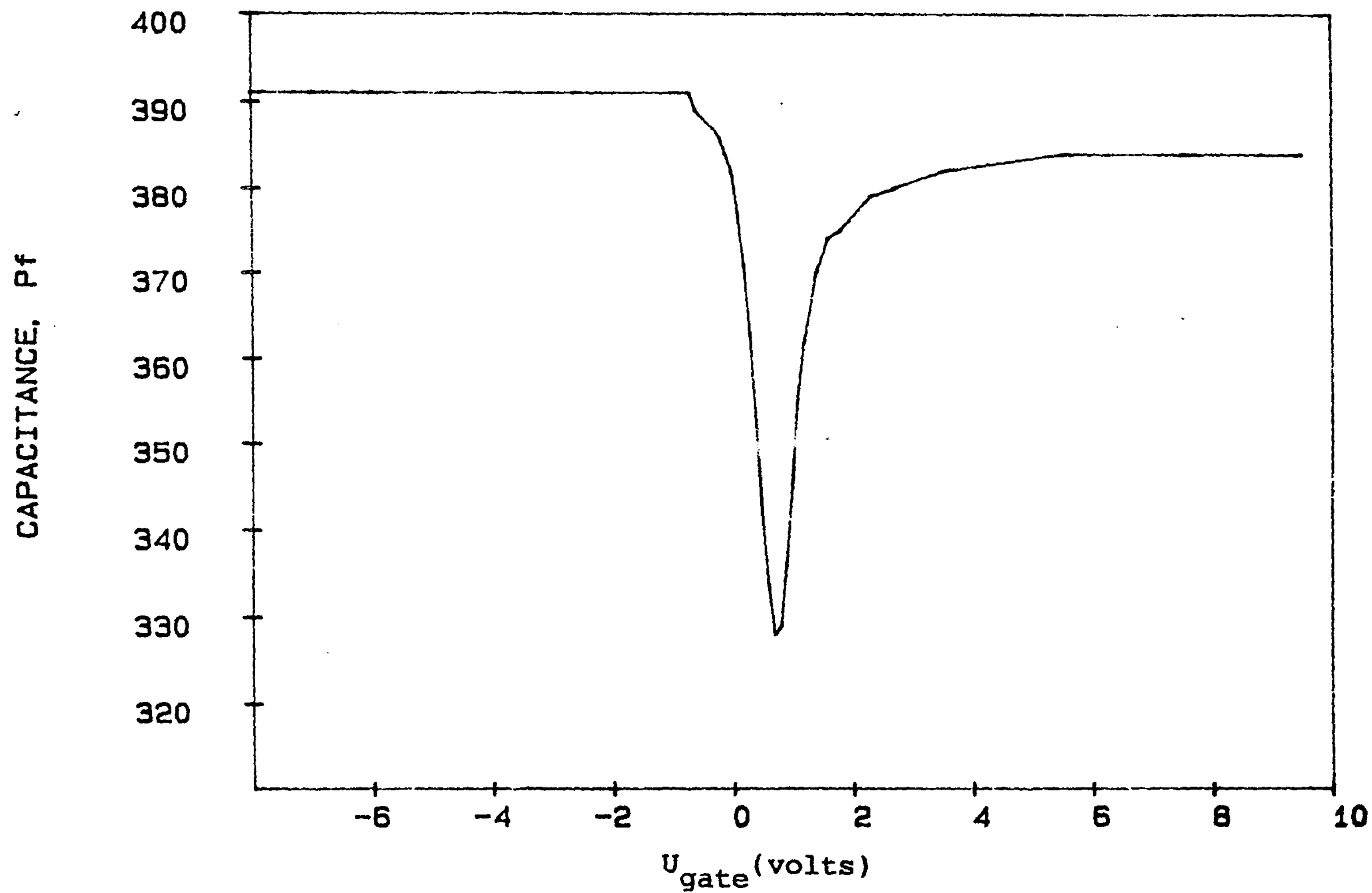

Fig.41

The result of manual CV measurement of the MIS sample unexposed to light.

$$C=C_i. \quad (79)$$

For biases between these two extreme cases, we have

$$C < C_i \quad (80)$$

according to Eq.(80) since the depletion region has a finite capacitance. This explains a V- like shape of the C-V curve in Fig.41.

As we noted earlier, the ideal MIS device is under the flat- band condition when there is no bias. There are reasons for which the real devices display a different type of behavior[100,101]. For instance, the presence of a negative charge (Q) on the metal-insulator interface will lead to a shift of the C-V curve as a whole into the positive direction in the voltage by the amount of:

$$\Delta V = \frac{-Q}{C_i}. \quad (81)$$

If, in addition, there exists a non-zero work function difference between the metal and semiconductor, the shift of the C-V curve (which is the same as a flat-band voltage shift ΔV_{fb}) becomes

$$V_{fb} = \phi_{ms} - \frac{Q}{C_i}. \quad (82)$$

This result is important for our work. It relates the charge in the insulator to the shift of the C-V curve along the V- axis which can be observed experimentally.

To find the flat- band voltage from the experimental C-V curve, we used the analysis method proposed in Ref.102.

The measured capacitance C of the MIS device is given by

$$C = \frac{dQ_T}{dV} \tag{83}$$

where Q_T is the total charge on the metal electrode. The voltage applied to the device is divided in two parts: ψ_s, semiconductor surface band- bending and voltage on the insulator layer which can be written as $\frac{Q_T}{C_i}$.

Therefore we may write:

$$V = \psi_s + \frac{Q_T}{C_i} \tag{84}$$

Differentiating and using Eq.(85) we have:

$$\frac{d\psi_s}{dV} = 1 - \frac{1}{C_i} \cdot \frac{dQ_T}{dV} = 1 - \frac{C}{C_i} \tag{85}$$

so that the value of ψ_s can be obtained with accuracy to an additive constant Δ by integration (this quantity is denoted here as $\bar{\psi}_s$):

$$\psi_s(V_2) = \int_{V_1}^{V_2} (1 \frac{C}{C_i})dV + \Delta \equiv \bar{\psi}_s(V_2) + \Delta \tag{86}$$

The additive constant can be found by using the following approximate relationship valid in depletion regime far from flatband[102]

$$C_d^{-2} \propto (\psi_s - \frac{kT}{e}) \tag{87}$$

According to this relation, C_d^{-2} is linear in ψ_s and

$$\psi_s - \frac{kT}{e} \cong 0 \quad \text{when } C_d^{-2}=0 \qquad (88)$$

Therefore, plotting C_d^{-2} vs. $\bar{\psi}_s$ in the depletion region, one must find the linear dependence; the value of $\bar{\psi}_s$ at $C_d^{-2}=0$ will give the additive constant Δ. Now the function $\psi_s(V)$ is known and V_{fb} can be found as the value of voltage V for which $\psi_s=0$.

5.2 Experimental Details

We used two methods of measuring the C-V characteristics of the MIS device. The manual (point by point) measurements were done using the General Radio impedance bridge (model 1650-A). Use of the bridge permitted measurements of both active and reactive parts of the impedance. Thus we were able to explore equivalent circuits of the device more complicated than the simple one used to derive Eq.(78). As we said before, use of the simplest equivalent circuit yielded satisfactory results. Since this equivalent circuit contains only capacitors, one needs only the reactive part of the impedance. We found it possible to build a set-up which would scan bias voltages and record the C-V curves automatically. The automatic C-V set- up is shown schematically in Fig.42. The 1 kHz signal from the function generator (Hewlett- Packard model 3311A) was fed to the measurement loop through the transformer. The

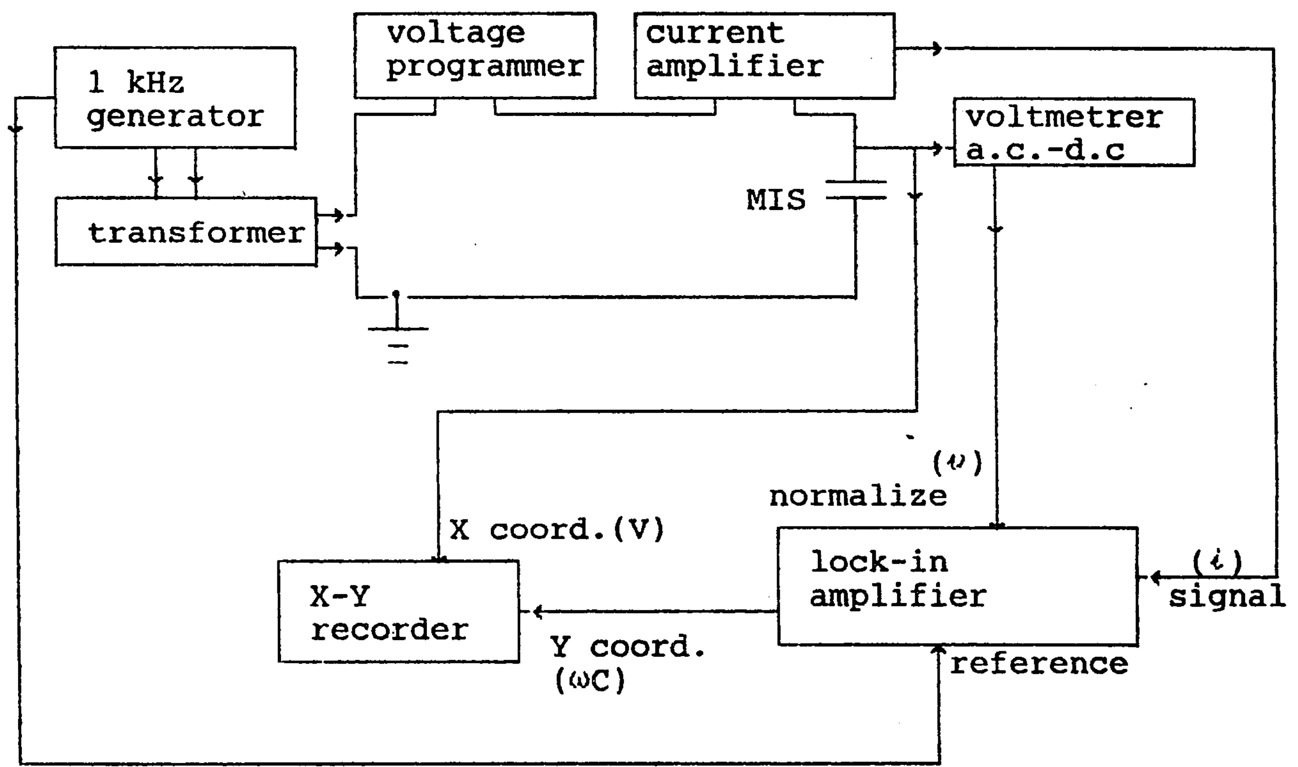

Fig.42

Setup for automated CV measurements.

secondary winding of the transformer supplied the probe voltage to the loop which consists of the following components:

- voltage programmer (EG&G model 175),
- current amplifier (we used electrometer Keithley model 610BR in current amplifier mode),
- the measured MIS device.

We took care that all the elements of this loop have a reactance much smaller than that of the MIS device measured. The output voltage of the current amplifier was proportional to the current through the MIS device. A voltmeter with high input impedance (voltmeter a.c.-d.c. on the diagram) was used to measure the a.c. voltage on the device and convert it into the d.c. signal.

The signals from the voltmeter and current amplifier were fed to normalization and signal input of the lock- in amplifier (Ithaco model 391A) correspondingly. The lock- in amplifier was tuned to the phase 90 degrees off compared to the reference voltage taken from the generator. Therefore, the output of the lock-in amplifier was proportional to the ratio of the component of current that is 90 degrees off the voltage (i) to the voltage (v). This ratio is reciprocal of the reactance of the MIS device reactance X_c since all reactances in the loop are small in comparison to the

reactance of the MIS device. Thus the signal was proportional to the device capacitance:

$$1/X_c = \omega C = \frac{i}{v} \qquad (89)$$

where ω is the frequency of the probe voltage. This signal was recorded as a function of d.c. bias voltage by the X-Y recorder while the bias voltage was scanned by the voltage programmer. The Y- scale of the recorder was calibrated using a known capacitor in place of the MIS device before performing the actual measurement.

All light-induced studies were carried out at 77K. To provide illumination we used light from a Xenon lamp passed through a 0.3 meter grating monochromator (GCA/McPherson model 218). In order to find the photon flux (at wavelength λ) the power of the monochromatic light was first measured at 5100A with a light power meter (International Light Power meter model 1L510) and then the calibration was extended to shorter wavelengths using a Si photodiode (EG&G model 4000B) with a known spectral response curve. The charging of the $Hg_{0.3}Cd_{0.7}Te/SiO_2$-Photox[TM] interface was determined by C-V measurements at a frequency of 1 kHz, the amplitude of the ac probe voltage at the gate being 50mV.

5.3 Experimental Results

A. Light Illumination at Zero Bias Voltage

The sample (in the open circuit configuration)

was first illuminated by light at λ from the monochromator for a given amount of time (t). The C-V measurements were then taken in the dark. After this procedure a new illumination period was started.

From the C-V measurement we have established that if the sample was kept at 77K in the dark after the above illumination procedure, the light-induced charge remained unchanged for at least 8 hours. This demonstrates that the trap mechanism is very slow with a characteristic frequency < 10^{-5} sec^{-1}. Thus after every new illumination period we have actually measured the cumulative effect of all preceding illumination periods. After U_{fb} reached a value of 20 V (or at the end of the day, whichever came first) the sample was heated to 300K which restored it to the initial, uncharged state. This was checked by cooling the sample down to 77K and taking C-V measurements after the 30 minute heating procedure.

In Fig.43 we present a typical set of C-V curves from our sample after illumination by 2800A light for different periods of time. The shift of the flatband voltage with illumination is apparent. To make our observations quantitative, the C-V curves of the device were measured in dark manually (see Fig.41) and the flatband voltage was determined using the procedure described above. The value of the capacitance at the flat-band voltage was 375 pF. Therefore we set the value

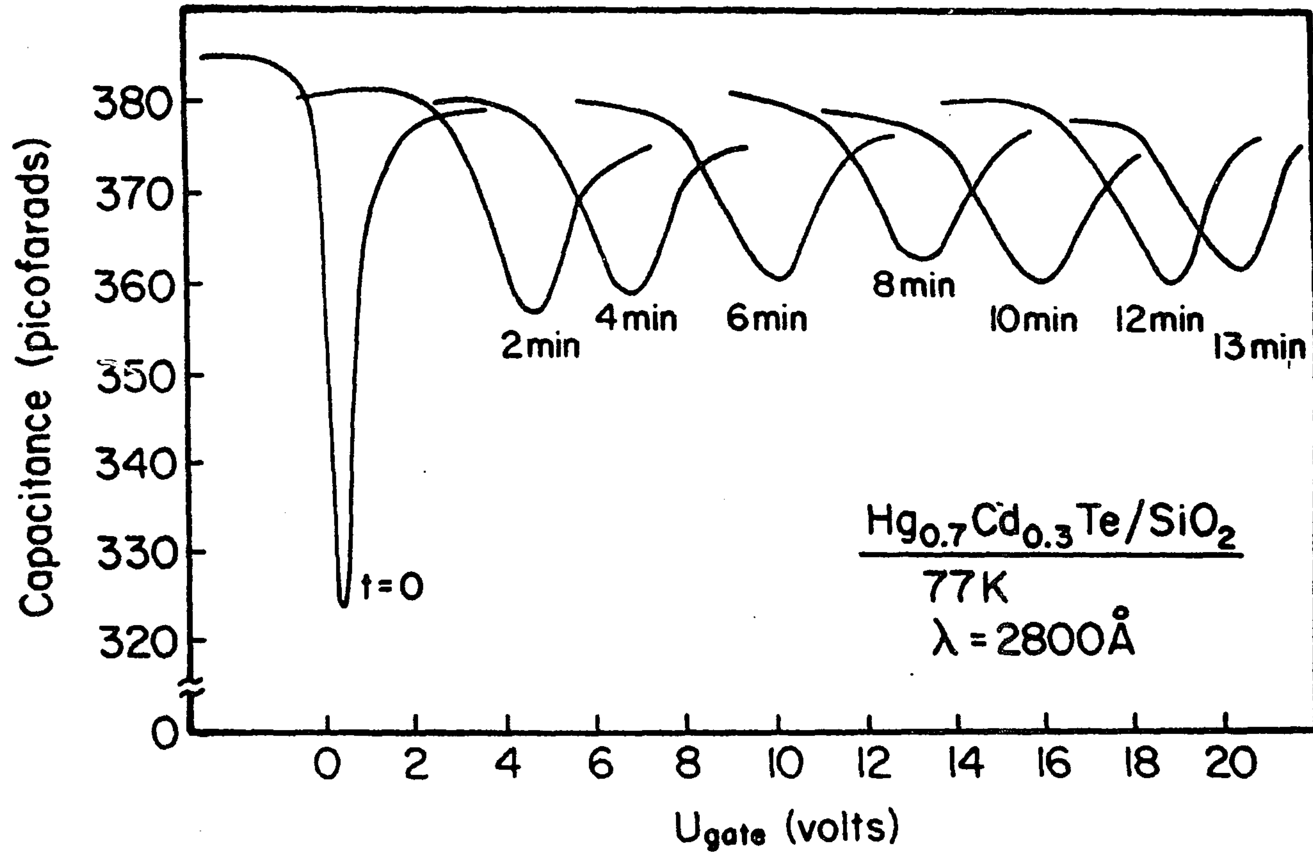

Fig.43

Results of CV measurements after exposure to 2800 Å light at zero bias.

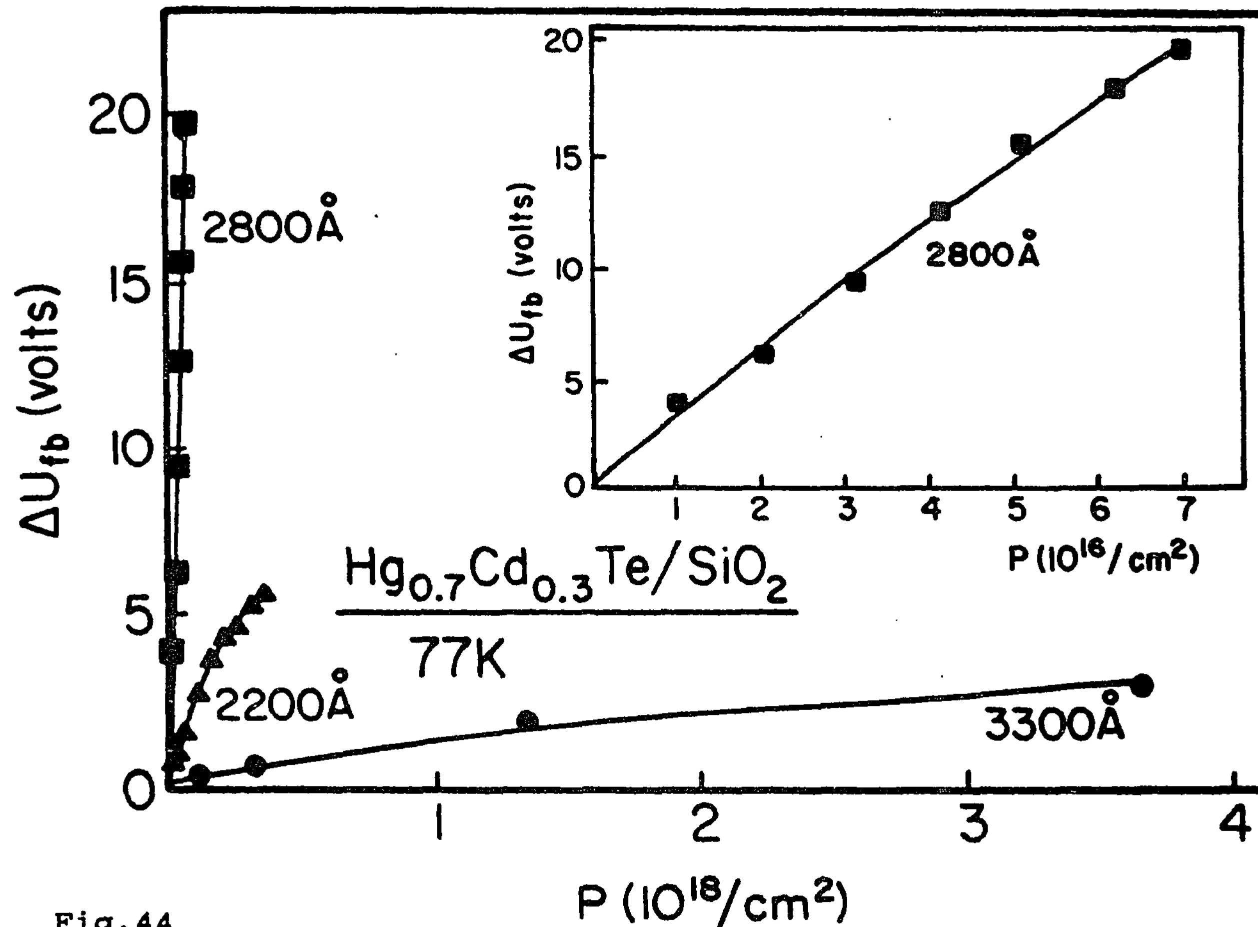

Fig.44

Photo- induced flatband shift ΔU_{fb} as a function of the total number of photons per cm^2, P, for illumination with wavelengths 3300, 2800 and 2200 Å. The inset is an expanded version of the 2800 Å results.

of U_{fb} in each measurement to be the voltage corresponding to a capacitance of 375 pF. Plotted in Fig.44 is the light-induced flatband shift, U_{fb}, as a function of the total number of incident photons per unit area, $P(h\nu)$, for three different wavelengths. The inset shows an expanded version of the 2800A data. Note that for all three wave-lengths U_{fb} tends to saturate as P increases. The saturation level for U_{fb} peaks at $\lambda \cong$ 2800A while for $\lambda \geq$ 5100A we have found no significant light-induced charging.

B. Light Illumination with Gate Bias

Application of a negative bias to the gate produced no appreciable change in the charging picture described above. However, the application of a positive bias made it possible to charge the system by utilizing $\lambda \geq$ 5100A. The result of illuminating the structure by $\lambda = 1\mu m$ light is presented in Fig.45. Curve (1) is the C-V measurement with no light exposure and no bias; this curve is the same as the t=0 data of Fig.41. The C-V results after exposure to 1 μm light for one hour and a gate bias of +10 V is shown in curve (2). The light and the dc bias were then shut off and the C-V evaluated after 10 minutes in the dark as displayed in curve (3). The results of Fig.45 indicate that 1 hour of illumination under +10 V bias has increased U_{fb} from

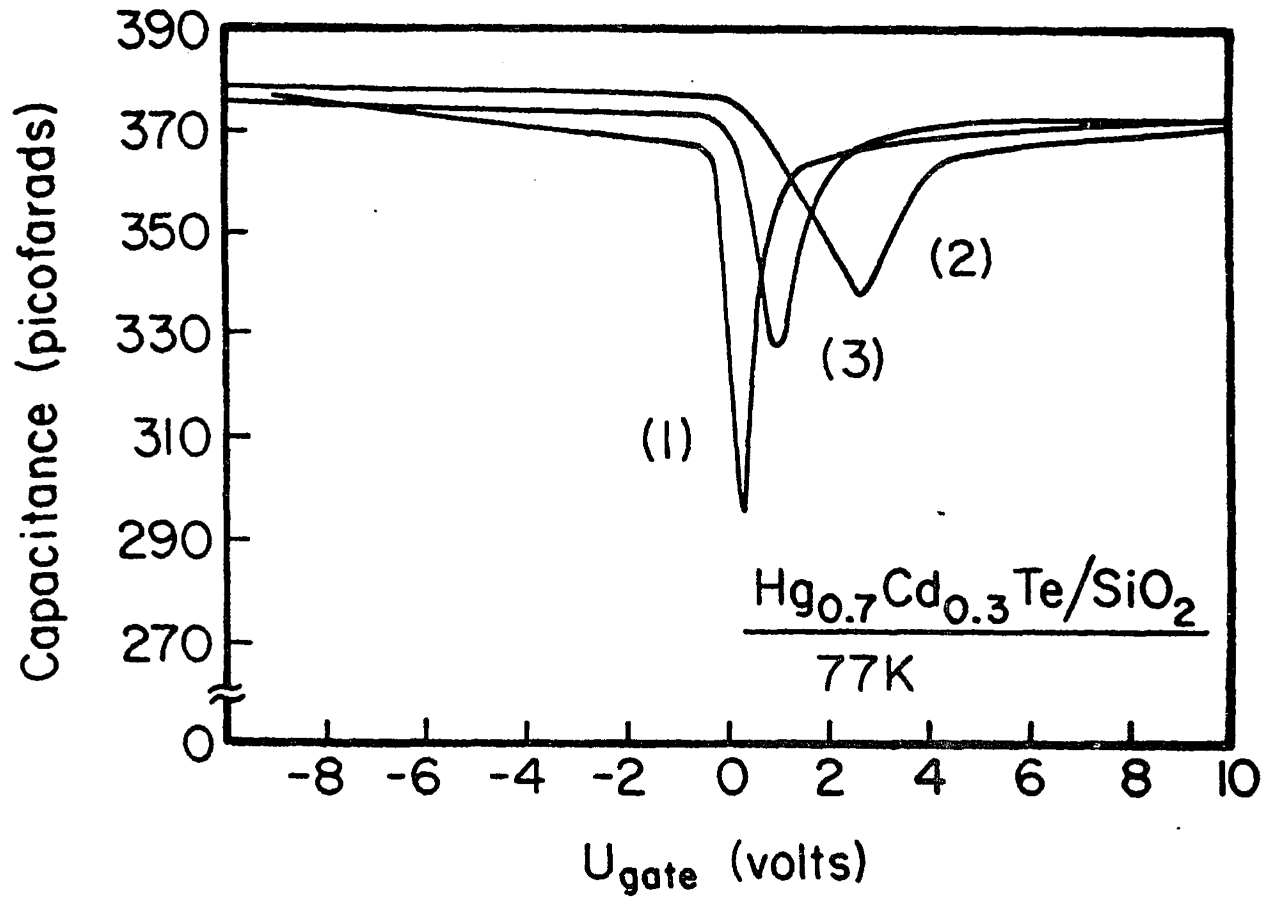

Fig.45

CV curves at 77K taken after 1μm light exposure with +10 V bias.
CV curves at 77K for (1) no light exposure, (2) after exposure to 1μm light for 1 h under +10 V bias and (3) after the light and bias were shut off.

approximately 1 V to 4 V. Figure 45 shows that the charge leaks off relatively quickly since after only 10 minutes of relaxation at 77K in the dark U_{fb} was reduced to about 2 V from 4 V. This is in sharp contrast with the case of charging by illumination only and suggests a different charging mechanism when bias is applied.

5.4 Discussion

A. Charging by Light Illumination with Zero Bias Voltage

The results of Figs.43 and 44 can be explained by the presence of very slow electron traps at or near the $Hg_{0.7}Cd_{0.3}Te/SiO_2$-Photox™ interface. The fact that the photo-induced flatband shift has a maximum for $\lambda \cong$ 2800A suggests that two mechanisms are operative; i.e., both charging and discharging. For 2800A $\leq \lambda \leq$ 5100A the light creates only a charging effect while for $\lambda \leq$ 2800A both charging and discharging occur. In addition, there is a distribution of trap states so that as the photon energy increases (up to a certain point) the number of traps accessed by the charging mechanism also increases, which explains why the 2800A light creates a greater U_{fb} than say 3300A. With further increase of the photon energy the discharging mechanism also comes into play and

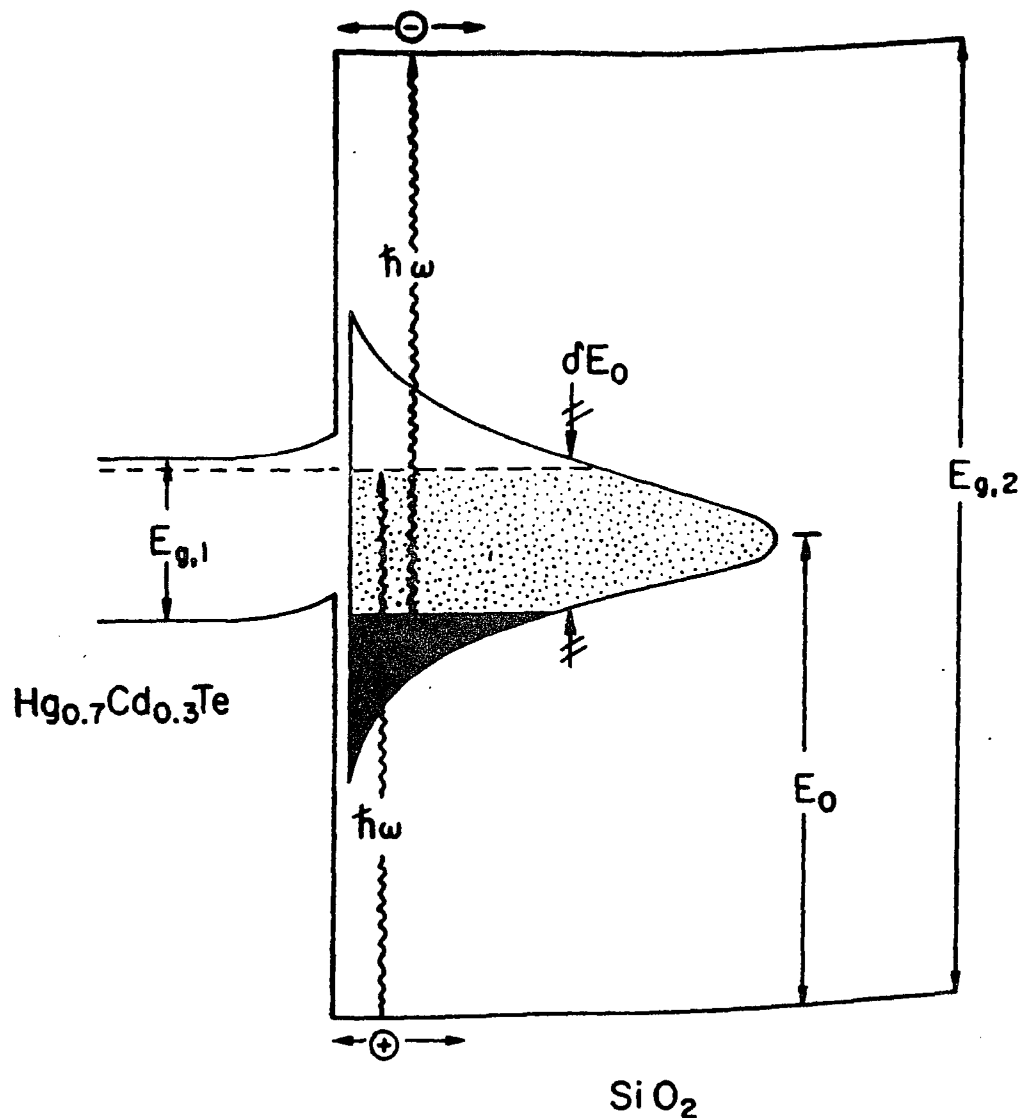

Fig.46

Proposed model for the $Hg_{1-x}Cd_xTe$ (n-type)/SiO_2- Pxotox[TM] interface. The distribution of the electron traps in SiO_2 is centered around E_0 with full width at half maximum δE_0. For clarity the energy gaps of $Hg_{1-x}Cd_xTe$ and SiO_2 are not drawn to scale. The dark area represents the states per unit area acessed by chrging only process while the shaded region indicates the region of charging and discharging.

causes the 2200A light to be less effective.

The above mechanisms are illustrated in further detail in Fig.46. In this figure we display schematically the interfacial region of the $Hg_{0.7}Cd_{0.3}Te/SiO_2$-Photox^{TM} system. The energy gaps of the two materials are denoted as $E_{g,1}$ ($Hg_{0.7}Cd_{0.3}Te$) and $E_{g,2}$ (SiO_2). The zero of energy is taken to be the top of the SiO_2 valence band. The electron traps are distributed continuously with distribution $D_t(E)$ around energy E_0 with full-width at half-maximum of δE_0. The n-type $Hg_{0.7}Cd_{0.3}Te$ is slightly depleted as indicated by the positive value of U_{fb} in the dark (t=0 curve in Fig.43). For the sake of clarity the band gaps of the $Hg_{0.7}Cd_{0.3}Te$ ($\cong$ 250 meV) and the SiO_2 (9 eV) are not drawn to scale.

As shown in the figure two processes can occur:

(1) Charging - An electron can be photo-excited from the SiO_2 valence band into a trap state, some of the resultant holes moving into the $Hg_{0.7}Cd_{0.3}Te$ region. This process can take place for photon energies ($h\nu$) less than or equal to $E_{g,2}$. We denote the quantum efficiency of this process as Q_1.

(2) Discharging - For photon energies greater than $E_{g,2}/2$ not only does charging take place as discussed above but, in addition, electrons in the trap states can be photo-excited into the conduction band of

the SiO_2. Some of these electrons can be transferred into the conduction band of the $Hg_{0.7}Cd_{0.3}Te$. The quantum efficiency of this effect is denoted as Q_2.

Note, that in order for process (1) to cause charging, the photoexcited hole must move into the $Hg_{0.7}Cd_{0.3}Te$ against the action of electric field whereas in process (2) the excited electron which produces discharging is pulled towards the $Hg_{0.7}Cd_{0.3}Te$ by the electric field. Thus we expect process (2) to have a higher probability than process (1), i.e. $Q_2 >> Q_1$.

We denote as N_1 the number of states per unit area available to mechanism (1) but not mechanism (2) and as $N_{1,2}$ the number of states available to both (1) and (2). We can write:

$$N_1(h\omega) = \begin{cases} \int_0^{h\omega} D_1(E)dE \ , \ h\omega < E_{g,2}/2 & (90a) \\ \int_0^{E_{g,2}-h\omega} D_1(E)dE \ , \ h\omega > E_{g,2}/2 & (90b) \end{cases}$$

$$N_{1,2}(\omega) = \begin{cases} 0 \ , h\omega < E_{g,2}/2 & (91a) \\ \int_{E_{g,2}-h\omega}^{0} D_1(E)dE, h\omega > E_{g,2}/2 & (91b) \end{cases}$$

In Fig.46 the dark region corresponds to N_1 while the

shaded region represents $N_{1,2}$ In order to develop our model more fully we define the following quantities:

$n_1(n_{1,2})$ = number of traps per unit area filled in the $N_1(N_{1,2})$ part of the trap distribution;

n = total number of filled traps per unit area.

Therefore, for process (1) we can write:

$$dn_1/dt = Q_1(P/t)\ (N_1 - n_1) \tag{92}$$

while for process (1) and (2):

$$dn_{1,2}/dt = Q_1(P/t)\cdot(N_{1,2} - n_{1,2}) - Q_2(P/t)n_{1,2} \tag{93}$$

The solutions to Eqs. (94) and (95) can be written as:

$$n_1(P) = N_1[1-\exp(-Q_1P)] \tag{94}$$

$$n_{1,2}(P) = \frac{N_{1,2}Q_1}{Q_1+Q_2}\cdot\left\{1-\exp[-(Q_1+Q_2)P]\right\} \tag{95}$$

and

$$n[P(\hbar\omega)] = n_1[P(\hbar\omega)] + n_{1,2}[P(\hbar\omega)] \tag{96}$$

Equations (96), (97) and (98) show that $n[P(\hbar\omega)3]$ saturates as $P\to\infty$. We denote the saturation value of $n[P(\hbar\omega)]$ as $n_s(\hbar\omega)$, such that from Eqs. (94), (95) and (96):

$$n_s(\hbar\omega) = N_1(\hbar\omega) + [N_{1,2}(\hbar\omega)Q_1'/(Q_1 + Q_2)] \tag{97}$$

It is also convenient to express $n[P(\hbar\omega)]$ in terms of $n_s(\hbar\omega)$ as follows:

$$n[P(\hbar\omega)] = n_s[1-\exp(-Q_1P)] + \frac{N_{1,2}Q_1}{Q_1 + Q_2} \times\left\{\exp(-Q_1P) - \exp[-(Q_1+Q_2)P\right\} \tag{98}$$

Comparison can thus be made between the experimental results of Fig.44 and our model. Assuming for simplicity that the charging takes place near the insulator/semiconductor interface, using Eq.(82) the photo-induced flatband shift, ΔU_{fb}, can be related to the number of photo-filled traps $n[P(\hbar\omega)]$by the relation

$$\Delta U_{fb}[P(\hbar\omega)] = |e|\cdot n\cdot[P(\hbar\omega)]/C_i \qquad (99)$$

Thus U_{fb} can be used as a direct measure of the number of filled traps, n. From Eqs. (93)-(95) and (99) the dependence of U_{fb} on $P(\hbar\omega)$ can be fit using as adjustable parameters N_1, $N_{1,2}$, Q_1 and Q_2. Shown by the solid lines in Fig.44 is a least-squares fit of the experimental data to these equations for the three different wave-lengths.

The quantities N_1, $N_{1,2}$, Q_1, and Q_2 obtained by the above fitting procedure have a fairly large standard deviation. However, the parameter $n_s(\hbar\omega)$ can be obtained with a high degree of reliability using Eqs. (96) and (97). Shown in Fig.47 by the open circles is $n_s(\hbar\omega)$ determined from experiment as a function of $\hbar\omega$. Note that there is a pronounced peak at about 4.7 eV and that $n_s(\hbar\omega) \cong 0$ for $\hbar\omega \le 2.4$ eV.

The photon energy dependence of $n(\hbar\omega)$ can be accounted for on the basis of the model in Fig.46 and Eq.(97). From the above considerations (least- squares fit in Fig.44) we find that $Q_2 \cong 10\ Q_1$ and hence for our

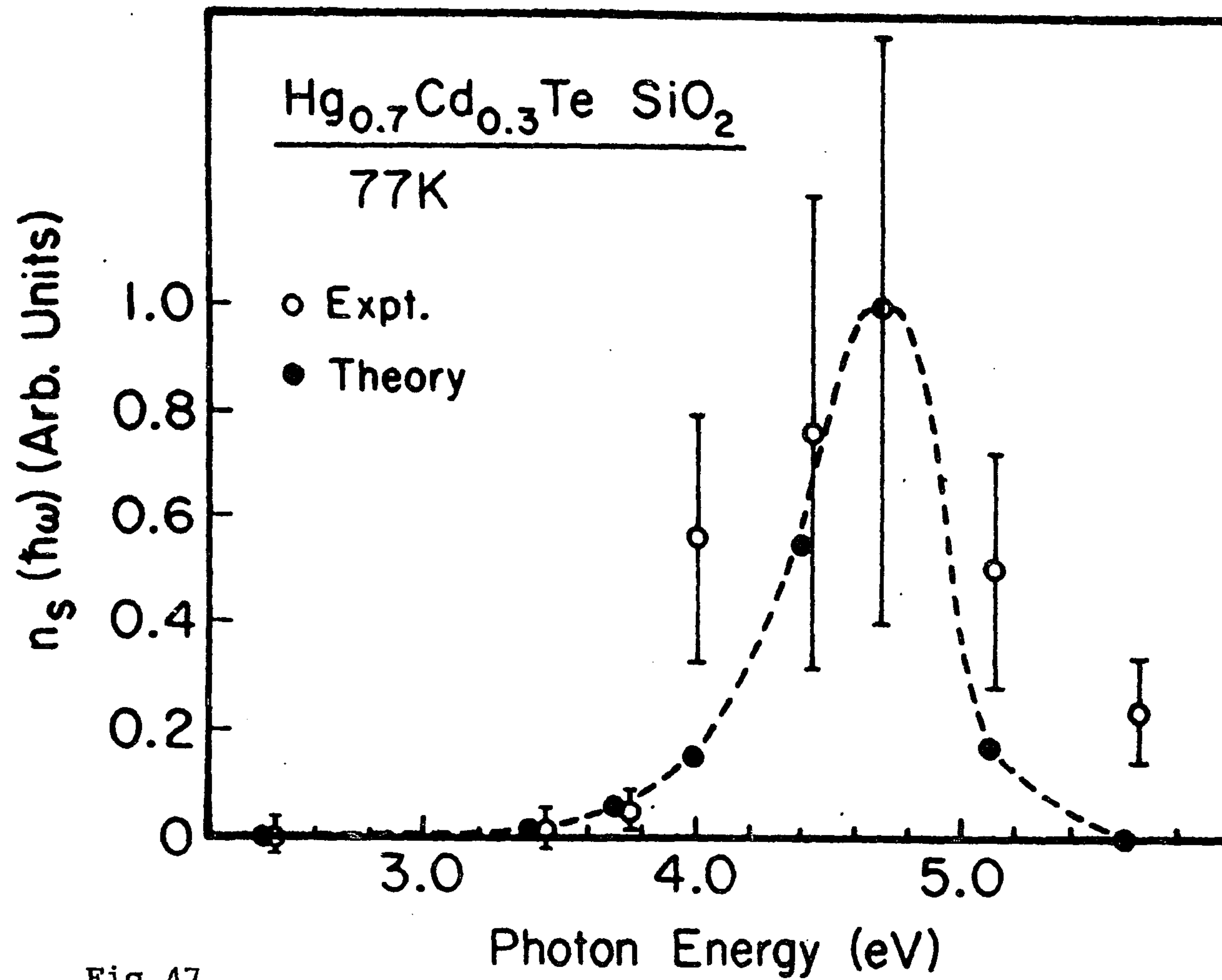

Fig.47

Experimental (open circles) and theoretical (closed circles) values of $n_s(h\omega)$

case Eq.(97) becomes:

$$n_s(\hbar\omega) \cong N_1(\hbar\omega) + \frac{1}{10}N_{1,2}(\hbar\omega) \tag{100}$$

To calculate N_1 and $N_{1,2}$ (see Eqs.(90) and (91)), we have assumed a Gussian distribution $D_t(E)$ having E_0 = 5.5 eV and δE_0 = 0.5 eV. For $E_{g,2}$ we take 9 eV which is close to the band gap of SiO_2. Our value of E_0 corresponds to the energy of traps in thermal SiO_2 produced by P and In impurities[103]. Shown by the closed circles in Fig.47 are values of $n_s(\hbar\omega)$ calculated using the above procedure. There is good agreement between the experiment (open circles) and theory (closed circles).

B. Charging by Light Illumination With Positive Bias

As we mentioned before, application of positive gate bias extends photocharging effect to the lower energy of incident light ($\cong$ 1.2 eV was the lowest energy of our measurements). The accumulated charge leaks off in a matter of minutes - rather quickly in comparison with the preceding case. The lower light energy limit of the effect suggests that the carrier generation by light in $Hg_{0.3}Cd_{0.7}Te$ is involved. Also, the faster charge leak- off points to a different nature of the interface states that hold the charge. At the present time we are not able to propose a detailed model explaining this effect.

In conclusion we investigated the effects of

illumination at 77K, with and without DC bias, on the C-V characteristics of a $Hg_{0.3}Cd_{0.7}Te/SiO_2$- Photox^{TM} MIS device. The light- induced chrge for zero bias is maintained for at least 8 h indicating very slow rates having characteristic frequency $<10^{-5}$ s^{-1}. The saturation value of Δu_{fb} for zero bias ehxibits a pronounced peak at $\lambda \cong 2800$Å (4.7 eV). These results can be explained by a model involving light- induced charging and discharging of very slow trap states in SiO_2 near the interface. These trap states have an energy distribution centered about 4.5eV above the SiO_2 valence band.

With positive gate voltage the charging mechanism is extended to lower wavelengths, the resulting charge quickly leaking off. At present time we do not have a detailed model to explain the bias- induced phenomenon.

Appendix A

Influence of Interference on the Photoreflectance and Thermoreflectance Spectra of Bulk CdTe

A number of authors pointed out the importance of interference effects in interpreting results of modulation spectroscopy[104,105] at the early stages of its development. In particular Fisher[104] has shown, that in the fundamental gap region, the reflection from the back surface of a bulk sample may lead to a signal below the bandgap energy being observed in the modulated reflection spectra. The interference effects become more pronounced and intricate when the multilayer structures are studied[106,107].

We have studied the influence of interference effects on the photoreflectance and thermoreflectance (TR) spectra of a bulk undoped CdTe sample. The sample was cut perpendicular to <111> direction and both front and back surfaces were polished according to the procedure described in section 3.3.1. The resulting thickness of the sample was 1.3 mm. Then TR and PR spectra were taken at 77K. After that, the back surface of the sample was roughened using 600 grit silicon carbide powder and the spectra were taken again.

The PR spectra were taken using 632 nm radiation from 1.5 mW He- Ne laser as the pump source at 500Hz. To facilitate the TR measurement, a strip of conducting paint was applied around the perimeter of the sample. The square wave current (approximately 1.0 V, 200 mA peak value) that was put through the strip at a frequency 8 Hz created the necessary temperature modulation.

We are presenting the comparison of the results for the sample with polished and rough back surface in Fig.48 (PR measurements) and Fig.49 (TR measurements). Photoreflectance spectra of the sample with polished and rough back surface are quite similar. In contrast, the TR spectra markedly differ. While in the rough back surface case, the TR spectrum consists of a single feature; the spectrum in the polished back surface case displays two of them.

The higher energy feature in the latter case coincides in energy with the position of the PR peak. The only feature obtained in the rough back surface case is somewhat lower in energy. At the moment we can't say whether the shift is a result of a change in the back surface condition or the difference in the heating conditions. In our experiment the heating strip is painted on the sample surface by hand. This process does not provide great reproducibility of thickness or

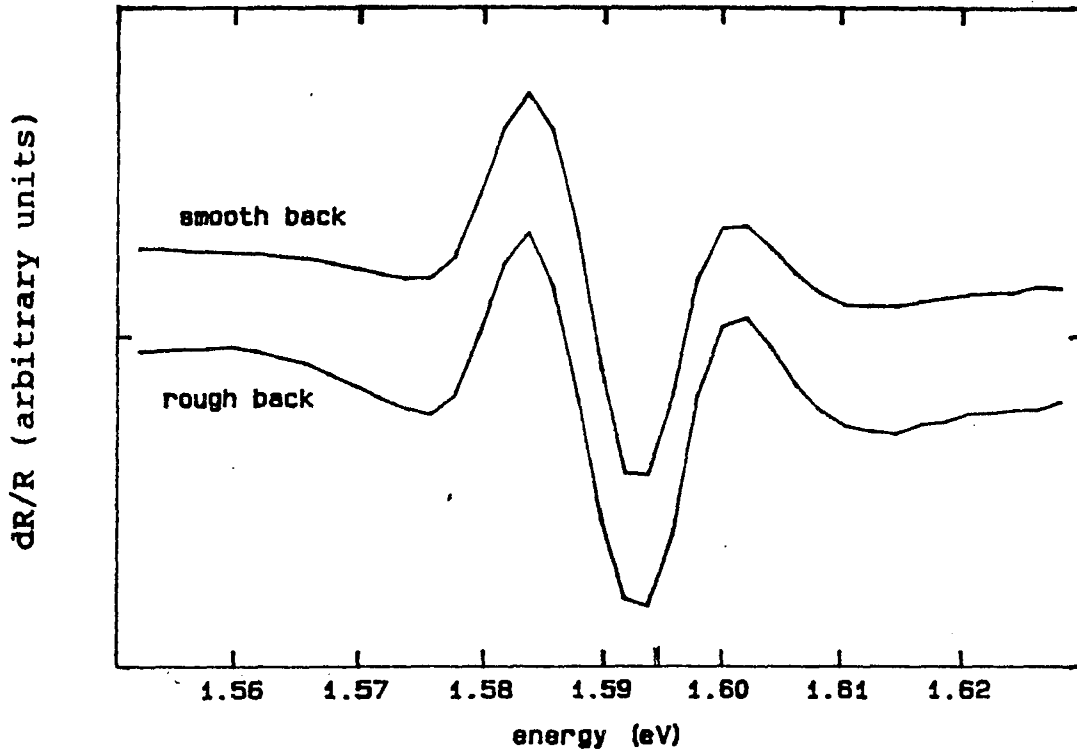

Fig.48

Photoreflectance spectra of CdTe (111) sample at 77K taken with smooth (polished) and rough back surface.

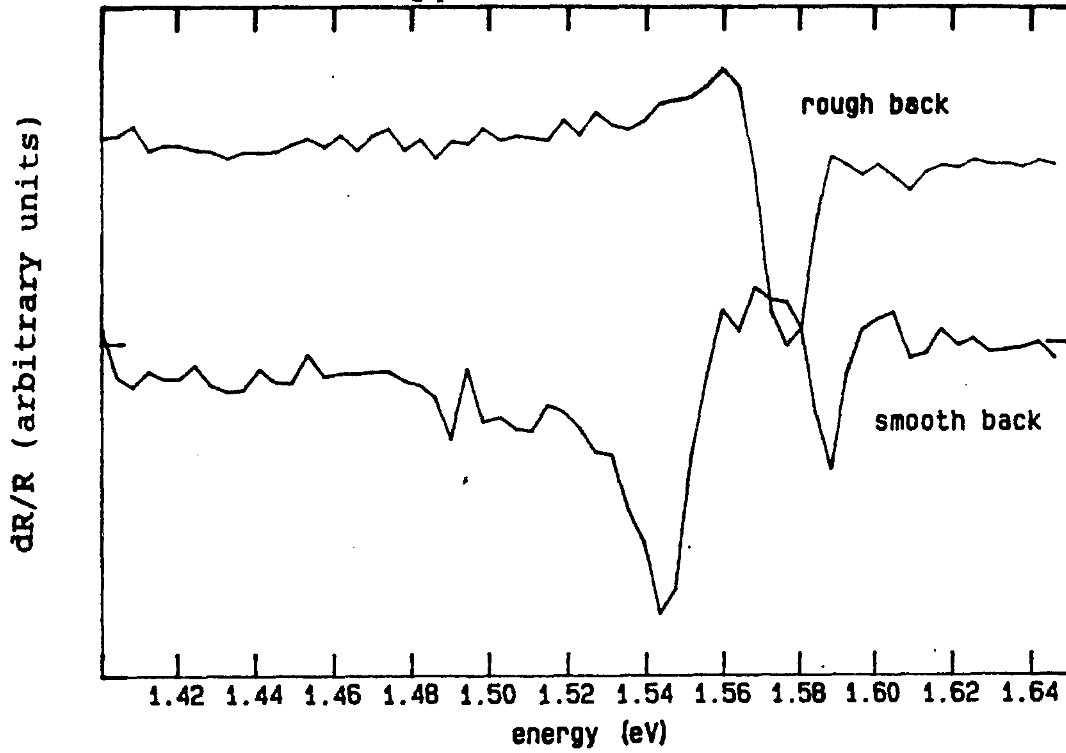

Fig.49

Termoreflectance spectra of CdTe (111) sample at 77K taken with smooth (polished) and rough back surface.

pattern. Since the back surface was roughened between the measurements, the strip had to be repainted and the sample had to be remounted. Therefore, in spite of trying to keep the modulating current on the same level, we may not have reproduced the heating conditions of the first measurement adequately. Consequently, we shall only attempt to interpret the presence of the additional lower energy feature in the spectra of the sample with polished back.

The additional feature which appears in the TR spectrum of the sample with polished back surface can be explained by the mechanism introduced by Fischer specifically for the spectral regions where the onset of absorption occurres[104]. The reflection from the back surface introduces the normalized modulation signal $\delta I/I$ which can be expressed as[104]:

$$\delta I/I \propto -R'(\delta\alpha)\cdot d\cdot e^{-\alpha d} \qquad (101)$$

where R' is the back surface reflectance, α is the absorption coefficient, $\delta\alpha$ is a modulated component of α and d is the sample thickness. According to Eq.(101), while the sample is relatively transparent, the onset of absorption will cause the increase of $\delta I/I$ signal due to the rise of the $\delta\alpha$ term. As the absorption increases, the $e^{-\alpha d}$ term dominates the expression and the signal dies out. Roughening the back surface will reduce R' (which apparently happened in our case); Therefore, the

signal originating from the back surface reflection will not be seen.

The fact that the mechanism does not manifest itself strongly in PR spectra is due to the difference in modulation methods. According to Aspnes and Frova[108], the magnitude of $\delta\alpha$ is proportional to:

$$\delta\alpha \propto \int_{z_0}^{z_d} dz' \cdot \delta\alpha(z') \qquad (102)$$

where z_0 and z_d are the coordinates (in depth of the sample) of the surface and of the point at which the modulation totally decays and $\delta\alpha(z')$ is the dependence of modulation on depth.

The depth of the modulating field in the case of PR is determined by the surface depletion layer depth which is typically several micrometers or less[100]. In the case of TR, the modulation depth is much bigger. Indeed, the modulation strength decreases gradually through the sample toward the back surface which is in contact with the heatsink. The modulation depth must constitute an appreciable fraction of the sample thickness. Therefore, according to Eq.(102), the quantity $\delta\alpha$ is much larger in the case of TR method, making the effect of the back surface reflection much more pronounced than in PR.

In conclusion, we have studied the influence of

the interference effects on the lineshape of PR and TR spectra of the CdTe in the fundamental gap optical region. The reflection from the back surface drastically changes the lineshape of the TR spectrum introducing a new feature below the energy of fundamental bandgap. No apparent change in the PR lineshape is introduced. The appearance of the additional structure in TR spectra can be explained within existing theoretical framework. The lower sensitivity of PR spectra to the back surface reflection can be explained by a much smaller depth of modulation than in the TR method.

References

1. G. Burns, Introduction to Group Theory with Applications (Academic Press, New York, 1977).

2. D. J. Chadi, J. P. Walter and M. L. Chen, Phys. Rev. B5, 3058 (1972).

3. D. J. Chadi, M. L. Cohen, Phys. Rev. B7, 692 (1973).

4. S. Katuski and M. Kumnimune, J. Phys. Soc. Jap. 31, 415 (1971).

5. R. Dornhaus and G. Nimtz in Springer Tracts in Modern Physics, vol.98 (Spinger-Verlag, New York, 1985) and references therein.

6. F. Urbach, Phys. Rev. 92, 1324 (1953).

7. H. H. Woodbury, Phys. Rev. B9, 5188 (1974).

8. H. H. Woodbury and M. Aven, Phys. Rev. B9, 5195 (1974).

9. K.Zanio in Semiconductors and Semimetals, vol.13, ed. by R. K. Willardson and A. C. Beer (Academic Press, New York, 1978).

10. J. Camassel, D. Auvergne and H. Mathieu, Solid State Commun. 13, 63 (1973).

11. A. Kisiel and P. M. Lee, J. Phys. F2, 395 (1972).

12. M. W. Scott, J. Appl. Phys. 40, 4077 (1969).

13. J. D. Wiley and R. N. Dexter, Phys. Rev. 181, 1181 (1969).

14. G. S. Eidzynas, Yu. F. Kavalyauskas, and A. Yu. Shileika, Sov. Phys. Semicond. 20, 499 (1986).

15. M. L. Cohen and D. J. Chadi, in Handbook on Semiconductors, vol.2 ed. by M. Balkanski (North Holland, Amsterdam, 1980).

16. A. Moritani, K. Taniguchi, and C. Hamaguchi, J. Phys. Soc. Jap. 34, 79 (1973).

17. P. M. Raccah, J. W. Garland, Z. Zang, V. Lee, D. Z.

Xue, L. L. Abels, S. Ugur and W. Wilensky, Phys. Rev. Letts. 53, 1958 (1984).

18. P. M. Raccah, V. Lee, S. Ugur, D. Z. Xue, L. L. Abels, J. W. Garland, J. Vac. Sci. Technol. A3, 183 (1985).

19. A. Lastras- Martines, U. Lee and P. M. Raccah, J. Vac. Sci. Technol. 21, 157 (1982).

20. A. Ksendzov, F. H. Pollak, P. M. Amirtharaj and J. A. Wilson, Journ. of Cryst. Growth 86, 586 (1988).

21. L.Viña, C. Umbach, M. Cardona, and L. Vodopyanov, Phys. Rev. B29, 6752 (1984).

22. V. G. Sredin, V. G. Savitskii, Y. V. Danilyuk, M. V. Miliyanduch ,and V. Petrovich, Sov. Phys. Semicond. 15, 249 (1981).

23. W. Hayes and R. Loudon, Scattering of Light in Solids (John Wiley and Sons, New York,1978).

24. A. Mooradian and T. C. Harman, Proceedings of the Conference on the Physics of Semimetals and Narrow- Gap Semiconductors, ed. by D. L. Carter and R. J. Bate (Pergamon, New York, 1971), p.297.

25. K. K. Tiong, P. M. Amirtharaj, P. Parayanthal and F. H. Pollak, Solid State Commun. 50, 891 (1984).

26. Y. Barda and L. Samuel, Phys. Rev. B35, 8260 (1987).

27 J. Baars and F. Sorger, Solid.State. Commun.. 10, 875 (1972).

28. D. N. Talwar and M. Vandervyver, J. Appl. Phys. 56, 1601 (1984).

29. P. M. Amirtharaj, K.-K. Tiong, and F. H. Pollak, J. Vac. Sci. Tech. A1, 1744 (1983).

30. S. P. Kozyrev, L. K. Vodopyanov, and R. Triboulet, Solid. State. Commun. 45, 383 (1983).

31. H.W.Verleur and A. S. Barker Phys. Rev. 149, 715 (1966).

32. Z- W. Fu and J Dow, Phys. Rev. B36, 7625 (1987).

33. X. C. Shen, H. Shen, P. Parayanthal, F. H. Pollak,

J. N. Schulman, A. L. Smirl, R. M. McFarlane, and I. D'Haenes, Superlattices and Microstructures 2, p.513 (1986).

34. M. Cardona, Modulation Spectroscopy (Academic Press, New York, 1969).

35. D. E. Aspnes and N. Bottka in Semiconductors and Semimetals, vol.9 (Academic Press, New York), 1972.

36. D. E. Aspnes, Proceedings of the First International Conference on Modulation Spectroscopy, Tuscon, Arizona, Nov.23-28 1972 in Surface Science, 37, p.418 (1973).

37. D. E. Aspnes in Handbook on Semiconductors, vol.2, ed. by M. Balkansky (North Holland, Amsterdam), 1980.

38. H. R. Phillip and H. Ehrenreich, Phys. Rev. 129, 1550 (1963).

39. F. H. Pollak and R. Tsu, Proceedings of Society of Photooptical Engineers (SPIE, Bellingham, 1981) 276, 78 (1981).

40. L. D. Landau and E. M. Lifshitz, Electrodynamics of Continuous Media (Pergamon, Oxford, 1960), Chap.XIV.

41. F. Bassani and G. P. Parvassini, Electronic States and Optical Transitions (Pergamon Press, Oxford, 1975).

42. A. Sommerfeld, Optics (Academic Press, New York, 1964).

43. L. Van Hove, Phys. Rev. 89, 1189 (1953).

44. P. Lautenschlager, M. Carriga, S. Logothetidis, and M. Cardona, Phys. Rev. B35, 9175 (1985).

45. B. O. Seraphin and N. Bottka, Phys. Rev. 145, 628 (1966).

46. S. Antoci, E. Reguzzoni and G. Samggia, Solid State Commun. 9, 1081 (1971).

47. H. Shen and F. H. Pollak, private communication.

48. See, for example, p.440 of Ref.29.

49. E. W. Wang, W. A. Albers and C. E. Bleil, II-VI Semiconducting Compounds. 1967 International Conferense, ed. by D. G. Thomas (W. A. Benjamin, New York 1967).

50. P. M. Raccah, J. W.Garland, S. E. Buttrill, L. Francke and J. Jackson, Appl. Phys. Lett. 52, 9 (1988)

51. K. Misawa, A. Moritani and J. Nakai, Jap. J. Appl.Phys. 15, 1309 (1976).

52. R. E. Nahory and J. L. Shay, Phys. Rev. Letts. 21, 1569 (1968), J. Shay, Phys. Rev. 92, 803 (1970).

53. O. J. Glembocki, B. V. Shanabrook, W. T. Beard and J. Comas, Proceedings of Society of Photooptical Engineers (SPIE, Bellingham, 1985), 524, 86 (1985).

54. H. Shen, Z. Hang, S. H. Pan, and F. H. Pollak, Appl. Phys. Lett.,52, 2058 (1988).

55. K. C. Haas, H. Ehrenreich, and B. Veliky, Phys. Rev. B1, 1088 (1983).

56. L. E. A. Berlouis, P. M. Peter and R. G. Humphreys, Appl. Phys. Lett. 51, 502 (1987).

57. A. Rodzik and A. Kiziel, J. Phys. C 16, 203 (1983).

58. C. K. Kim, P. Lautenschlaeger and M. Cardona, Solid State Commun. 59, 797 (1986).

59. Y. P. Varshni, Physica (Utrecht) 34, 149 (1967).

60. J. A. Wilson and V. A. Cotton, J. Vac. Sci. Technol. A3, 199 (1985).

61. P. Koppel, J. Appl. Phys. 57, 1705 (1985).

62 P. M. Amirtharaj, J. H. Dinan, J. J. Kennedy, P. R. Boyd and O. J. Glembocky, J. Vac. Sci. Technol. A4, 2028 (1986).

63. P. M. Raccah, J. W. Garland, Z. Zhang, U. Lee, S. Ugur, S. Mioc, S. K. Ghandi and I. Bhat, J. Appl. Phys. 57, 2014 (1985).

64. $Hg_{1-x}Cd_xTe$ Surface and Defect Study Program. DARPA/DSO Contract No.MDA-903-83-C 0108: Fourth Interim Technical Report, Jan. 1985, Section III, p.43.

65. Section V of this dissertation.

66. X.C. Shen, H. Shen, P. Parayanthal, F.H. Pollak, J.N. Schulman, A.L. Smirl, R.M. McFarlane and

I.D'Haenens, Superlattices and Microstructures 2, 513 (1986).

67. F.H. Pollak in Photochemistry: Fundamental Processes and Measurement Techniques, ed. by W.L. Wallace, A.J. Nozik, S.K. Deb and R.H. Wilson (The Electrochemical Society, Pennington, 1982) p. 608.

68. R.N. Bhattacharya, H. Shen, P. Parayanthal, F.H. Pollak, T. Coutts and H. Aharoni, Proceedings of the Society of Photo-Optical Instrumentation Engineers (SPIE, Bellingham, 1987) 794, 81 (1987); also, Phys. Rev.B37, 4044 (1988).

69. R. Glosser and N. Bottka, Proceedings of the Society of Photo-Optical Instrumentation Engineers (SPIE, Bellingham 1987) 794, 88 (1987).

70. P. M. Amirtharaj, K. K. Tiong, P. Parayanthal, F. H. Pollak, and J. Furdyna, J. Vac. Sci. Technol. A3, 226 (1985).

71. G.H. Tsau, A. Shen, M. Madou, J.A. Wilson, V.A. Cotton and C.E. Jones, J. Appl. Phys. 59, 1238 (1986).

72. J. M. Francou, K. Samindayar, J. L. Paurat, J. P. Gaillard, A. Million and C. Fontane, Journ. of Cryst. Growth 72, 220 (1985).

73. J. L. Paurat, J. M. Francou, N. Magnea, E. Mova and K. Samindayar, Journ. of Cryst. Growth 72, 194 (1985).

74. P. M. Amirtharaj, R. C. Bowman and R. L. Alt, Advances in Semiconductors and Superlattices, 13-18 March, 1988, Newport Beach, CA.

75. M. Cardona and D. L. Greenway, Phys. Rev. 131, 98 (1963).

76. M. Cardona and G.Harbeke, Phys. Rev. Lett. 8, 90 (1962).

77. Y. F. Tsay, S. S. Mitra and J. F. Vetelino, J. Phys. Chem. Solids, 34, 2167 (1973).

78. M. Cardona in Light Scattering in Solids II ed. by M. Cardona and G. Güntherodt,(Springer-Verlag, Berlin, 1985), p.19.

79. E. Anastassakis in Dynamical Properties of Solids, ed. by G. K. Horton and A. A. Maradudin, (North Holland, New York, 1980), p.157.

80. G. W. Rubloff, E. Anastassakis and F. H. Pollak, Solid State Commun., 13, 1755 (1973).

81.R. M. Martin, Phys. Rev. B4, 3676 (1971)

82. A. Pinczuk and E. Burstein in Light Scattering in Solids, ed. by M. Cardona (Springer-Verlag, Berlin), 1975

83. P. J. Colwell and M. L. Klein, Solid State Commun. 8, 2095 (1970)

84. J. Menendez and M. Cardona, Phys. Rev. B31, 3696 (1985).

85. A. A. Godolin and E. I. Rashba in Proceedings of the Thirteenth International Conference on Physics of Semiconductors, ed. by F. G. Fermi (Tipografia Marves, Rome, 1976), p.284.

86. A. A. Godolin and E. I. Rashba, Solid State Commun. 19, 1177 (1976).

87. D. C. Hamilton, Phys. Rev. 188, 1221 (1969).

88. E. Bedel, R. Carles, A. Zwick, J. B. Renucci and M. A. Renucci, Phys. Rev. B30, 5923 (1984).

89. P. W. Kruse in Semiconductors and Sememetals, vol.18 ed. by R. K. Willardson and A. C. Beer (Academic Press, New York, 1981), p.4.

90. F. H. Pollak and R. Tsu. Proceedings of Society of Photooptical Engineers (SPIE, Bellingham, 1983) 452, 26 (1983).

91. J. Menendez , M. Cardona, and L. K. Vodopyanov, Phys. Rev. B31, 3705 (1985).

92. H. Richter, Z. P. Wang and L. Ley, Solid State Commun. 39, 625 (1981).

93. M. Zigone, R. Beserman and M. Balkanski in Proceedings of the Second International Conference on Light Scattering in Solids (Paris, July 19-23,1971), ed. by M. Balkanski (Flammarion, Paris), 1971.

94. P. Y. Yu, M. H. Pilkuhn and F. E. Evangelisti, Solid State Commun. 25, 371 (1978).

95. W. F. Leanard and M. Michael, J. Appl. Phys. 50,

1450 (1979).

96. Y. Nemirovsky and I. Kidron, Solid State Electron. 22, 831 (1981).

97. M. A. Kinch in Semiconductors and Semimetals, Vol.18, ed. by K. Willardson and A. Beer (Academic Press, New York, 1981), p.131.

98. G. H. Tsau, Z. Sher, M. Madou, J. A. Wilson, V. A. Cotton and C. E. Jones, J. Appl. Phys. 59, 1238 (1986).

99. R. B. Shcoolar, B. K. Janousek, R. L. Alt, R. C. Carscallen, M. J. Daughtery and A. A. Fote, J. Vacuum Sci. Technol. 21, 164 (1982).

100. S. M. Sze, Physics of Semiconductor Devices (John Wiley and Sons, New York, 1981).

101. E. H. Nicollian and A. Goetzberger, Bell Systems Tech. J. 46, 1055 (1967).

102. C. N. Berglund, IEEE Trans. Electron. Devices, ED-13, 701 (1966).

103. R. F. DeKreesmaecker, D. J. Dimaria and S. T. Pantelides, in The Physics of SiO_2 and its Interfaces, ed. by S. T. Pantelides (Pergamon, Oxford, 1978)

104. J. E. Fischer, Surface Sci. 31, 473 (1973).

105. V. K. Subashiev, Surface Sci. 37, 947 (1973).

106. P. C. Klipstein and N. Apsley, J. Phys. C 19,6461 (1986).

107. X. L. Zheng, D. Heiman, B. Lax and F. A. Chambers, Appl. Phys. Letts. 52, 287 (1988).

108. D. E. Aspnes and A. Frova, Solid St. Commun. 7, 155 (1969).

109. We explored the more complicated equivalent circuits which include the presence of the interface states fast enough to follow the probe voltage as proposed in Ref.(91). In this work we are only interested in determination of the flatband voltage. We compared results for our device obtained using the equivalent circuit of Ref.91 and the simple one described here, and found very little difference.